

Department of Engineering Science
University of Oxford

Wave Theory for Guided Surface Plasmon Polaritons in Dielectric/Metallic Waveguide Arrays

Yufeng ZHOU

Brasenose College

A thesis submitted for the degree of
Master of Science by Research
Trinity Term 2013

Abstract

Wave Theory for Guided Surface Plasma Polariton in Dielectric/Metallic Waveguide Arrays

Yufeng ZHOU
Brasenose College/
Department of Engineering Science
University of Oxford

A thesis submitted for the degree of Master of Science by Research
Trinity Term 2013

In order to achieve a more comprehensive understanding of the sub-wavelength optical communication, or namely the plasmonic communication, the guided surface plasma polaritons (SPPs) in a general dielectric/metallic (D/M) waveguide array is studied both analytically and numerically.

An iterative-type analytical solution of a general D/M waveguide structure is derived for the first time. By applying the general solution to several established cases, such as a three layer D/M waveguide, the validity of the derivation is carefully scrutinized. A detailed numerical analysis based on the analytical result is then presented. Important parameters of such waveguide array, including the energy confinement and propagation loss, are mainly focused on.

Based on the solid theoretical research of a general D/M waveguide, the coupling effect between a symmetric mode (*s*-mode) and an anti-symmetric mode (*a*-mode) in a specific waveguide, namely the five layer D/M waveguide, is studied. The lossy nature of the anti-symmetric mode is capable of shortening the coupling distance (or coupling length) into the sub-wavelength range. This newly proposed device shows

potential in developing different integrated optical circuit elements, such as couplers, multiplexers, and so forth. In this thesis, a plasmonic coupler is proposed with detailed illustrations. By taking advantage of the super short coupling distance property, the coupler could be applied to interchange 1.55μm plasmonic signals between two channels within hundreds of nanometers' propagation distance. Compared with the current studies of plasmonic couplers [1], the dimension (length) of such an element could be reduced significantly.

Acknowledgements

The past two years has been one of the greatest times throughout my studies. It has been my great honour to be surrounded by so many talented professors and researchers at Oxford, the leading research university in the world. The purpose of this section is to send my gratitude to all the people in these two years who have influenced me and helped me to make progress.

First of all, I am heartily thankful to my supervisor Dr. Frank Payne for his guidance, encouragement and support. His professional knowledge in the field of optoelectronics and his diligent attitude towards research initiate my interest and motivated me to work hard.

I also would like to send my gratitude to Prof. DC O'Brien and Dr. CJ Stevens for their time in assessing my project. The feedback they provided during the first year's transfer viva was of great help.

I am more than lucky to have my parents who are very supportive to my research study in Oxford. Without your caring, I would hardly achieve half of the goals I have fulfilled up to now. Meanwhile, I would like to thank my beloved Violet. Meeting you and having you being by my side are definitely the best moments of my Oxford time, or even my life.

Finally, I would like to thank all of those who supported me through the difficult moments through the last year, including my colleagues and my friends in Oxford, London, Hong Kong and my home. Research life would become boring and lonely without any of you.

CONTENTS

ABSTRACT

ACKNOWLEDGEMENT

CONTENTS

LIST OF FIGURES

Chapter 1 Introduction **1**

1.1 Objectives 1

1.2 Overview of Plasmonic Waveguide Analysis 2

1.2.1 Analytical Approach 4

1.2.2 Numerical Approach 6

1.3 Overview of Plasmonic Communication 8

1.3.1 Plasmonic Component 8

1.3.2 Plasmonic Communication System 10

1.4 Scope and Organization 12

Chapter 2 Background **14**

2.1 Introduction 14

2.2 Surface Plasmon Polariton (SPPs) 14

2.3 Scalar Wave Equation 15

2.4 Plasmonic Waveguide Analysis 17

2.4.1 Slab Waveguide (Planar Waveguide) 17

2.4.2 Plasmonic Slab Waveguide Analysis 19

2.5 Plasmonic Coupler 23

2.5.1 Analytical Derivation 24

2.6 Drude's Model 26

2.7 Conclusion 27

Chapter 3 Theoretical Analysis of the General D/M Waveguide 28

3.1 Theory 28

3.1.1 Physical Condition Description 28

3.1.2 Two-sided Waveform Expression 29

3.2 General D/M Waveguide Array 32

3.2.1 Boundary Condition Discussion 32

3.2.2 Iterative Derivation 34

3.3 Regular D/M Waveguide Array 33

3.3.1 Analytical Solution 34

3.3.2 Numerical Simulation & Discussions 40

3.4 Analytical Scrutinize of the General D/M Waveguide 48

3.4.1 General IMI Waveguide 48

3.4.2 General IMIMI Waveguide 49

3.5 Conclusion 50

Chapter 4 Numerical Analysis of the General D/M Waveguide 51

4.1 Introduction 51

4.2 Energy Confinement 52

4.2.1 Time-averaged Power of Signal Transmission 52

4.2.2 Time-averaged Power Ratio of Adjacent Layers 53

4.2.3 Simulation Results & Discussion 58

4.3 Propagation Loss 65

4.3.1 Time-Averaged Power Loss 65

4.3.2 Simulation Results & Discussion 66

4.4 Conclusion 70

Chapter 5 Coupling Effect between Different Plasmonic Modes 71

5.1 Introduction 72

5.1.1 Structural Description of a Duo-Channel SPP Coupler 72

5.1.2 Mechanism of a Duo-Channel SPP Coupler 73

5.2 Approximated Analytical Model 74

5.2.1 Transversal Approximation 74

5.2.2 Longitudinal Analysis 77

5.2.3. Numerical Comparisons 81

5.3 Exact Numerical Model 84

5.3.1 Motivation 84

5.3.2 Model Description 84

5.3.3 Simulation Results & Discussion 88

5.4 Phase Control of the Coupler 92

5.4.1 Introduction 92

5.4.2 Numerical Analysis of the Phase Control 94

5.4.3 Important Parameters of the Phase Control 99

5.5 Data Transmission 102

5.5.1 Objectives 102

5.5.2 Output Modal Description 104

5.5.3 Important Quantities 105

5.6 Conclusion 109

Chapter 6 Conclusion **112**

6.1 Summary of Findings 112

6.2 Future Work 114

REFERENCES

List of Figures and Tables

Figure 1-1: An Overview of A General D/M Waveguide Array 1

Figure 2-1: Sketch of the SPP Propagation in a Cartesian Coordinate 16

Figure 2-2: Sketch of A General Slab Waveguide 17

Figure 2-3: D/M Waveguide Array with Single Interface 19

Figure 2-4: MIM Waveguide Array with Two D/M Interfaces 22

Figure 2-5: Transversal Surface of a Two-Waveguide Coupler 23

Figure 3-1: Transverse Profile of A General Dielectric/Metallic Waveguide Array 28

Figure 3-2: Transversal Profile of an Regular D/M Waveguide Array 37

Figure 3-3: Transversal Surface of an IMIMI Waveguide 38

Figure 3-4: Transversal Surfaces of the MIM and IMI Waveguides 38

Figure 3-5a: Real Part of the Effective Index of the Symmetric Mode in IMIMI 39

Figure 3-5b: Imaginary Part of the Effective Index of the Symmetric Mode in IMIMI 39

Figure 3-5c: Real Part of the Effective Index of the Anti-Symmetric Mode in IMIMI 40

Figure 3-5d: Imaginary Part of the Effective Index of the Anti-Symmetric Mode in IMIMI 40

Figure 3-6a: Real Part of the Effective Index of the Symmetric Mode in MIM 44

Figure 3-6b: Imaginary Part of the Effective Index of the Symmetric Mode in MIM 44

Figure 3-6c: Real Part of the Effective Index of the Anti-Symmetric Mode in MIM 45

Figure 3-6d: Imaginary Part of the Effective Index of the Anti-Symmetric Mode in MIM 45

Figure 3-7: An IMIMI Waveguide with Large Core Layer Thickness 46

Figure 4-1: Transversal Definition of the Core Layers in IMIMI Waveguide 52

Figure 4-2: The Adjacent Power Ratio of the Two Metal Layers and the Core Layer 58

Figure 4-3: The Confined Energy (in the core layers) Percentage Against Different Metal Layer Thickness (nm) 59

Figure 4-4: The Adjacent Power Ratio of the Two Metal Layers and the Core Layer 60

Figure 4-5: The Confined Energy (in the core layers) Percentage Against Different Metal Layer Thickness (nm) 60

Figure 4-6: The Adjacent Power ratio of the Two Metal Layers and the Core Layer 61

Figure 4-7: The Confined Energy (in the core layers) Percentage with Different Core Layer Thickness (nm) 62

Figure 4-8: The Adjacent Power Ratio of the Two Metal Layers and the Core Layer 63

Figure 4-9: The Confined Energy (in the core layers) Percentage Against Different Metal Layer Thickness (nm) 63

Figure 4-10: Normalized Transmission Power of s-mode and a-mode in IMIMI Waveguide 67

Figure 4-11: Propagation Length of s-mode with Different IMIMI Waveguide Structures 68

Figure 4-12: Propagation Length of *a*-mode with Different IMIMI Waveguide Structures 68

Figure 5-1: Longitudinal Profile of A Duo-Channel SPP Coupler 72

Figure 5-2: Transverse Profile of A Duo-Channel SPP Coupler 72

Figure 5-3a: Numerical Plotting of the Real Part of the Transversal Superposition between Amplitude-Normalized LRSPP and SRSPP 75

Figure 5-3b: Numerical Plotting of the Imaginary Part of the Transversal Superposition between Amplitude-Normalized LRSPP and SRSPP 76

Figure 5-4: The Coupling Length (L_C) of An IMIMI Waveguide under Different Dimensions 81

Figure 5-5: The Coupling Length (L_C) vs. Different Amplitude Ratios of the Two Modes 82

Figure 5-6: *y*-*z* Plane Boundries of the Two Channels 85

Figure 5-7: Power Density Function of Each Channel with Different Amplitude Ratios 87

Figure 5-8: The Coupling Length (L_C) of an IMIMI Waveguide under Different Amplitude Ratios of the Two Modes by Exact Numerical Simulation 88

Figure 5-9: The Coupling Length (L_C) Ratio between the Exact Numerical Method and Approximated Analytical Method 89

Figure 5-10: The Average Coupling Length (L_C) Ratio between the Exact Numerical Method and Approximated Analytical Method of Figure 5-9 90

Figure 5-11: Longitudinal Profile of a Duo-Channel SPP Coupler 92

Figure 5-12: Output Signal from the Different Channel of Input 95

Figure 5-13: The Coupling Length against Different A_{ratio} When the Information Signal is Guided from the Different Channel 95

Figure 5-14: Output Signal from the Same Channel of Input 96

Figure 5-15: The Phase Shift of the Control Signal Against Different A_{ratio} 97

Figure 5-16: The Relative Power Ratio of Two Output Conditions Against Varied Control Phase Values 100

Figure 5-17: The Relative Power Ratio of Two Output Conditions Against Varied Amplitude Ratio Values 101

Fig 5-18a: Numerical Plotting of the Real Part of the Digit '0' *H*-Field 103

Fig 5-18b: Numerical Plotting of the Imaginary Part of the Digit '0' *H*-Field 103

Fig 5-19a: Numerical Plotting of the Real Part of the Digit '0' *H*-Field 104

Fig 5-19b: Numerical Plotting of the Imaginary Part of the Digit '0' *H*-Field 105

Fig 5-20: On/Off Power Ratio with regarding to A_{ratio} values 106

Fig 5-21: Input/ Output Power Difference Ratio with regarding to A_{ratio} values 108

Table 5-1: Dimensions and Material Properties of the Coupler 73

Table 5-2: Transversal Decay Rates of Each Layer in the IMIMI Coupler 75

Table 5-3: Real and Imag Part of the Effective Indexes for Both Modes 79

Table 5-4: Numerical Selections of A_{ratio} Regarding to Different w_d Values 96

Table 5-5: Numerical Selections of $\boldsymbol{\varphi}$ Regarding to Different w_d Values When the Length of the Coupler is Fixed as 100nm 97

Table 5-6: Relative Power Ratio of Both Outputs Regarding to Different w_d Values 98

Chapter 1 Introduction

1.1 Objectives

This project is based on the analysis of a general metallic/dielectric (D/M) waveguide with multiple layers, which is also named as the D/M waveguide array. The following figure 1-1 is a structural illustration of such a waveguide. In this thesis, both the analytical and the numerical work aim at providing a solid foundation for future application development based on such structures.

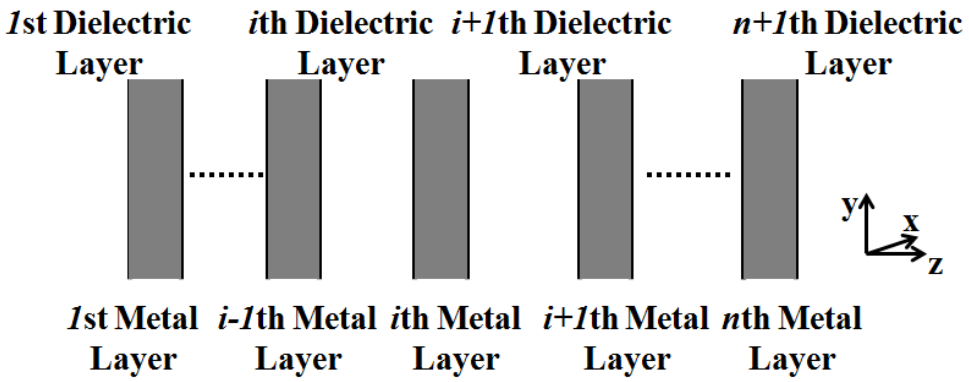


Fig 1-1: An Overview of a General D/M Waveguide Array

Figure 1-1 illustrates the geometry of a general D/M waveguide array, in which the *x*-axis is defined as the propagation direction and the *y*-*z* plane is the transversal surface. The theoretical solutions of several simple D/M waveguide arrays were published, and have been used for decades [2]. Based on the theoretical results, a number of researchers proposed approximate analytical models for more complicated waveguide structures, including the plasmonic interconnect [3]. These approximated models can be simulated for the numerical performances of multiple vital parameters of the waveguide study in the communication area, such as power loss, coupling effect, energy confinement and so forth [4]-[6].

However, as a fundamental element of this area, the D/M waveguide array has not been fully studied yet. As introduced above, current analytical studies are based on theoretical results of simple D/M waveguide arrays with limited number of layers, for example the three layer metal/insular/metal (MIM) waveguide [7].

Furthermore, the high speed transmission of the plasmonic signal has inspired numbers of research groups [8]-[10] to design applicable plasmonic elements, which could be connected with the highly developed realm of electronic integrated circuits (ICs). Although the plasmonic elements are much smaller than the conventional optical ones, they are still too bulky in the electronic ICs [11]. Therefore, the size reduction in both propagation direction and transversal direction of a plasmonic waveguide has become a principal problem in this field.

The main objectives of this thesis are to complete the theoretical study and to propose innovative approaches in size reduction of plasmonic elements. A complete analytical solution of an arbitrary D/M waveguide array is proposed for the first time. Based on the analytical solution, more simulation models could be developed for evaluating the vital parameters listed above in the plasmonic waveguide communication. Besides, by analyzing the coupling effect of the D/M waveguide array, a super-short coupling length within the sub-wavelength range is discovered.

In order to have a clear understanding of the work of this thesis, the recent research works in the field of plasmonic waveguide and plasmonic communication will be reviewed in the following sections. Also, the structure of the whole thesis will be listed for the ease of reading.

1.2 Overview of Plasmonic Waveguide Analysis

In general, the plasmonic waveguides can be sub-categorized into two types: the two-dimensional waveguide (with 1D transversal surface geometry) and the three-dimensional waveguide (with 2D transversal surface geometry). According to the transversal surface geometry displayed in figure 1-1, the general D/M waveguide array is a two-dimensional waveguide structure.

With a more complicated geometry structure of its transversal surface, the three-dimensional waveguide is usually studied in the following two methods: one is the approximated analytical approach, and the other one is the numerical approach [12]-[14]. The former is usually derived from the accurate analytical results of a certain relatively simpler waveguide structure. Given a specific material and geometry condition, this type of method is capable of providing straight forward expressions, together with accurate numerical simulations. The latter is applied when either the geometry is difficult to be simplified by existed analytical models, or the numerical results are more significant than the physical expressions.

The D/M slab structure (two-dimensional waveguide) is the foundation of metallic waveguide study. The *Plasmonics: Fundamentals and Applications* [16] has introduced the analytical solutions for several simple cases. As for the transverse 3D waveguide study, the rectangular metallic aperture, also called the transverse metallic strip, is mainly studied as for its wide application [17]-[19]. Recent published results in both analytical and numerical approaches are introduced in the following parts.

1.2.1 Analytical Approach

Different analytical approaches published in solving the metallic aperture structure under different conditions are introduced in this section. Important parameters such as complex effective index, cut-off wavelength, skin depth of metal and propagation loss are simulated and compared.

A. Kumar et al [20] applied the effective index method (EIM) [21] to the metallic waveguide case. In order to perfectly match the EIM with the structural profile, the outer metallic layer is regarded as infinite in both dimensional widths. In comparison with the traditional FEM and FDM results, the numerical performances of this analytical approach, including the effective index, propagation length and the cut-off frequency, are numerically close.

Apart from the EIM-based model, Gordon et al. have applied another analytical method to the metal stripe geometry [22]. In order to study the relationship between the cut-off frequency and the metal types, the 2D aperture structure is decomposed into two orthogonal 1D cases, with one carrying the TE mode and the other carrying the coupling TM mode. The structure introduced in [23] is the same as that of in [20], with a different structural decomposition method from [22]. Instead of using the EIM, an analytical solution for 2D metallic aperture is proposed under the specific physical condition that the near- and mid- infrared wavelength range (NIR and MIR) is above the cut-off frequency (cut-off criteria refers to [22]). Also, from the previous work [25], the TE_{10} mode has been determined as one of the dominant modes in the enhanced transmission [15] in such structures. Finally, they compute analytical expressions for

the two orthogonal 2D D/M arrays; one transmits coupled SPPs (Surface Plasma Polaritons), the other propagates TE_{10} mode. The approximated expression for the overall 3D array is then shown, with its numerical performance matching the reference very closely.

For multiple metallic waveguides, an analytical approach is proposed in [24] with a negative permittivity metal material (not complex). The classic SPP theory in a MIMIM (metal/insulator/metal/insulator/metal) structure is analytically solved with a set of solutions, β_a (anti-symmetric mode) and β_s (symmetric mode). Then by coupled wave theory, the dispersion relations in the periodic array can be derived as:

$$k_z = \beta + 2Ccos(k_x D) \tag{1.1}$$

In equation (1.1), k_z and k_x are the wave-vectors of the SPPs in transversal and propagation directions, respectively. D is the sum thickness of one metal layer and one dielectric layer, and $2\beta = (\beta_a + \beta_s)$, $2C = (\beta_a - \beta_s)$.

The coupling coefficient C is negative, which is different from dielectric arrays' positive values. This could be applied in negative refraction effect [38] and its applications [39].

1.2.2 Numerical Approach

Instead of trying to simplify the 2D structure under different physical or mathematical conditions, numerical approaches usually deal with the metal stripe(s) as a whole directly. In many published works, the FDTD/FDFD (finite differential time/frequency domain) [26]-[27] methods have proved to be reliable.

M. A. Swillam et al. have done a relatively full range of numerical study of a single rectangular metallic waveguide in [28]. They firstly display important guided modes guided in such structure in a wide wavelength range. The FDFD mode solver and Comsol Multiphysics [29] are used to simulate the dispersion characteristics of each mode. According to the wavelength, from short to long, three major modes and their operation bands are introduced as TE_{01} mode, guided anti-symmetric SPP mode and conventional mode (dielectric waveguide mode), respectively. The difference between a TM_{01} mode from a typical MIM structure and the TE_{01} is also discussed, which reveals that TM_{01} mode has a better performance in the near cut-off situations. Besides, unlike the 1D structures (MIM or IMI), which limit the slow/fast light transmission to only one polarization, the paper shows that the rectangular metal can enable polarization insensitive in such applications.

Except for the wavelength-based mode categories, the guided modes in a metallic waveguide can also be classified as leaky modes and bound modes [30]. In this paper, air-exposed surfaces of metallic stripes on glass substrates are studied by applying a specific numerical method, namely the FVH-FDM [31] with CCS-PML (full vectorial magnetic field finite difference method with complex coordinate stretching in

perfectly matched layer). The new proposed numerical method is capable of solving both leaky and bound modal in a metal stripe.

Though not studying rectangular shaped metal stripes, Tian Yang et al. propose a semi-analytical model in solving a nano-scale periodic dipolar metallic structure [32]. The numerical method they used to improve previous analytical works can be drawn to study the rectangular arrays numerically. On the basis of the published coupled dipole method (CDM) [33], they consider the fact that only real frequency/ wavelength signal is efficient in experiments or several principle simulations, such as FDTD. In the first place, the field from each dipole is obtained by FDTD. Then, the coupling effect between each dipole channel, which is real-frequency-based, can be found analytically [34]-[35]. Finally, the mixed model is capable of solving the dispersion relation of any periodic arrangement with identical unit waveguide, if the resonance properties and field profiles of a single waveguide have been solved. In [36], the mixed model carried out in [32] is numerically tested by FDTD.

1.3 Overview of Plasmonic Communication

Integrated optical circuits have been studied in many different application areas over the last 35 years. Various types of integrated optical components, sometimes named elements, have been designed and manufactured. One of the major purposes of developing this area was to reduce the number of electro-optics interconnectors and enhance the communication between analog signals and optical signals [40]. While the unexpected rapid advancements in the SPP area have expanded it into multiple components, such as optical splitting, coupling, filtering and routing of signals, and might lead the industry to the future of systematic plasmonic communication.

1.3.1 Plasmonic Component

Many studies in this topic are developed from the study of the SPP waveguide. In such cases, the components are mostly categorized according to the specific operation of SPP modes in such waveguides.

Robert Charbonneau et al. show a comprehensive research in the passive plasmonic components based on long-range SPPs (LRSPP) [41]. In their study, the ss_b^0 mode is mainly studied, in which the letter *s* means approximately symmetric in one dimension, 0 represents the fundamental mode. According to the advantages of this mode, such as low propagation loss, lower cut-off wavelengths for higher modes, and so forth, it has been treated as the LRSPP mode in a rectangular metal waveguide by several research groups [42]-[43]. Their experimental studies using the metal Au in SiO_2 have demonstrated the performance of ss_b^0 in structures like Y-junctions, s-bends, couplers, as well as Mach-Zehnder interferometers. In addition to the experimental

preparations, the numerical finite-difference method has also been used in analyzing the ss_b^0 in an Ag film supported by Si [44]. Robert Charbonneau et al. develop a set of numerical expressions for determining important transmission parameters of the ss_b^0 mode, including coupling efficiency, coupling loss, and the transition loss between the metal stripe and other optical elements, for example a single-mode fiber. The numerical results match with the experimental ones accurately at the propagation wavelength of 1550nm.

Meanwhile, the A. Boltasseva et al. show a strong interest at a wider wavelength range between 1250nm and 1650nm [40]. The theoretical part of their study led to the concept of EIM [21] for the thin metal film of finite width that supports the LRSPP. Based on the numerical and experimental demonstrations of LRSPP Y-splitters, a directional coupler was designed, which has possible coupling lengths of 1.9 and 0.8 mms. Two gold stripes with 15nm thick and different separation distances (4 micron and close to 0 micron) are used. The coupling length is determined as:

$$L_{\frac{\pi}{2}} = {}^{\pi}/_{2\kappa} \tag{1.2}$$

In (1.2), *L* determines the coupling length corresponding to full power transfer from one waveguide to another, and *k* is a coupling constant proportional to $1/\lambda$.

The loss of a similar directional coupler is studied by [45] with more experimental support. In order to simulate the DC for more wavelength modes, the simple wavelength dependent expression for the coupling constant is given as:

$$\kappa = \frac{\pi \delta N}{\lambda} \tag{1.3}$$

δN is the effective index difference between even modes and odd modes.

Experimentally, the coupling length is extended to 4.1 mm, with 8 micron separation of metal waveguides. At telecom's wavelength region, the loss of such a coupler is tested as 4dB/cm in propagation and 2dB coupling loss.

1.3.2 Plasmonic Communication System

Based on the sophisticated designs of single plasmonic components, the research interests in developing complete plasmonic communication system are growing. In the recent studies, key parameters such as signal delay, energy dissipation, cross talk and so forth, have been studied in different ways.

One of the applications for such systems is intra-chip interconnection. By pointing out the limitations of conventional interconnects based on electrons, J. A. Conway et al. have made several innovative discoveries in the area of plasmonic interconnection [46]. The major limitations of electronic signal propagation lies in the RC time of the conventional interconnect [51]. The resistance, R, increases when the cross section area decreases; while capacitance, C, does not decay significantly. Thus, the undesirable time increase is determined by the reduction of the wire scale. In plasmonics wires, the following equations are used in modeling the cylindrical sub-wavelength waveguide system in [46]:

$$\frac{\gamma_2 I_1(\gamma_1 a) K_o(\gamma_2 a)}{\gamma_1 I_0(\gamma_1 a) K_1(\gamma_2 a)} = -\frac{\varepsilon_1}{\varepsilon_2}, where\ \gamma_i = \left(k^2 - \varepsilon_i \frac{\omega^2}{c_0^2}\right)^{1/2} \quad (1.4)$$

In (1.4), γ_i is the evanescent field decay coefficients for different regions (1 for metal, 2 for dielectric substrate). I_n and K_n are the nth order modified Bessel functions of the first and second kind.

The group velocity of a 1 micron free-space wavelength signal reduces from $0.38c_0$ to $0.10c_0$ when the wavelength diameter decreases from 50nm to 10nm, and hence the group delay increases. The group delay of the 10nm plasmonic interconnect is still less than a 50nm conventional one. In contrast to the merits mentioned above, they also find the weakness of the plasmonic waveguide, which is the energy loss. The tightly confined SPP signal suffers a higher loss in a classic metal waveguide; even good metal (like Ag) is applied. Therefore, in [46], the research group comes to the conclusion that plasmonic interconnects can be well applied with high density when the communication distance is within the range that no significant power loss will be suffered.

Except for the studies in the cross section of plasmonic interconnects, Georgios Veronis et al. also focus on the longitudinal direction studies of such an interconnect of different waveguide dimensions, and provide a very precise analogy model for future applications [48]. At optical communication wavelengths, especially the interested one $1.55\mu m$, good metals like silver satisfies the condition that:$|\epsilon_{metal}| \gg \epsilon_{diel}$. Therefore, $|E_{x\,metal}| \ll |E_{x\,diel}|$ and the integral of the electric field in the *x*-axis direction (the cross section surface) can be approximated by $E_{x\,diel}d$. Thus, characteristic impedance of a fundamental MIM can be found as:

$$Z_{MIM}(d) = \frac{E_{x\,diel}d}{H_{y\,diel}} = \frac{\beta_{MIM}(d)}{\omega\epsilon_0}d \tag{1.5}$$

In (1.5), *d* is the core layer thickness of the waveguide. $\beta_{MIM}(d) = 2\pi/\lambda_g(d)$, where $\lambda_g(d)$ is the wavelength of the guided plasmonic signal.

1.4 Scope and Organization

The thesis mainly focuses on the study of the general D/M waveguide array and how this structure could be applied to confine the wave energy inside a nanometer-scale range. In order to provide a clear picture, the structure of the whole thesis is introduced as follows.

In Chapter 2, the background of the surface plasma theory is introduced, including the fundamental waveguide theory and latest experimental results. Besides, the Drude Model, which is used to quantify the metallic material property throughout this thesis, is also introduced.

In Chapter 3, the general D/M waveguide array for surface plasmon polaritons (SPPs) is studied. The characteristic equations of the guided plasmonic modes in such waveguides are derived theoretically. By simplifying the boundary conditions into several widely studied geometry models, the validity of the solution for the general structure is further strengthened.

In Chapter 4, on the basis of the theoretical results in chapter 3, approximated analytical models for several principle parameters, including energy confinement and propagation loss are developed. Later, by presenting the simulation results of such models, the propagation performance of each guided mode in such waveguides is analyzed numerically.

In Chapter 5, the special coupling effect between the LRSPPs (long-range SPP) and the SRSPPs (short-range SPP) at the same wavelength through an IMIMI waveguide array is studied. By choosing the widely applied communication

wavelength (~1.55μm), the coupling length is determined by both an approximated analytical approach and an accurate numerical approach. Furthermore, when the initial phase of each plasmonic mode is considered, the output of the coupler can be selected through the phase control of a partial input signal. Based on the proposal, the real data transmission case, namely the On/Off transmission model, is tested and simulated. By evaluating the key transmission parameters, the application potential of such a device is enhanced.

In Chapter 6, a summary of the whole thesis is given. The important results in each chapter are summarized. Several future work directions based on this project are also proposed.

Chapter 2 Background

2.1 Introduction

In this chapter, fundamental concepts and theories in the plasmonics area are to be introduced as the background information of the whole thesis. First of all, the mechanism of surface plasma is elaborated. After that, the theoretical principles of waveguide analysis, especially the plasmonic waveguide analysis, are illustrated with detailed mathematical derivations. Furthermore, the basic method of analyzing the plasmonic coupler is presented. At last, the property of metal material's permittivity is explained. By showing the general background of the plasmonic area, the 'theory-simulation' research pattern, which the dissertation follows, would be explicitly formed.

2.2 Surface Plasmon Polariton (SPPs)

Surface plasmon polaritons (SPPs) propagates along the interface between the dielectric material and the metallic material. The interface between the metal and dielectric causes the discontinuity in the electric field, which is perpendicular to the propagation direction, and the surface charges. SPPs are the radiation fields excited by the coupling of the electromagnetic fields to the metal (conductor) surface charges' oscillations. These fields will penetrate into both the metal and dielectric layers. Due to the transversal energy decay, the SPPs will finally be confined in the surface which is parallel to the propagation direction.

2.3 Scalar Wave Equation

2.3.1 Wave Equation & Maxwell's Equations

Starting from the fundamentals in Electromagnetism, a general equation that presents the nature of the guided surface plasmon polaritions (SPPs) should be introduced in the first place. In order to describe the physical properties of the SPPs, the Maxwell's Equations [52] are the fundamental tool to start with.

The Maxwell's equations are well-known as the link of the four fields, including the dielectric displacement **D**, the electric field **E**, the magnetic field **H**, as well as the magnetic flux density **B**. The following derivations throughout this thesis are based on the assumption that no external charge or current source exists in space.

$$\nabla \cdot \boldsymbol{D} = 0 \tag{2.1}$$

$$\nabla \cdot \boldsymbol{B} = 0 \tag{2.2}$$

$$\nabla \times \boldsymbol{E} = -\frac{\partial \boldsymbol{B}}{\partial t} \tag{2.3}$$

$$\nabla \times \boldsymbol{H} = \frac{\partial \boldsymbol{D}}{\partial t} \tag{2.4}$$

By combining equation (2.3) and (2.4) together, we may have:

$$\nabla \times \nabla \times \boldsymbol{E} = -\mu_o \frac{\partial^2 \boldsymbol{D}}{\partial t^2} \tag{2.5}$$

Since $\nabla \times \nabla \times \boldsymbol{E} \equiv \nabla(\nabla \cdot \boldsymbol{E}) - \nabla^2 \boldsymbol{E}$ and $\nabla \cdot (\varepsilon E) \equiv \boldsymbol{E} \cdot \nabla\varepsilon + \varepsilon \nabla \cdot \boldsymbol{E}$, equation (2.5) can be further simplified as follow:

$$\nabla^2 \boldsymbol{E} = \frac{\boldsymbol{\varepsilon}}{\boldsymbol{c^2}} \frac{\partial^2 \boldsymbol{E}}{\partial t^2} \tag{2.6}$$

where *c* is the speed of light, and the fields (**E**-field in this case) are defined to be harmonic-time-dependent, expressed as: $\boldsymbol{E}(\boldsymbol{r}, t) = \boldsymbol{E}(\boldsymbol{r}) e^{-i\omega t}$

Therefore, the *Helmholtz* equation [53] can be obtained and expressed as follow:

$$\nabla^2 \boldsymbol{E} + \boldsymbol{k_o^2 \varepsilon} \frac{\partial^2 \boldsymbol{E}}{\partial t^2} = 0 \tag{2.7}$$

where $k_o = \frac{\omega}{c}$, is the wave vector in vacuum, and ω is the angular frequency of the field.

2.3.2 Wave Equations with the Defined Propagation Geometry [54]

Consider an abstract propagation geometry shown below with a Cartesian coordinate defined as the three arrows:

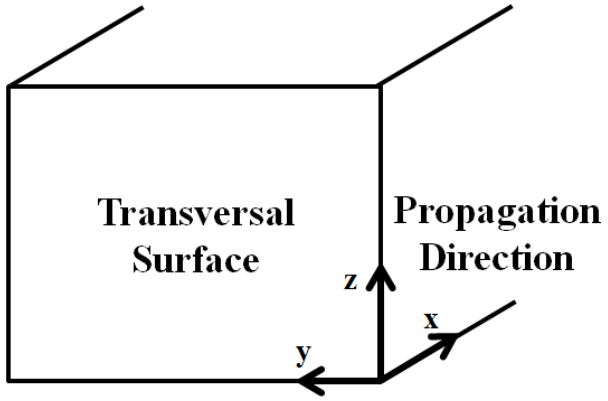


Fig 2-1: Sketch of the SPP Propagation in a Cartesian Coordinate

As shown in figure 2-1, there are two directions to be specified in determining the SPP propagation: the x-axis is the direction of wave propagation, and the y-z plane is the transversal plane. When the material is uniform along the x-axis, the propagating wave can be expressed as $\boldsymbol{E}(x,y,z) = \boldsymbol{E}(y,z)e^{i\beta x}$, where β is also defined as the propagation constant. Replacing this expression into equation (2.7), the scalar wave equation of the given propagation geometry can be obtained as follow:

$$\frac{\partial^2 \boldsymbol{E}(y,z)}{\partial y^2} + \frac{\partial^2 \boldsymbol{E}(y,z)}{\partial z^2} + (k_o^2 \varepsilon(y,z) - \beta^2)\boldsymbol{E}(y,z) = 0 \tag{2.8a}$$

Similarly, we can obtain the expression for the **H**-field of the same structure:

$$\frac{\partial^2 \boldsymbol{H}(y,z)}{\partial y^2} + \frac{\partial^2 \boldsymbol{H}(y,z)}{\partial z^2} + (k_o^2 \varepsilon(y,z) - \beta^2)\boldsymbol{H}(y,z) = 0 \tag{2.8b}$$

2.4 Plasmonic Waveguide Analysis

The waveguide structure is a specific geometry that guides the optical wave along a certain direction. As listed from chapter 1, it is usually sub-categorized into two types: the two-dimensional waveguide and the three-dimensional waveguide. Geometrically, the two-dimensional waveguide has uniform material distribution along the propagation direction of the plasmonic signal, as well as one of the directions on the transversal surface. The slab waveguide, which would be introduced later in section 2.4.1, is a typical two-dimensional waveguide which this thesis focuses on. A three-dimensional waveguide refers to the waveguide with a complex transversal geometry structure.

2.4.1 Slab Waveguide (Planar Waveguide) [55]

A slab waveguide is an ideal waveguide structure, which can also be named as a planar waveguide. Shown as the following diagram, a multi-slab waveguide with different refractive index can be solved by the specific wave equation as equation (2.8) and a set of boundary conditions.

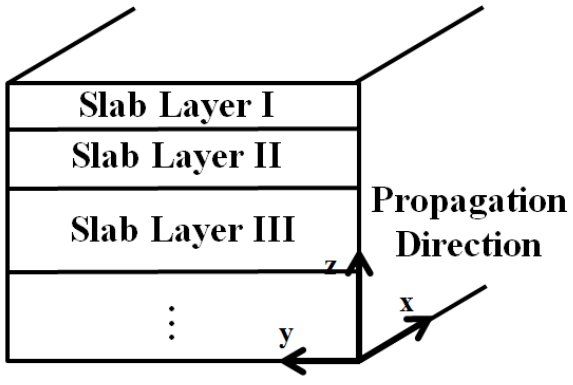


Fig 2-2: Sketch of A General Slab Waveguide

Traditional slab waveguides are composed of different dielectric materials in each slab layer, and it is used to guide the traditional waveguide modes (TWG) [56]. However, when one or several slab layers of the waveguide is metal, and the dimension of it is reduced to sub-wavelength range, the surface plasmon polaritons (SPPs) would survive. And such plasmonic slab waveguide is named as the dielectric/metallic (D/M) waveguide array in this thesis.

Before introducing the published analytical solutions of different types of D/M waveguide arrays, the specific scalar wave equations of the two most fundamental modes, the TE-mode and the TM-mode [57], are derived in this section.

Noting that equation (2.3) and (2.4) can be further decomposed into the three spatial axes, we may obtain the following group of coupled equations: [57]

$$\frac{\partial E_z}{\partial y} - \frac{\partial E_y}{\partial z} = i\omega\mu_o H_x \tag{2.9a}$$

$$\frac{\partial E_x}{\partial z} - \frac{\partial E_z}{\partial x} = i\omega\mu_o H_y \tag{2.9b}$$

$$\frac{\partial E_y}{\partial x} - \frac{\partial E_x}{\partial y} = i\omega\mu_o H_z \tag{2.9c}$$

$$\frac{\partial H_z}{\partial y} - \frac{\partial H_y}{\partial z} = -i\omega\varepsilon_o\varepsilon H_x \tag{2.9d}$$

$$\frac{\partial H_x}{\partial z} - \frac{\partial H_z}{\partial x} = -i\omega\varepsilon_o\varepsilon H_y \tag{2.9e}$$

$$\frac{\partial H_y}{\partial x} - \frac{\partial H_x}{\partial y} = -i\omega\varepsilon_o\varepsilon H_z \tag{2.9f}$$

Recall that x-axis is the propagation direction and y-axis is the oscillation direction of the fields, which means that $\frac{\partial}{\partial x} = i\beta$ and $\frac{\partial}{\partial y} = 0$, the coupled equations (2.9) can be further simplified for both fundamental modes.

For the TM modes, $H_x = H_z = E_y = 0$

$$\frac{\partial^2 H_y}{\partial z^2} + (k_o^2 \varepsilon(z) - \beta^2) H_y = 0 \tag{2.10a}$$

$$E_x = -i \frac{1}{\omega \varepsilon_o \varepsilon} \frac{\partial H_y}{\partial z} \tag{2.10b}$$

$$E_z = -\frac{\beta}{\omega \varepsilon_o \varepsilon} H_y \tag{2.10c}$$

For the TE modes, $E_x = E_z = H_y = 0$

$$\frac{\partial^2 E_y}{\partial z^2} + (k_o^2 \varepsilon(z) - \beta^2) E_y = 0 \tag{2.11a}$$

$$H_x = -i \frac{1}{\omega \varepsilon_o \varepsilon} \frac{\partial E_y}{\partial z} \tag{2.11b}$$

$$H_z = -\frac{\beta}{\omega \varepsilon_o \varepsilon} E_y \tag{2.11c}$$

2.4.2 Plasmonic Slab Waveguide Analysis

2.4.2.1 SPPs at Single D/M Interference

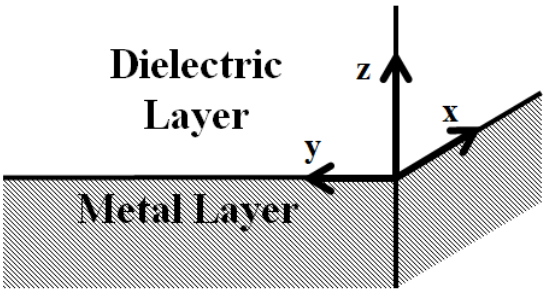


Fig 2-3: D/M Waveguide Array with Single Interface

As shown in figure 2-3, the waveguide is composed of two slab layers. One of them is a dielectric layer, and the other one is a metal layer. According to the physical description of SPP modes, the plasmonic energy would be confined along the surface between two layers and be propagated along positive *x*-axis. For each fundamental mode, the major field oscillates in the *y*-axis direction and varies against the *z*-axis coordination.

For the TM-modes, the major field H_y can be expressed as:

$$H_y(x,z) = \begin{cases} A_1 e^{k_m z} e^{i\beta x} & z \geq 0 \\ A_2 e^{-k_d z} e^{i\beta x} & z < 0 \end{cases} \tag{2.12}$$

where the wave vectors' *z*-axis components in each material region are $k_m = k_o\sqrt{n_{eff}^2 - \varepsilon_m}$, $k_d = k_o\sqrt{n_{eff}^2 - \varepsilon_d}$; the complex propagation constant $\beta = n_{eff}k_o$ and n_{eff} is the effective index of the TM mode SPPs in this structure; A_1 and A_2 are the peak amplitude values of the field.

By using equation (2.10b), the *x*-axis component of **E**-field, E_x, can be expressed as follow:

$$E_x(x,z) = \begin{cases} -iA_1 \dfrac{k_m}{\omega\varepsilon_o\varepsilon_m} e^{k_m z} e^{i\beta x} & z \geq 0 \\ iA_2 \dfrac{k_d}{\omega\varepsilon_o\varepsilon_d} e^{k_d z} e^{i\beta x} & z < 0 \end{cases} \tag{2.13}$$

Since the field components H_y and E_x must be continuous at the interface (z=0) between different slab layers (Boundary Conditions [58]), we can obtain the following results by equalizing both field equations at z=0:

$$\begin{cases} A_1 = A_2 \\ \dfrac{k_m}{k_d} = -\dfrac{\varepsilon_m}{\varepsilon_d} \end{cases} \tag{2.14}$$

And by expanding k_m and k_d with the target unknown n_{eff}, the propagation constant, namely the solution of this mode, can be solved as:

$$\beta_{TM} = k_o n_{eff} = k_o\sqrt{\frac{\varepsilon_m\varepsilon_d}{\varepsilon_m + \varepsilon_d}} \tag{2.15}$$

Equation (2.15) is widely regarded as the analytical solution of the TM-polarized plasmonic mode in such slab waveguide structure. As for the more complicated D/M waveguide arrays, different boundary conditions though, the concept of solving the propagation constant is the same.

Similarly, for the TE-modes, the major field E_y can be expressed as:

$$E_y(x,z) = \begin{cases} A_1 e^{k_m z} e^{i\beta x} & z \geq 0 \\ A_2 e^{-k_d z} e^{i\beta x} & z < 0 \end{cases} \tag{2.16}$$

By equation (2.11b), the *x*-axis component of **H**-field H_x can be written as follow:

$$H_x(x,z) = \begin{cases} iA_1 \dfrac{k_m}{\omega\mu_o} e^{k_m z} e^{i\beta x} & z \geq 0 \\ -iA_2 \dfrac{k_d}{\omega\mu_o} e^{k_d z} e^{i\beta x} & z < 0 \end{cases} \tag{2.17}$$

Since the field components E_y and H_x must be continuous at the interface (z=0) between the metal and dielectric layers, the following equation is obtained after matching equation (2.16) with (2.17):

$$A_1(k_m + k_d) = 0 \tag{2.18}$$

Since the SPPs only decays along *z*-axis in both slab layers, the real parts of k_m and k_d must be positive, so that $(k_m + k_d) \neq 0$. Therefore, the condition described by equation (2.18) leads to the only possibility that $A_1=0$, which is the peak amplitude value of the *E*-field.

Mathematically, it proves that no TE-polarized surface plasmon polarition can survive in the D/M waveguide array [13]. In this thesis, only the TM-polarized SPP modes in a general D/M waveguide array are mainly studied.

2.4.2.2 SPPs at MIM Waveguide Array

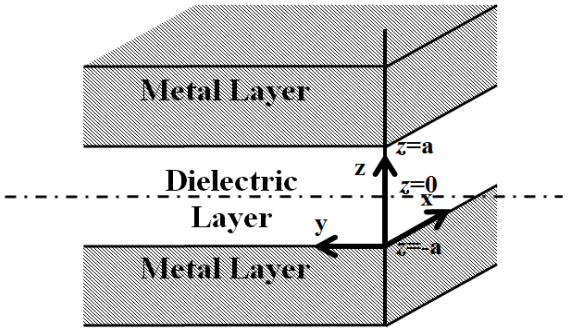


Fig 2-4: MIM Waveguide Array with Two D/M Interfaces

The name MIM waveguide is short for metal/insular/metal waveguide. The word 'insular' is the same as 'dielectric layer' in this thesis.

Similar to the section 2.4.2.1, the major fields (H_y) of TM-polarized SPP mode are first described.

$$H_y(x,z) = \begin{cases} Ae^{k_m(z-a)}e^{i\beta x} & z \geq a \\ Ce^{k_d z}e^{i\beta x} + De^{-k_d z}e^{i\beta x} & -a \leq z < a \\ Be^{-k_m(z+a)}e^{i\beta x} & z < -a \end{cases} \tag{2.19}$$

$$E_x(x,z) = \begin{cases} -iA\dfrac{k_m}{\omega\varepsilon_o\varepsilon_m}e^{k_m(z-a)}e^{i\beta x} & z \geq a \\ -iC\dfrac{k_d}{\omega\varepsilon_o\varepsilon_d}e^{k_d z}e^{i\beta x} + iD\dfrac{k_d}{\omega\varepsilon_o\varepsilon_d}e^{-k_d z}e^{i\beta x} & -a \leq z < a \\ iB\dfrac{k_m}{\omega\varepsilon_o\varepsilon_m}e^{k_m(z+a)}e^{i\beta x} & z < -a \end{cases} \tag{2.20}$$

where $k_m = k_o\sqrt{n_{1D}^2 - \varepsilon_m}$, $k_d = k_o\sqrt{n_{1D}^2 - \varepsilon_d}$, and $\beta = n_{eff}k_o$.

By solving the boundary conditions set at both $z=a$ and $z=-a$, two sets of solutions can be obtained as follow:

$$tanh(k_d \cdot a) = -\frac{k_m\varepsilon_d}{k_d\varepsilon_m} \tag{2.21}$$

$$coth(k_d \cdot a) = -\frac{k_m\varepsilon_d}{k_d\varepsilon_m} \tag{2.22}$$

Each transcendental equation solves the propagation constant for one possible plasmonic mode of the slab waveguide.

2.5 Plasmonic Coupler

One of the most important considerations in plasmonic communication is to achieve ultra-dense integration in between the waveguides and devices [5]. When two waveguides are close to each other, the fields of each modes overlap with the other ones, and cause the coupling effect. It could be used to design couplers with small dimension, and also could cause the unwanted crosstalk effect in the communication system [11]. The normal mode approach [13] is applied in this thesis to investigate the coupling effect of the specific waveguide array. Therefore, the mathematical derivations of such an approach are introduced in this section.

In the general case, the coupling effect is discussed in between two optical waveguides. As previously studied by Zia et al [30], the geometry of such 2D metallic waveguides can be described as the in the figure below.

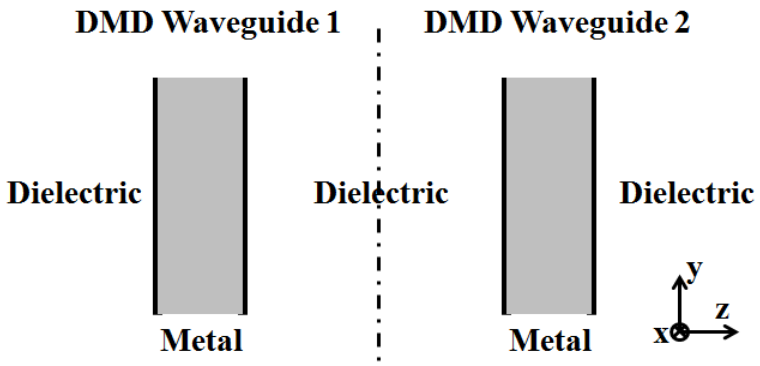


Fig 2-5: Transversal Surface of a Two-Waveguide Coupler

As shown from above, the coupler is composed of two dielectric/metal/dielectric (DMD) waveguides. Since a strongest coupling effect exists in between two identical waveguides [5], we may express the symmetric material function as follows:

$$\varepsilon(x, y, z) = \varepsilon(x, y, -z) \tag{2.23}$$

2.5.1 Analytical Derivation

Assume that the waveguide is uniform along the *y*-axis. Similar to the theoretical results of section 2.4.2.2, the symmetric coupler could support two types of plasmonic modes with either symmetric ($\boldsymbol{H}_s(y,z)$) or anti-symmetric ($\boldsymbol{H}_a(y,z)$) field distribution regarding to the surface z=0.

In normal mode approach, the input of the coupler is regarded as the superposition of the two possible modes.

$$\boldsymbol{H}_y(x,y,z) = c^s(x)\boldsymbol{\varphi}^s_{trans}(y,z) + c^a(x)\boldsymbol{\varphi}^a_{trans}(y,z) \tag{2.24}$$

Where the mode amplitude functions are as: $c^s(x) = A^s(x)e^{i\beta_s x}$ and $c^a(x) = A^a(x)e^{i\beta_a x}$. The complex propagation constants of each function can be expressed as: $\beta_s = \beta_{sr} + i \cdot \beta_{si}$ and $\beta_a = \beta_{ar} + i \cdot \beta_{ai}$.

Also, from the view of each waveguide (the LHS one and the RHS one), once the field is most confined within one of them, we may have the following equations:

$$\boldsymbol{H}_l(y,z) = \boldsymbol{\varphi}^s_{trans}(y,z)/\sqrt{2} + \boldsymbol{\varphi}^a_{trans}(y,z)/\sqrt{2} \tag{2.25a}$$

$$\boldsymbol{H}_r(y,z) = \boldsymbol{\varphi}^s_{trans}(y,z)/\sqrt{2} - \boldsymbol{\varphi}^a_{trans}(y,z)/\sqrt{2} \tag{2.25b}$$

Therefore we may use equation (2.25a and b) to interpret as:

$$\boldsymbol{H}_y(x,y,z) = c_l(x)\boldsymbol{H}_l(y,z) + c_r(x)\boldsymbol{H}_r(y,z) \tag{2.26}$$

Where $c_l(x) = c^s(x)/\sqrt{2} + c^a(x)/\sqrt{2}$ and $c_r(x) = c^s(x)/\sqrt{2} - c^a(x)/\sqrt{2}$; with $|c_l(x)|^2 + |c_r(x)|^2 = |c^s(x)|^2 + |c^a(x)|^2$. This proofs that the two different interpretations of the superposed field are conserved in power.

If the initial signal is guided from the LHS waveguide, the mathematical expressions of each waveguide can be written as: $c_l(0) = 1$ and $c_r(0) = 0$. When the power of the signal is coupled into the other side of the coupler, namely the RHS waveguide, we may first have $c_l(L_C) = 0$, where L is the propagating length of the signal. By using the above relations, we may have the following conditions at coupling length L:

$$c_r(L_C) = |\frac{1}{2}[\exp(-i\beta_s L_C) - \exp(-i\beta_a L_C)]|^2 \tag{2.27}$$

If equation (2.27) is applied into the conventional coupler where no lossy material is included, it can be further simplified as follow:

$$c_r(L) = \sin^2(\frac{\pi}{2}\frac{L}{L_C}) \tag{2.28}$$

From this periodic expression, we usually define the coupling length L_C as

$$L_C = \pi/|\beta_{sr} - \beta_{ar}| \tag{2.29}$$

2.6 Drude Model [47]

Compared with the dielectric materials, the metallic ones have different physical properties in many aspects. One of the major differences is that the complex refractive index of metallic material is sensitive to the optical frequency. While dielectric material has a relative constant value for a small wavelength spectrum variance range. In order to provide a more accurate refractive index value for the metallic material utilized in the waveguide analysis, the Drude Model is introduced in this thesis.

Drude Model is a mathematical expression shown as below, and it provides the numerical permittivity of metal, for example silver.

$$\varepsilon(\omega) = 1 - \frac{\omega_p^2}{\omega(\omega - j\gamma)} \tag{2.30}$$

where $\omega = k_o c$ is the optical frequency, $\omega_p = 1.2 \times 10^{16} Hz$ is the plasma frequency of silver, and $\gamma = 1.2 \times 10^{14} Hz$ is the collision frequency of silver.

In this project, the interested optical frequency is between the collision frequency and the plasma frequency. This will lead to the result that the refractive index of the metal is complex. For a frequency higher than the plasma frequency, the index will turn into pure real, which physically means that the metal will perform as dielectric.

In the following chapters, the metal material to be applied in the numerical simulation is silver. According to equation (2.30), the refractive index value -95.431+i*9.515 would be used when the plasmonic signal wavelength is at 1.55μm.

2.7 Conclusion

According to the objectives of the whole thesis listed in the first chapter, a few background concepts and derivations were explained in this chapter. These could be regarded as the basis of the research work to be elaborated in the following chapter 3, 4 and 5.

In section 2.3 and 2.4, the conventional theoretical studies of the slab waveguide were introduced first. Though the geometry condition of the waveguide's transversal surface to be investigated would be more complicated, the basic ideology of deriving the wave equation from the Maxwell equations is identical. Also, by providing the theoretical solution of the simple D/M waveguide arrays, the target result could be compared when the complex physical condition is simplified.

Later in section 2.5, the normal mode analysis method of analyzing the coupling effect within two identical plasmonic waveguides was presented. On the basis of such methodology, the special coupling effect could be investigated in chapter 5.

Besides, the Drude Model used in this thesis is also introduced in section 2.6. Similar to other research projects listed in section 1.2 and 1.3, the numerical results of the metallic material's permittivity from this model is used for further simulations.

Chapter 3 Theoretical Analysis of the General D/M Waveguide

3.1 Theory

3.1.1 Physical Condition Description

As shown in Fig 3-1, the dielectric/metallic waveguide array is considered to be bounded by dielectric materials on both ends of the structure. In between of the dielectric boundaries, the waveguide array consists of *N* metallic slabs and *N-1* dielectric slabs. In the general case study, the width and the refractive index of each slab are arbitrary. For convenience and consistency, the *x* axis of the coordinate system is defined as the propagation direction of the SPP modes, while the *z* axis is defined as the variation direction of the refractive index profile.

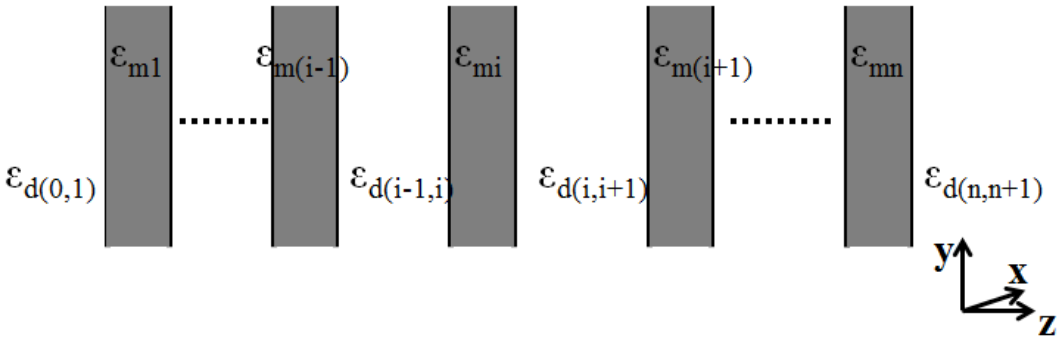


Fig 3-1: Transverse Profile of a General Dielectric/Metallic Waveguide Array

The permittivity of each metallic region, as shown above in Fig 3-1, can be expressed as ε_{mi} (for $i= 1, 2,..., N$). Similarly, the permittivity of each dielectric region is denoted as $\varepsilon_{di,i+1}$ (for $i= 0, 1, 2,..., N$). The dielectric boundaries at both sides are assumed to be extended to infinity. Similar to the notations above, the physical quantities that describe the metallic layers are denoted with a single digit subscript, while the ones of the dielectric layers are denoted with a double digit subscript in this

dissertation. The single digit of the metallic subscript indicates the specific layer which the quantity refers to. The double digits of the dielectric subscript are the serial numbers of its adjacent metallic layers. Besides, the subscription letters, *m* and *d*, are short for metallic and dielectric, respectively.

Since the structure only varies along the z-axis, the electromagnetic fields remain uniformly in the y-axis direction. As shown in the figure above, the boundaries between the i^{th} metallic layer and the $(i\text{-}1)^{th}$ dielectric layer is denoted as z_{Li}, and the boundaries between the i^{th} metallic layer and the $(i+1)^{th}$ dielectric layer is denoted as z_{Ri}. Therefore, the width of each layer can be directly derived as follow,

The width of metallic layer:

$$w_{m_i} = z_{R_i} - z_{L_i}\ (i = 1,2, \dots, N) \tag{3.1a}$$

The width of dielectric layer:

$$w_{d_{i,i+1}} = z_{L_{i+1}} - z_{R_i}\ (i = 1,2, \dots, N-1) \tag{3.1b}$$

3.1.2 Two-sided Waveform Expression

Since typical SPP modes are mainly discussed in the following chapters, only TM modes will be analyzed (no TE mode exists in such structure, see Chapter 2.4). Also, traditional waveguide modes (TWG), which exist in conventional dielectric waveguides, are not considered at this stage [56]. The physical nature of a SPP mode determines that the waveform exponentially decays in each layer of the structure, and that it decreases to zero at both infinite sides. According to the wave theory

background introduction, the scalar wave equation for a TM mode in such an array geometry can be determined as follow:

$$\frac{\partial^2 \boldsymbol{H}(y,z)}{\partial y^2} + \frac{\partial^2 \boldsymbol{H}(y,z)}{\partial z^2} + (k_o^2 \varepsilon(y,z) - \beta^2)\boldsymbol{H}(y,z) = 0 \tag{3.2}$$

In order to solve such a partial differential equation for the D/M waveguide array analytically, a set of precise waveform expressions of all possible solutions is desired. From the structural description, it can be shown that except for the two infinite dielectric layers, each single layer has two boundaries. Taking either boundary as the reference, the wave field in each layer region can be expressed differently in two ways: one based on the left-hand-side (LHS) boundary, and the other based on the right-hand-side (RHS) one. In general, two different notation systems would be set up for further mathematical derivations. The detailed waveform expressions of each region can be explicitly written as below:

For an arbitrary metallic region $z_{Li} \leq z < z_{Ri}$, the LHS boundary expression can be written as:

$$H_y(x,z) = A_i e^{k_{m_i}(z-z_{Li})} e^{i\beta x} + D_i e^{-k_{m_i}(z-z_{Li})} e^{i\beta x} \tag{3.3a}$$

$$E_x(x,z) = \frac{k_{m_i}}{\omega \varepsilon_o \varepsilon_{m_i}} \left[-iA_i e^{k_{m_i}(z-z_{Li})} + iD_i e^{-k_{m_i}(z-z_{Li})}\right] e^{i\beta x} \tag{3.3b}$$

OR the RHS boundary expression as:

$$H_y(x,z) = A_i{}' e^{k_{m_i}(z_{Ri}-z)} e^{i\beta x} + D_i{}' e^{-k_{m_i}(z_{Ri}-z)} e^{i\beta x} \tag{3.4a}$$

$$E_x(x,z) = \frac{k_{m_i}}{\omega \varepsilon_o \varepsilon_{m_i}} \left[-iA_i{}' e^{k_{m_i}(z_{Ri}-z)} + iD_i{}' e^{-k_{m_i}(z_{Ri}-z)}\right] e^{i\beta x} \tag{3.4b}$$

Similarly, for an arbitrary dielectric region $z_{Ri} \leq z < z_{Li+1}$, the LHS boundary expression can be written as:

$$H_y(x,z) = B_i e^{k_{d_{i,i+1}}(z-z_{Ri})} e^{i\beta x} + C_i e^{-k_{d_{i,i+1}}(z-z_{Ri})} e^{i\beta x} \quad (3.5a)$$

$$E_x(x,z) = \frac{k_{d_{i,i+1}}}{\omega \varepsilon_o \varepsilon_{d_{i,i+1}}} \left[-iB_i e^{k_{d_{i,i+1}}(z-z_{Ri})} + iC_i e^{-k_{d_{i,i+1}}(z-z_{Ri})} \right] e^{i\beta x} \quad (3.5b)$$

OR the RHS boundary expression as:

$$H_y(x,z) = B_i' e^{k_{d_{i,i+1}}(z_{Li+1}-z)} e^{i\beta x} + C_i' e^{-k_{d_{i,i+1}}(z_{Li+1}-z)} e^{i\beta x} \quad (3.6a)$$

$$E_x(x,z) = \frac{k_{d_{i,i+1}}}{\omega \varepsilon_o \varepsilon_{d_{i,i+1}}} \left[-iB_i' e^{k_{d_{i,i+1}}(z_{Li+1}-z)} + iC_i' e^{-k_{d_{i,i+1}}(z_{Li+1}-z)} \right] e^{i\beta x} \quad (3.6b)$$

In the expressions above, the complex amplitude of the waveform is represented by variables such as A_i, A_i' and so forth. And k_m and k_d are defined as the component of the wave vector perpendicular to the boundary between any two adjacent layers. By denoting the effective index of the plasmonic mode as n_{eff}, the wave vectors can be written as:

$$k_{m_i} = k_o \sqrt{n_{eff}^2 - \varepsilon_{m_i}} \; (i = 1,2,\dots,N) \quad (3.7a)$$

$$k_{d_{i,i+1}} = k_o \sqrt{n_{eff}^2 - \varepsilon_{d_{i,i+1}}} \; (i = 0,1,2,\dots,N) \quad (3.7b)$$

where the free space wave number $k_o = 2\pi/\lambda$. And β is the propagation constant, which can be further expressed as:

$$\beta = n_{eff} \cdot k_o \quad (3.8)$$

3.2 General D/M Waveguide Array

3.2.1 Boundary Condition Discussion

From the previous introduction, two different notation systems, which describe the identical wave fields, have been set. In each set of systems, the number of variables is *4n*+1 (*4n* amplitude variables and n_{eff}); while the number of equations, or boundary conditions, is *4n* (*2n* sets of equalizations in H_y and E_z respectively). Obviously, the mismatch of the two numbers makes it impossible to be solved directly. Therefore, seeking a universal equivalent relation in between of the two systems would become the missing piece, and make it feasible to be solved analytically. In the following analysis, the boundary conditions of the LHS expression system are firstly applied. The description of such an approach is presented as below.

Starting from the most RHS dielectric region, which extends to infinity along the positive direction of the *z*-axis, the boundary conditions in between of the adjacent layers can be applied by matching the H_y and E_z fields as follows, respectively. Since the most RHS dielectric region does not have a definite RHS boundary, all the electromagnetic fields are written in the LHS boundary expression format.

$$\lim_{z \to z_{R_n}^-} H_y(LHS) = \lim_{z \to z_{R_n}^+} H_y(LHS) \tag{3.9a}$$

$$\lim_{z \to z_{R_n}^-} E_z(LHS) = \lim_{z \to z_{R_n}^+} E_z(LHS) \tag{3.9b}$$

Where $z_{R_n}^-$ is denoted as the left-hand side of the plane $z=z_{R_n}$ and $z_{R_n}^+$ is denoted as the right-hand side of the plane $z=z_{R_n}$.

Similarly, the other *(2n-1)* sets of boundary conditions can all be expressed.

On the other hand, since the first dielectric region has no LHS boundary (extends to infinity along the negative direction of the *z*-axis), its RHS expression is used to derive its boundary condition, which relates to the first metallic region.

$$\lim_{z\to z_{L_0}^-} H_y(RHS) = \lim_{z\to z_{L_0}^+} H_y(RHS) \tag{3.10a}$$

$$\lim_{z\to z_{L_0}^-} E_z(RHS) = \lim_{z\to z_{L_0}^+} E_z(RHS) \tag{3.10b}$$

Due to the symmetry of the two wave field expression formats, solving the structure by starting the derivation from the most LHS dielectric layer will lead to an identical solution.

In order to find out the hidden relations of all the listed sets of equations, an arbitrary metallic layer, together with two adjacent dielectric layers, is selected first. Numbering the metallic layer as the i^{th} one, the detailed boundary conditions of both sides can be written as:

when $z = z_{R_i}$

$$A_i e^{k_{m_i} w_{m_i}} + D_i e^{-k_{m_i} w_{m_i}} = B_i + C_i \tag{3.11a}$$

$$\frac{k_{m_i}}{\varepsilon_{m_i}}\left(A_i e^{k_{m_i} w_{m_i}} - D_i e^{-k_{m_i} w_{m_i}}\right) = \frac{k_{d_{i,i+1}}}{\varepsilon_{d_{i,i+1}}}(B_i - C_i) \tag{3.11b}$$

when $z = z_{L_i}$

$$A_i + D_i = B_{i-1} e^{k_{d_{i-1,i}} w_{d_{i-1,i}}} + C_{i-1} e^{-k_{d_{i-1,i}} w_{d_{i-1,i}}} \tag{3.12a}$$

$$\frac{k_{m_i}}{\varepsilon_{m_i}}(A_i - D_i) = \frac{k_{d_{i-1,i}}}{\varepsilon_{d_{i-1,i}}}\left(B_{i-1} e^{k_{d_{i-1,i}} w_{d_{i-1,i}}} - C_{i-1} e^{-k_{d_{i-1,i}} w_{d_{i-1,i}}}\right) \tag{3.12b}$$

To minimize the number of the complex amplitude variables, we divide the H_y field matching equations by the E_z field matching ones. Denote that:

$$A_i = R_i \cdot D_i \quad \text{and} \quad C_i = L_i \cdot B_i \tag{3.13}$$

Here, in the LHS expression format, R_i and L_i are complex amplitude ratios of the i^{th} metallic layer and the i^{th} dielectric layer. And the four equations can be simplified as the following two:

$$\frac{k_{m_i}}{\varepsilon_{m_i}} \cdot \frac{R_i - 1}{R_i + 1} = \frac{k_{d_{i-1,i}}}{\varepsilon_{d_{i-1,i}}} \cdot \frac{e^{(2k_{d_{i-1,i}} w_{d_{i-1,i}})} - L_{i-1}}{e^{(2k_{d_{i-1,i}} w_{d_{i-1,i}})} + L_{i-1}} \tag{3.14a}$$

$$\frac{k_{m_{i-1}}}{\varepsilon_{m_{i-1}}} \cdot \frac{R_{i-1} - e^{(-2k_{m_{i-1}} w_{m_{i-1}})}}{R_{i-1} + e^{(-2k_{m_{i-1}} w_{m_{i-1}})}} = \frac{k_{d_{i-1,i}}}{\varepsilon_{d_{i-1,i}}} \cdot \frac{1 - L_{i-1}}{1 + L_{i-1}} \tag{3.14b}$$

In order to further simplify the expression, we may denote

$$X_{Li} = \frac{k_{m_i} \varepsilon_{d_{i-1,i}}}{\varepsilon_{m_i} k_{d_{i-1,i}}} \text{ and } X_{Ri} = \frac{k_{m_i} \varepsilon_{d_{i,i+1}}}{\varepsilon_{m_i} k_{d_{i,i+1}}} \tag{3.15}$$

3.2.2 Iterative Derivation

By replacing the variable L_{i-1} of equation (3.14a) into equation (3.14b) as a function of R_{i-1}, the iterative relationship between R_i and R_{i-1} is built straightforwardly. In other words, the metallic complex amplitude ratio of $(i\text{-}1)^{th}$ metallic layer, R_{i-1}, can be derived from that of the i^{th} layer. Therefore, with a determined initial value R_n, the target value R_1 could be solved with n recursions. Reminding of the previous discussion of the two ends of the array, we may have:

At the n^{th} M/D boundary, say i= n, $B_n = 0$ in equation (3.11a) and (3.11b) since the waveform is zero at the infinity. Thus equation (3.11a) and (3.11b) can be rewritten as:

$$A_n e^{k_{m_n} w_{m_n}} + D_n e^{-k_{m_n} w_{m_n}} = C_n \tag{3.16a}$$

$$\frac{k_{m_n}}{\varepsilon_{m_n}} (A_n e^{k_{m_n} w_{m_n}} - D_n e^{-k_{m_n} w_{m_n}}) = -\frac{k_{d_{n,n+1}}}{\varepsilon_{d_{n,n+1}}} C_n \tag{3.16b}$$

Dividing the equation (3.16a) by (3.16b), we may reorganize and obtain the expression of R_n as follow:

$$R_n = \frac{A_n}{D_n} = e^{(-2k_{m_n} w_{m_n})} \cdot \frac{k_{m_n} \varepsilon_{d_{n,n+1}} - \varepsilon_{m_n} k_{d_{n,n+1}}}{k_{m_n} \varepsilon_{d_{n,n+1}} + \varepsilon_{m_n} k_{d_{n,n+1}}} \tag{3.17}$$

However, the expression of R_n, as well as the iteratively derived expression of R_1, still contains the unknown variable n_{eff} in all different wave vectors. Another equation that describes the relation between R_1 and n_{eff} from a different view would be necessary.

In order to derive the other expression of R_1, the RHS format expression of the most LHS dielectric layer is applied (there is no LHS of this region). Similarly, the physical condition, which the wave field decays to zero at the negative infinite position of the *z*-axis, is used for the following derivation:

At the *1st* M/D boundary, say i= 1, $B_0' = 0$ in equation (3.6a) and (3.6b) due to the same reason as above. Thus equation (3.12a) and (3.12b) can be rewrite as:

$$A_1 + D_1 = -C_0' e^{k_{d_{0,1}} w_{d_{0,1}}} \tag{3.18a}$$

$$\frac{k_{m_1}}{\varepsilon_{m_1}} (A_1 - D_1) = -\frac{k_{d_{0,1}}}{\varepsilon_{d_{0,1}}} C_0' e^{k_{d_{0,1}} w_{d_{0,1}}} \tag{3.18b}$$

As it can be shown, when equation (3.18a) is divided by (3.18b), the non-zero variable C_0'is cancelled out from the final results. Thus, it would not introduce new unknown variables into the system. Alternatively, R_1 can be achieved as:

$$R_1 = \frac{A_1}{D_1} = \frac{k_{m_1}\varepsilon_{d_{0,1}} + \varepsilon_{m_1}k_{d_{0.1}}}{k_{m_1}\varepsilon_{d_{0,1}} - \varepsilon_{m_1}k_{d_{0.1}}} \tag{3.19}$$

Summarizing the equations above, we may observe that (n+1) formulas (including 3.17 and 3.19) have been achieved for (n+1) variables (R_1, R_2, …, R_n and n_{eff}).

$$R_1 = \frac{A_1}{D_1} = \frac{k_{m_1}\varepsilon_{d_{0,1}} + \varepsilon_{m_1}k_{d_{0.1}}}{k_{m_1}\varepsilon_{d_{0,1}} - \varepsilon_{m_1}k_{d_{0.1}}} \tag{3.19}$$

$$R_n = \frac{A_n}{D_n} = e^{(-2k_{m_n}w_{m_n})} \cdot \frac{k_{m_n}\varepsilon_{d_{n,n+1}} - \varepsilon_{m_n}k_{d_{n,n+1}}}{k_{m_n}\varepsilon_{d_{n,n+1}} + \varepsilon_{m_n}k_{d_{n,n+1}}} \tag{3.17}$$

$$\frac{(X_{Ri}+1)R_{i-1}-(X_{Ri}-1)e^{-2k_{m_i}w_{m_i}}}{(X_{Ri}+1)e^{-2k_{m_i}w_{m_i}}-(X_{Ri}-1)R_{i-1}} = e^{-2k_{d_{i-1,i}}w_{d_{i-1,i}}}\frac{(X_{Li}+1)R_i-(X_{Li}-1)}{(X_{Li}+1)-(X_{Li}-1)R_i} \tag{3.20}$$

(i= 2,3,…,n)

Each one of the (n-1) equations in the set of (3.20) is obtained cancelling L_{i-1} in between of (3.14a) and (3.14b). Altogether with equation (3.17), the effective index n_{eff} can be obtained by equalizing equation (3.20) with the iterative expression of R_1.

3.3 Regular D/M Waveguide Array

In section 3.2, a general analytical solution has been proposed in detail. For most applications or experiments, nevertheless, a regular D/M waveguide array is more interesting due to its less complexity and wider application range. By 'regular', it means that every one of the metallic layers is identical to the other ones, so is the dielectric layers in between two metallic ones. Also, such a symmetric structure is more convenient for fabrication. Therefore, the expression (3.17), (3.19) and (3.20) can be further simplified in the following steps.

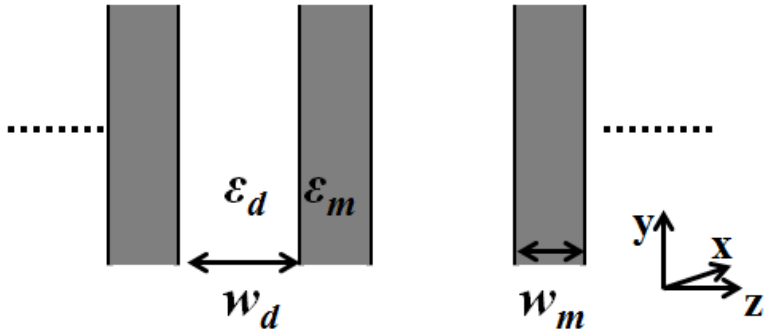


Fig 3-2: Transversal Profile of an Regular D/M Waveguide Array

In many research studies these days, two types of such waveguide arrays have been intensively studied, namely a three layer D/M waveguide array [7], and a five layer one [59]. The mode solutions of these two examples are mainly discussed in the following sections. A five layers array, usually with two metallic strips, is also named as an IMIMI (insular/metal/insular/metal/insular) waveguide. A three layers one can be either an IMI waveguide, or a MIM waveguide. The transversal profiles of these arrays are plotted as figure 3-3 and 3-4, respectively.

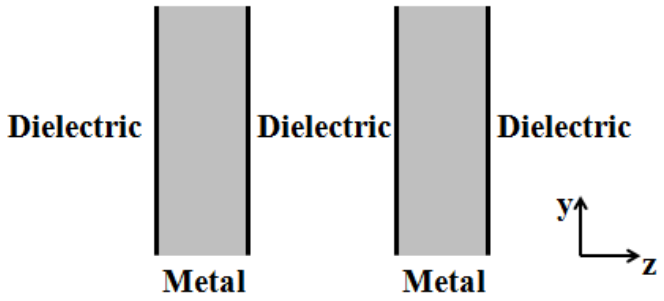


Fig 3-3 Transversal Surface of an IMIMI Waveguide

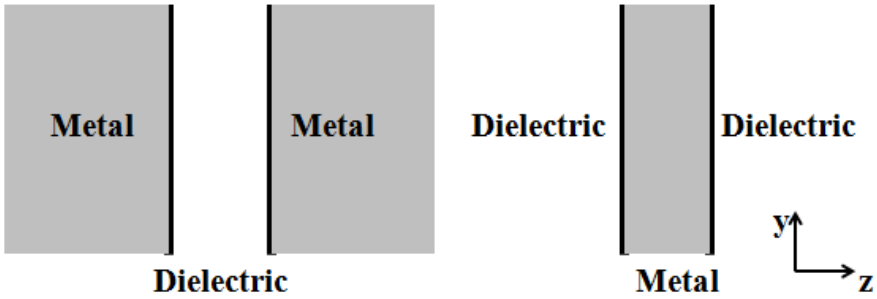


Fig 3-4: Transversal Surfaces of the MIM and IMI Waveguides

3.3.1 Analytical Solution

Since every metallic (or dielectric) layer is identical to each other, the refractive index of each one is the same. Mathematically, we have the following conditions:

$$X_{Li} = X_{Ri} = X\ (i = 1,2,\dots,n) \tag{3.21a}$$

$$\varepsilon_{m_i} = \varepsilon_m, k_{m_i} = k_m, w_{m_i} = w_m\ (i = 1,2,\dots,n) \tag{3.21b}$$

$$\varepsilon_{d_i} = \varepsilon_d,\ \ k_{d_i} = k_d,\ w_{d_i} = w_d\ (i = 0,1,2,\dots,n) \tag{3.21c}$$

Replacing the above variables into (3.17), (3.19) and (3.20), the iterative solution of the general case can be rewritten as follow:

$$R_1 = \frac{A_1}{D_1} = \frac{k_m\varepsilon_d + \varepsilon_m k_d}{k_m\varepsilon_d - \varepsilon_m k_d} \tag{3.22}$$

$$R_n = \frac{A_n}{D_n} = e^{(-2k_m w_m)} \cdot \frac{k_m\varepsilon_d - \varepsilon_m k_d}{k_m\varepsilon_d + \varepsilon_m k_d} \tag{3.23}$$

$$\frac{(R_i+1)-X(R_i-1)}{(R_i+1)+X(R_i-1)} e^{(2k_d w_d)} = \frac{\left[R_{i-1}e^{(2k_m w_m)}+1\right]-X\left[R_{i-1}e^{(2k_m w_m)}-1\right]}{\left[R_{i-1}e^{(2k_m w_m)}+1\right]+X\left[R_{i-1}e^{(2k_m w_m)}-1\right]} \tag{3.24}$$

(i= 2,3,…,n)

3.3.1.1 IMIMI Analysis

When the iterative solution is to be applied in an IMIMI array, n equals 2. By using equation (3.22), (3.23) and (3.24), two sets of solutions can be obtained from the following characteristic equation.

$$e^{(-2k_d w_d)} = \left(\frac{1 - \mathrm{X}\dfrac{(\mathrm{k_m}\varepsilon_\mathrm{d} - \mathrm{k_d}\varepsilon_\mathrm{m}) - (\mathrm{k_m}\varepsilon_\mathrm{d} + \mathrm{k_d}\varepsilon_\mathrm{m})\mathrm{e}^{2\mathrm{k_m w_m}}}{(\mathrm{k_m}\varepsilon_\mathrm{d} - \mathrm{k_d}\varepsilon_\mathrm{m}) + (\mathrm{k_m}\varepsilon_\mathrm{d} + \mathrm{k_d}\varepsilon_\mathrm{m})\mathrm{e}^{2\mathrm{k_m w_m}}}}{1 + \mathrm{X}\dfrac{(\mathrm{k_m}\varepsilon_\mathrm{d} - \mathrm{k_d}\varepsilon_\mathrm{m}) - (\mathrm{k_m}\varepsilon_\mathrm{d} + \mathrm{k_d}\varepsilon_\mathrm{m})\mathrm{e}^{2\mathrm{k_m w_m}}}{(\mathrm{k_m}\varepsilon_\mathrm{d} - \mathrm{k_d}\varepsilon_\mathrm{m}) + (\mathrm{k_m}\varepsilon_\mathrm{d} + \mathrm{k_d}\varepsilon_\mathrm{m})\mathrm{e}^{2\mathrm{k_m w_m}}}} \right)^2 \tag{3.25}$$

The characteristic equation indicates that two different modes of SPPs can be propagated through this array. The specific characteristic equations are listed as below.

$$\tanh\left(\mathrm{k_d} \cdot \mathrm{w_d}/2\right) = \mathrm{X}\frac{(\mathrm{k_m}\varepsilon_\mathrm{d} - \mathrm{k_d}\varepsilon_\mathrm{m}) - (\mathrm{k_m}\varepsilon_\mathrm{d} + \mathrm{k_d}\varepsilon_\mathrm{m})\mathrm{e}^{2\mathrm{k_m w_m}}}{(\mathrm{k_m}\varepsilon_\mathrm{d} - \mathrm{k_d}\varepsilon_\mathrm{m}) + (\mathrm{k_m}\varepsilon_\mathrm{d} + \mathrm{k_d}\varepsilon_\mathrm{m})\mathrm{e}^{2\mathrm{k_m w_m}}} \tag{3.26a}$$

$$\coth\left(\mathrm{k_d} \cdot \mathrm{w_d}/2\right) = \mathrm{X}\frac{(\mathrm{k_m}\varepsilon_\mathrm{d} - \mathrm{k_d}\varepsilon_\mathrm{m}) - (\mathrm{k_m}\varepsilon_\mathrm{d} + \mathrm{k_d}\varepsilon_\mathrm{m})\mathrm{e}^{2\mathrm{k_m w_m}}}{(\mathrm{k_m}\varepsilon_\mathrm{d} - \mathrm{k_d}\varepsilon_\mathrm{m}) + (\mathrm{k_m}\varepsilon_\mathrm{d} + \mathrm{k_d}\varepsilon_\mathrm{m})\mathrm{e}^{2\mathrm{k_m w_m}}} \tag{3.26b}$$

3.3.1.2 IMI or MIM Analysis

As for a three layer array, namely the IMI or MIM waveguide, the analytical solution is more straightforward. By equalizing (3.22) and (3.23), the characteristic equation can be obtained directly.

$$e^{(-2k_c w_c)} = \left(\frac{k_m \varepsilon_d + \varepsilon_m k_d}{k_m \varepsilon_d - \varepsilon_m k_d}\right)^2 \tag{3.27}$$

The subscript *c* in the equation represents the core layer material of the array. If it is a MIM array, then *c* represents *d*, or dielectric. Otherwise, it is *m*, or metallic. Also, from each case of the characteristic equation, two solutions can be obtained. Normally, these two solutions are named as symmetric mode (*s*-mode) and anti-symmetric mode (*a*-mode).

3.3.2 Numerical Simulation & Discussions

Although difficult to be solved by hand calculation, the characteristic equations listed above provide an intuitive approach for numerical simulation. The results of such a simulation would be the effective indexes of such an array with a certain number of layers. In this section, both arrays with five layers (IMIMI) and three layers (MIM) would be mainly examined. The hidden relations in between of these two structures are presented afterwards.

In the following sections of this chapter, the numerical results are simulated in the material model described as follows. The metallic layer is simulated as silver (Ag), and the dielectric layer is simulated as silicon (Si), with the central layer width equal to

100nm. The wavelength variation has been considered in determining the permittivity of different materials by using the Drude Model.

3.3.2.1 Numerical Solution of IMIMI Waveguide

The effective indexes of the *s*-mode and the *a*-mode in a regular IMIMI waveguide are solved based on the analytical equations from section 3.2, and plotted in fig *3-5a* to fig *3-5d*. The real part and the imaginary part of each mode are plotted separately.

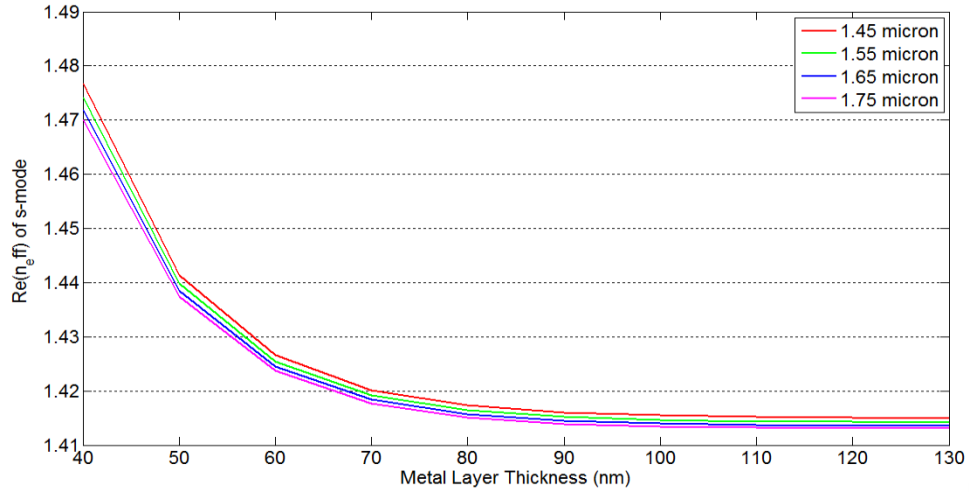


Fig 3-5a: Real Part of the Effective Index of the Symmetric Mode in IMIMI

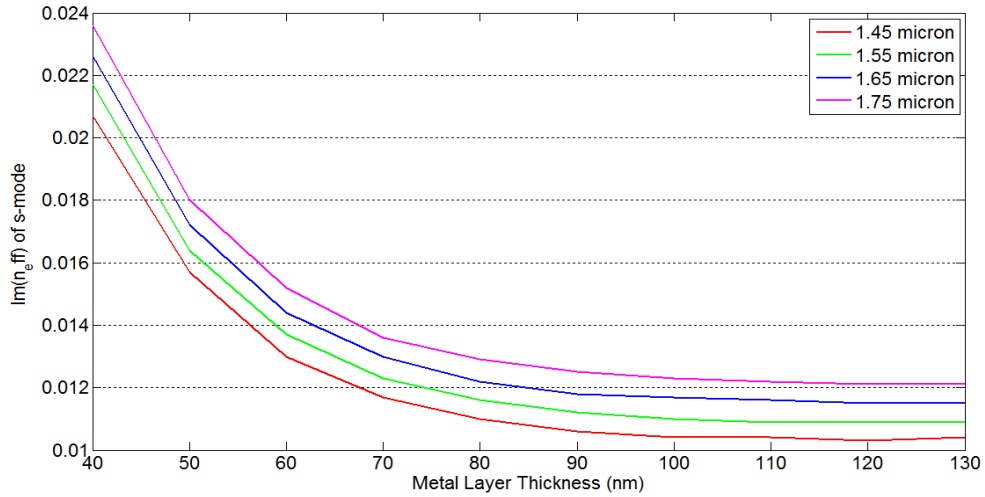


Fig 3-5b: Imaginary Part of the Effective Index of the Symmetric Mode in IMIMI

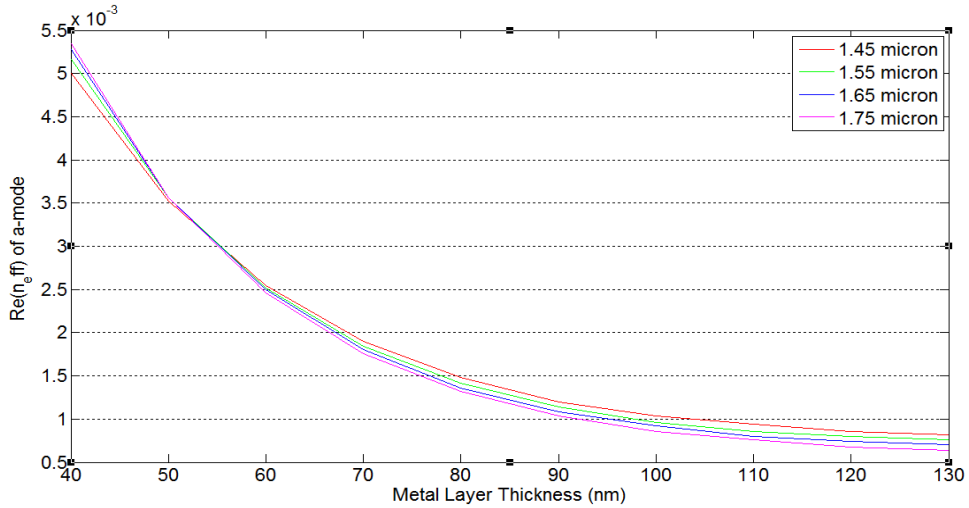


Fig 3-5c: Real Part of the Effective Index of the Anti-Symmetric Mode in IMIMI

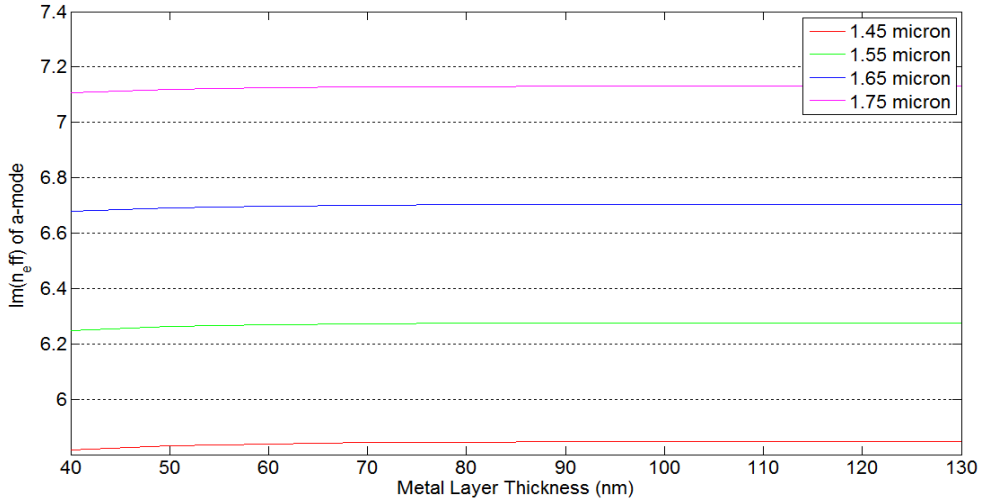


Fig 3-5d: Imaginary Part of the Effective Index of the Anti-Symmetric Mode in IMIMI

The vertical axes of each figure are the numerical values of the corresponding variable, while the horizontal axes represent the variation range of the metal layer thickness (from 30nm to 70nm). The core silicon layer remains as a constant value of 100nm, and the boundary silicon layers are set to be extending to infinity. Four different wavelengths are selected around 1.55μm.

On one side, the four figures reveal the different variations of both the real and imaginary part of each mode (s-mode or a-mode) according to the width of the two metallic layers in the IMIMI waveguide. The curves in the first three figures are monotonously decreasing, while the last curve in fig *3-6d* is slightly increasing.

On the other hand, these four sets of curves reveal a common characteristic which carries an important physical meaning and would be further discussed in chapter 4.

As shown from each figure, when the thickness reaches 60nm (0.04λ), the effective indexes of different modes become stable, and approaching a certain constant. By simple calculation, the approached value is the complex solution, or the effective index, of a MIM structure array with the same central dielectric layer and two infinite silver layers at the sides. Therefore, an IMIMI five layer structure can be regarded as a MIM three layer structure when the metal layer thickness reaches the threshold value. In this case, as well as the following sections, the threshold value is 0.04λ.

Also, for each set of wavelengths (1.55μm is the main focus), the variation trends, as well as the approaching values, of the *s*-mode and *a*-mode are different. This means that the *a*-mode and *s*-mode of the same wavelength propagate differently in the same array. The *s*-mode has a relatively low imaginary part; while the real part values of the *a*-mode approach to zero when the metal layer thickness exceeds the threshold value. This might cause the differences in amplitude decay and phase velocity through mode propagation, and would provide possibilities of designing new SPP devices.

3.3.2.2 Numerical Solution of MIM Waveguide

Similar to that of the IMIMI waveguide, the simulation of the MIM waveguide are run under the condition that a core silicon layer is bounded by two infinite metallic layers. The materials of each layer remain the same. Instead of varying the metallic layer thickness, the core layer thickness is altered from 100nm to 300nm in this section, so that the influence of the core silicon layer can be discussed independently.

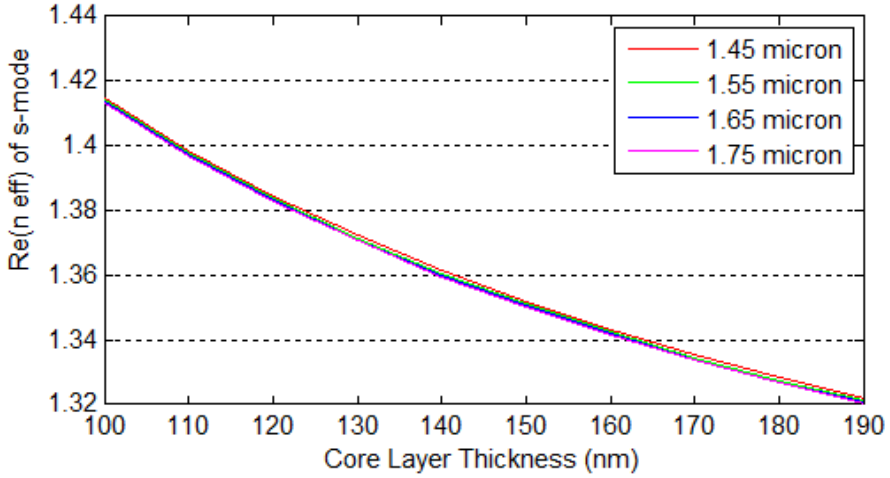


Fig 3-6a: Real Part of the Effective Index of the Symmetric Mode in MIM

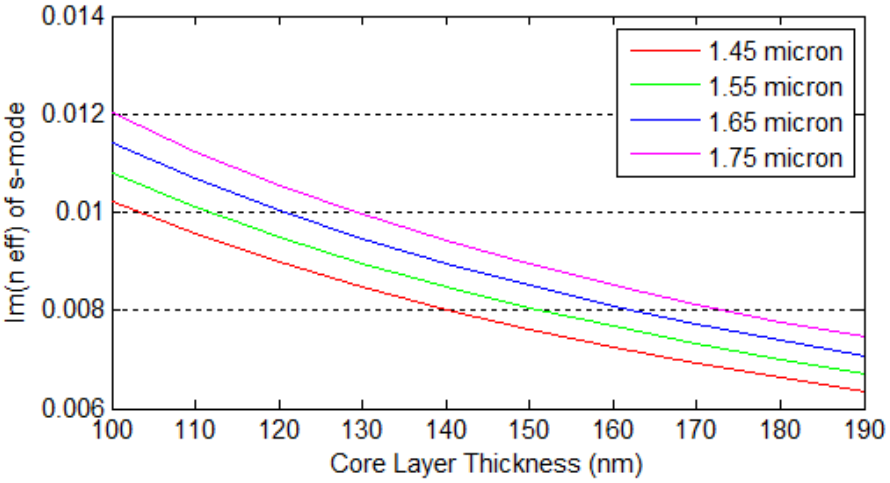


Fig 3-6b: Imaginary Part of the Effective Index of the Symmetric Mode in MIM

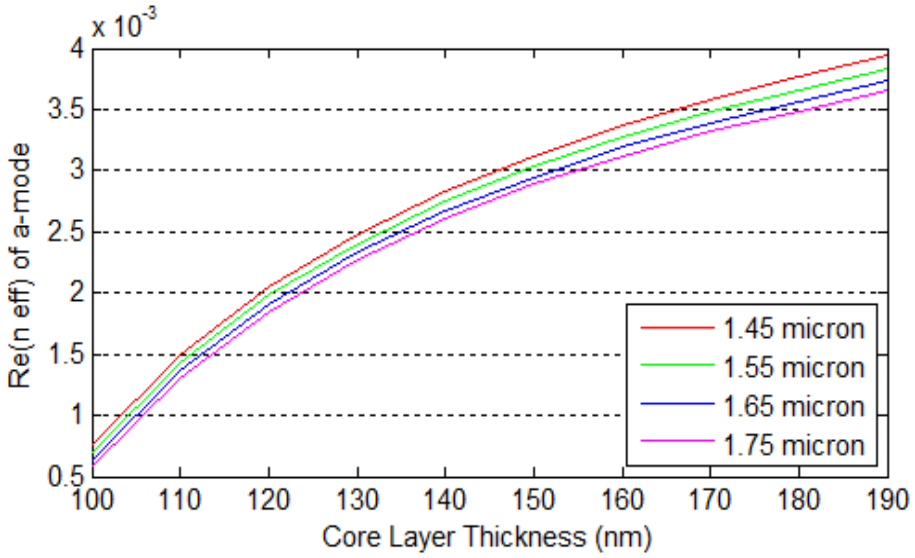


Fig 3-6c: Real Part of the Effective Index of the Anti-Symmetric Mode in MIM

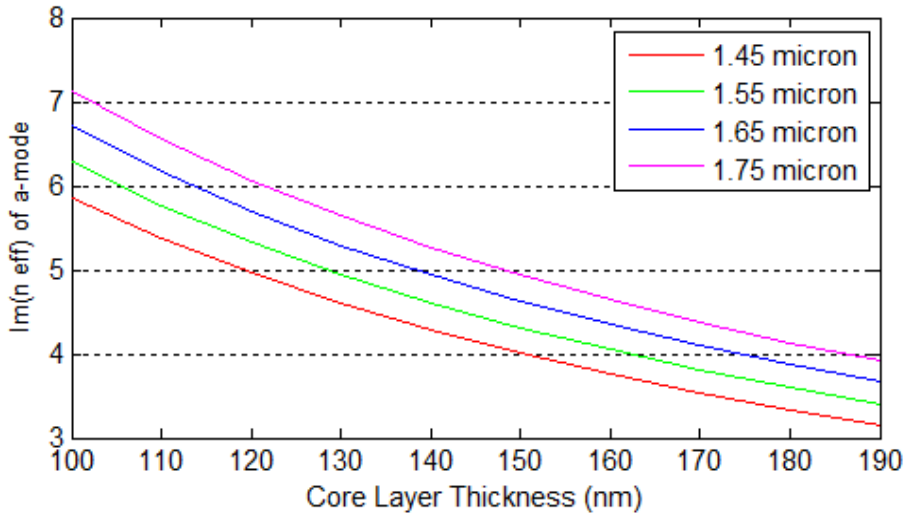


Fig 3-6d: Imaginary Part of the Effective Index of the Anti-Symmetric Mode in MIM

Comparing the initial numerical values of the four figures (core layer thickness equal to 100nm) with the approaching values of the four figures in section 3.3.2.1, it can be found that the two sets of numbers, if the same wavelength is selected, are nearly equalized. It proves that, if the metallic layer thickness of a regular IMIMI

waveguide exceeds a certain threshold value, the effective index seen by the input plasmonic modes (both *s*-mode and *a*-mode) are the same as that of an identical MIM waveguide. Such property could provide an accurate threshold parameter for simplifying such waveguide structures to be studied.

3.3.2.3 Analytical Description of the Structural Variation

As shown from the mode solutions of an IMIMI waveguide under different physical conditions, both variations have transformed the IMIMI structure into new stable waveguide structures.

Section 3.3.2.1 introduced the first type of waveguide variation by broadening the core layer (dielectric material) of an IMIMI waveguide to a quite large value. Physically speaking, if the core layer is broad enough to be considered as an infinite layer, then the IMIMI waveguide has been divided into two identical IMI waveguides.

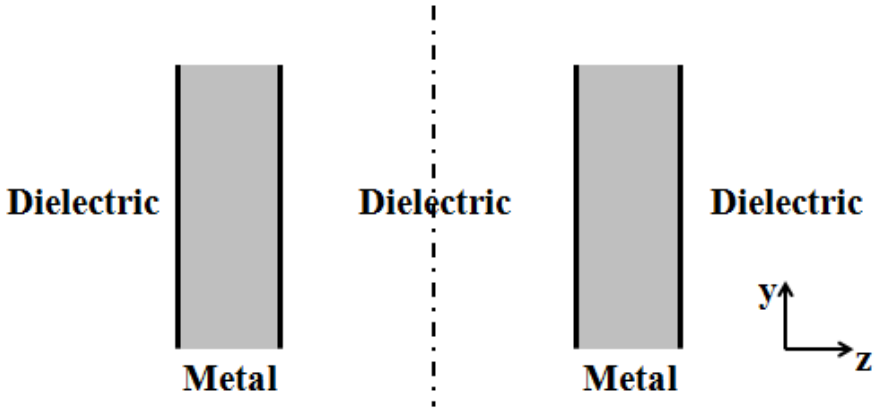


Fig 3-7: An IMIMI Waveguide with Large Core Layer Thickness

Mathematically, when the width of the core layer thickness is large enough to be considered as infinite, the characteristic equation of the IMIMI waveguide (3.25) can

be transformed into that of an IMI waveguide (3.27) as follow.

$$e^{(-2k_d w_d)} \to 0 \text{ when } w_d \to \infty$$

$$\therefore \frac{(k_m\varepsilon_d - k_d\varepsilon_m) - (k_m\varepsilon_d + k_d\varepsilon_m)e^{2k_m w_m}}{(k_m\varepsilon_d - k_d\varepsilon_m) + (k_m\varepsilon_d + k_d\varepsilon_m)e^{2k_m w_m}} = \frac{k_d\varepsilon_m}{k_m\varepsilon_d}$$

$$\therefore e^{(-2k_m w_m)} = \left(\frac{k_m\varepsilon_d + \varepsilon_m k_d}{k_m\varepsilon_d - \varepsilon_m k_d}\right)^2$$

In the other case, section 3.3.2.2, the widths of both metallic layers are very large. An infinitely thick metallic layer would completely confine the plasmonic mode within it. So, the IMIMI waveguide is turned into a MIM waveguide finally. The derivation of the characteristic equations is presented as below.

$$(k_m\varepsilon_d + k_d\varepsilon_m)e^{2k_m w_m} \gg (k_m\varepsilon_d - k_d\varepsilon_m) \quad \text{when } w_m \to \infty$$

$$\therefore \frac{(\mathrm{k_m\varepsilon_d - k_d\varepsilon_m}) - (\mathrm{k_m\varepsilon_d + k_d\varepsilon_m})\mathrm{e}^{2\mathrm{k_m w_m}}}{(\mathrm{k_m\varepsilon_d - k_d\varepsilon_m}) + (\mathrm{k_m\varepsilon_d + k_d\varepsilon_m})\mathrm{e}^{2\mathrm{k_m w_m}}} \cong -1$$

$$\therefore e^{(-2k_d w_d)} = \left(\frac{k_m\varepsilon_d + \varepsilon_m k_d}{k_m\varepsilon_d - \varepsilon_m k_d}\right)^2$$

Thus, equations (3.26a) and (3.26b) return to the format of equation (3.25). It indicates that the structure is the same as a three layer MIM waveguide. The previous figures (fig 3-5a~fig 3-5d) simulate this physics situation and determine the threshold thickness of the metal layer.

3.4 Analytical Scrutinize of the Methodology

Before introducing the comprehensive numerical simulation of a general D/M waveguide array in the following chapter, the established characteristic equations of several widely applied D/M waveguide arrays can be used to enhance the validity of the analytical work introduced in section 3.2. By matching the different analytical approaches together, the new methodology would be successfully verified and would provide a wide application range in the general D/M waveguide array structure.

3.4.1 General IMI Waveguide

When *n=1*, the D/M Waveguide Array is actually a three layer IMI structure (Insulator/Metal/Insulator), which has an established characteristic equation as

$$e^{(-2k_{m_1}w_{m_1})} = \frac{k_{m_1}\varepsilon_{d_{0,1}} + \varepsilon_{m_1}k_{d_{0.1}}}{k_{m_1}\varepsilon_{d_{0,1}} - \varepsilon_{m_1}k_{d_{0.1}}} \frac{k_{m_1}\varepsilon_{d_{1,2}} + \varepsilon_{m_1}k_{d_{1,2}}}{k_{m_1}\varepsilon_{d_{1,2}} - \varepsilon_{m_1}k_{d_{1,2}}} \tag{3.27'}$$

It is the direct equalization of equation (3.17) and (3.19) by the iterative analytical solution. If the two dielectric layers are symmetric ($\varepsilon_{d_{0,1}} = \varepsilon_{d_{1,2}}$), which is the physical condition of a regular IMI waveguide, equation (3.27') can be further expressed into the characteristic equations of the two types of modes discussed in section 3.3, namely symmetric mode (*s*-mode) and anti-symmetric mode (*a*-mode).

$$\begin{aligned} tanh\left(\frac{k_m \cdot w_m}{2}\right) &= -\frac{k_m\varepsilon_d}{k_d\varepsilon_m} \\ coth\left(\frac{k_m \cdot w_m}{2}\right) &= -\frac{k_m\varepsilon_d}{k_d\varepsilon_m} \end{aligned} \tag{3.25'}$$

3.4.2 General IMIMI Waveguide

When *n=2*, the D/M Waveguide Array is equivalent to a five layer IMIMI structure (Insulator/ Metal/ Insulator/ Metal/ Insulator). The characteristic equation of a general IMIMI waveguide is not widely used, while that of an identical one has been introduced in section 3.3.

By putting the expression (3.19) and (3.17) into equation (3.20), we may obtain

$$\frac{(R_2+1)-X_{L2}(R_2-1)}{(R_2+1)+X_{L2}(R_2-1)}e^{\left(2k_{d_{1,2}}w_{d_{1,2}}\right)}=\frac{\left[R_1e^{(2k_{m_1}w_{m_1})}+1\right]-X_{R1}\left[R_1e^{(2k_{m_1}w_{m_1})}-1\right]}{\left[R_1e^{(2k_{m_1}w_{m_1})}+1\right]+X_{R1}\left[R_1e^{(2k_{m_1}w_{m_1})}-1\right]} \qquad (3.20')$$

where R_1 and R_2 can be obtained from equation (3.19) and (3.17).

If we expand the internal dielectric region between two metal layers to become infinitely large, the term $e^{(2k_{d_{1,2}}w_{d_{1,2}})}$ becomes infinite in its real part, which gives

$$R_1=e^{(-2k_{m_1}w_{m_1})}\cdot\frac{k_{m_1}\varepsilon_{d_{1,2}}-\varepsilon_{m_1}k_{d_{1,2}}}{k_{m_1}\varepsilon_{d_{1,2}}+\varepsilon_{m_1}k_{d_{1,2}}} \qquad (3.19')$$

Mathematically, this situation has become the same one discussed in the last section (IMI structure). It perfectly translates the physical meaning that an infinite dielectric layer separates the five layer system into two three layer ones. The approach of solving R_2 is similar.

3.5 Conclusion

In this chapter, the analytical study of a general D/M waveguide array has been proposed. By defining the two-sided boundary expressions for the wave fields within each layer of the waveguide, the general array system has been solved with the special boundary conditions at both ends of its transversal profile.

In order to match with the current applications more closely, the general D/M waveguide structure has been further simplified into an identical array. Therefore, a more concise expression of the analytical solution has been presented. Furthermore, numerical solutions of different plasmonic modes in two widely used identical arrays, the IMIMI waveguide and the MIM waveguide, have been plotted with MATLAB and have been discussed in detail. The relationship between the two waveguide implied by the variation trends of both the real part and the imaginary part of the numerical solutions has also been analyzed quantitatively. Taking the wavelengths around $1.55\mu m$ into consideration, when the core dielectric layer is 100nm, the threshold value for the metal layer thickness has been decided as around 0.04λ. Beyond the threshold value, the analytical solution of the MIM waveguide can be directly applied into the IMIMI waveguide study.

Finally, the numerical relations have been further scrutinized by mathematical derivations in section 3.4. Also, the perfect match between the iterative solution and the published analytical equations has successfully provided a more convincing basis for the following chapters.

Chapter 4 Numerical Analysis of the General D/M Waveguide

4.1 Introduction

Based on the iterative approach of solving a general D/M waveguide analytically, a series of important parameters in SPPs communication applications can be simulated and examined numerically. In this chapter, two vital parameters, including the energy confinement, as well as the propagation loss, are mainly discussed due to the following reasons.

In current plasmonic communication techniques, D/M waveguide arrays propagate different SPP modes at a sub-wavelength dimension. It indicates that the array structure is capable of confining a plasmonic mode within a sub-wavelength dimension range in the transversal surface of the array.

Whereas the propagation range is comparably large (~hundreds of microns in plasmonic communications), the propagation loss along the metallic material could affect the accuracy of signal transmission.

Based on the iterative-type analytical solution from chapter 3, the conventional study of these two important parameters would be expanded from a new aspect.

In order to achieve a better communication performance, a smaller light energy confining area, together with a lower propagation loss over the whole propagation distance, is preferred. And the interested parameters would become the intuitive references for industrial array designs.

4.2 Energy Confinement

From the analytical discussion shown in chapter 3, the characteristic equations for the modes in a three layer D/M waveguide array, namely an IMI waveguide, or a MIM waveguide, are relatively simple and straight forward to be applied. However, the two boundary layers, in real cases, cannot be designed with infinite thicknesses. The numerical discrepancy caused by finite thicknesses should be determined accurately. And from the study of the identical D/M waveguide in chapter 3.3, the similarity of an IMIMI waveguide and a MIM waveguide increases, when the metallic layer thickness in enlarged gradually. Intuitively, a numerical expression can be derived to describe the variation relation.

As shown from the following graph, the core layers of an IMIMI waveguide can be defined as the three layers in the middle of the structure. And the ratio of the energy confined in the core layers *CR* can be expressed as:

$$CR = \frac{E_{core}}{E_s} \tag{4.1a}$$

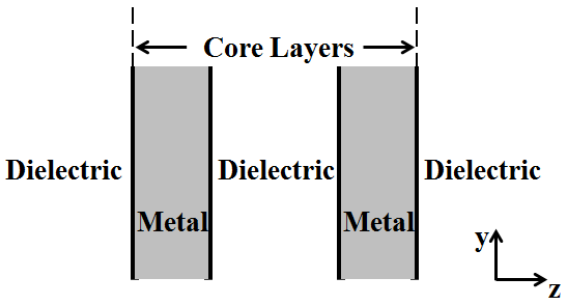


Fig 4-1: Transversal Definition of the Core Layers in IMIMI Waveguide

4.2.1 Time-averaged Power of Signal Transmission

Since the frequency of a plasmonic signal is usually quite high (~10^{14} Hz), the period time is relatively short, in terms of the period of a transmitting signal. Therefore, the time-averaged power P_s of a transmitted signal is usually considered as the vital parameter in determining signal energy E_s at the receiver end of a communication channel. And equation (4.1a) can also be derived as (4.1b)

$$E_s = P_s \cdot t_s \tag{4.2}$$

$$CR = \frac{E_{core}}{E_s} = \frac{P_{core}}{P_s} \tag{4.1b}$$

From the electromagnetic field theory [55], the time-averaged power P_s of a time-harmonic wave can be calculated by the following formula [50].

$$P_s = \frac{1}{2}\oint \boldsymbol{P}_{ave} d\boldsymbol{s} = \frac{1}{2}\oint Re(\boldsymbol{E} \times \boldsymbol{H}^*) d\boldsymbol{s} \tag{4.3}$$

By applying the geometry description of the waveguide in chapter 3, the $\boldsymbol{E}$ field, $\boldsymbol{H}$ field and the time-averaged Poynting vector $\boldsymbol{P}_{ave}$ of a propagating mode in a D/M waveguide array can be described by equations (4.4a), (4.4b) and (4.4c) ($\boldsymbol{i}$,$\boldsymbol{j}$ and $\boldsymbol{k}$ are denoted as the unit vectors of a Cartesian Coordination).

$$\boldsymbol{H}^* = {H_y}^*(x,z) \cdot \boldsymbol{j} \tag{4.4a}$$

$$\boldsymbol{E} = E_x(x,z) \cdot \boldsymbol{i} + E_z(x,z) \cdot \boldsymbol{k} \tag{4.4b}$$

$$\boldsymbol{P}_{ave} = \frac{1}{2} Re\big(-E_z(x,z) \cdot {H_y}^*(x,z) \cdot \boldsymbol{i} + E_x(x,z) \cdot {H_y}^*(x,z) \cdot \boldsymbol{k}\big) \tag{4.4c}$$

From the expression above, two directional power fluxes exist when the plasmonic signal is being propagated in an array. According to the previous notations, the

directions of the two fluxes are along the *x*-axis (***i***) and the *z*-axis (***k***), respectively. Since the flux along the *z*-axis is perpendicular to the transmission direction, it is considered as power loss that will not be received as transmitted signals. Therefore, the first term of the $\boldsymbol{P}_{ave}$ equation (4.4c) is regarded as the time-averaged power of signal transmission. By setting up the specific waveguide structure, its mathematical expression can be further derived and discussed in the next part of this section.

4.2.2 Time-averaged Power Ratio of Adjacent Layers

From the conclusion of 4.2.1, it is appropriate to calculate the ratio of the time-averaged power of signal transmission in order to determine the energy distribution over the transversal surface.

$$P_{transmission} = \frac{1}{2}\iint Re\left(-E_z(x,z)\cdot {H_y}^*(x,z)\right)\cdot dy\cdot dz \tag{4.5}$$

By integrating the pointing vector of each layer on the cross-section surface of an IMIMI waveguide, the ratio between the confined power (within the three core layers) and the whole power would be obtained. The variation of the ratio, achieved by changing the physical conditions of the array, represents the property of energy confinement quantitatively.

Generally, an arbitrary metallic layer is placed in between the two dielectric layers in the D/M waveguide array. By applying the iterative approach of solving the effective index, the relative time-averaged transmission power ratio of two adjacent layers can also be achieved analytically.

By substituting (2.10c) into (4.2), the Poynting vector can be expressed as:

$$\boldsymbol{P}_{ave} = \frac{1}{2} Re\left(-\frac{\beta}{\omega \varepsilon_o \varepsilon_i} H_y(x,z) \cdot {H_y}^*(x,z) \right) \cdot \boldsymbol{i} \tag{4.5}$$

Recall the LHS boundary expressions in chapter 3, and select the input side of a waveguide (x=0) as the surface to be discussed, the equation can be expanded if the i^{th} metallic layer is discussed. Besides, an identical D/M waveguide array case is applied, so that the physical meaning of it would be enhanced.

$$\left|\boldsymbol{P}_{m_i}\right| = \left| \frac{\beta}{2\omega \varepsilon_o \varepsilon_m} \left[A_i e^{k_m (z - z_{Li})} + D_i e^{-k_m (z - z_{Li})} \right] \cdot \left[A_i e^{k_m (z - z_{Li})} + D_i e^{-k_m (z - z_{Li})} \right]^* \right| \tag{4.5}$$

Where the complex terms can be replaced with

$$A_i = a_re_i + i \cdot a_im_i \tag{4.6a}$$

$$D_i = d_re_i + i \cdot d_im_i \tag{4.6b}$$

$$k_m = k_re_m + i \cdot k_im_m \tag{4.6c}$$

Similarly, the power of the i^{th} dielectric layer can be written as:

$$\left|\boldsymbol{P}_{d_i}\right| = \left| \frac{\beta}{2\omega \varepsilon_o \varepsilon_d} \left[B_i e^{k_d (z - z_{Ri})} + C_i e^{-k_d (z - z_{Ri})} \right] \cdot \left[B_i e^{k_d (z - z_{Ri})} + C_i e^{-k_d (z - z_{Ri})} \right]^* \right| \tag{4.7}$$

Where the complex terms can be replaced with

$$B_i = b_re_i + i \cdot b_im_i \tag{4.8a}$$

$$C_i = c_re_i + i \cdot c_im_i \tag{4.8b}$$

$$k_d = k_re_d + i \cdot k_im_d \tag{4.8c}$$

Simply substituting the complex expansions into the original formula, equation (4.5) and (4.7) can be rewritten as:

$$\begin{aligned}\left|\boldsymbol{P}_{m_i}\right| = \Bigg|\frac{\beta}{2\omega\varepsilon_o\varepsilon_m}\{&\left(a_re_i{}^2 + a_im_i{}^2\right)\mathrm{e}^{2k_re_{\mathrm{m}}(\mathrm{z}-z_{Li})} \\ &+ \left(d_re_i{}^2 + d_im_i{}^2\right)\mathrm{e}^{-2k_re_{\mathrm{m}}(\mathrm{z}-z_{Li})} \\ &+ 2\mathrm{Cos}[2k_im_{\mathrm{m}}(\mathrm{z}-z_{Li})](a_re_i d_re_i + a_im_i d_im_i) \\ &+ 2\mathrm{Sin}[2k_im_{\mathrm{m}}(\mathrm{z}-z_{Li})](a_re_i d_im_i - a_im_i d_re_i)\}\Bigg|\end{aligned} \tag{4.9}$$

$$\begin{aligned}\left|\boldsymbol{P}_{d_{i,i+1}}\right| = \Bigg|\frac{\beta}{2\omega\varepsilon_o\varepsilon_d}\{&\left(b_re_i{}^2 + b_im_i{}^2\right)\mathrm{e}^{2k_re_{\mathrm{d}}(\mathrm{z}-z_{Ri})} \\ &+ \left(c_re_i{}^2 + c_im_i{}^2\right)\mathrm{e}^{-2k_re_{\mathrm{d}}(\mathrm{z}-z_{Ri})} \\ &+ 2\mathrm{Cos}[2k_im_{\mathrm{d}}(\mathrm{z}-z_{Ri})](b_re_i c_re_i + b_im_i c_im_i) \\ &+ 2\mathrm{Sin}[2k_im_{\mathrm{d}}(\mathrm{z}-z_{Ri})](b_re_i c_im_i - b_im_i c_re_i)\}\Bigg|\end{aligned} \tag{4.10}$$

However, the amplitude variables are omitted in the previous iterative approach. In order to further simplify (4.9) and (4.10), and provide a systematic analysis of such a structure, the amplitude ratios R_i and L_i are applied as follows.

$$R_i = R_re_i + i \cdot R_im_i \tag{4.11a}$$

$$L_i = L_re_i + i \cdot L_im_i \tag{4.11b}$$

Thus, by $A_i = R_i \cdot D_i$ and $C_i = L_i \cdot B_i$, we may have

$$a_re_i = d_re_i \cdot R_re_i - d_im_i \cdot R_im_i \tag{4.12a}$$

$$a_im_i = d_re_i \cdot R_im_i + d_im_i \cdot R_re_i \tag{4.12b}$$

$$c_re_i = b_re_i \cdot L_re_i - b_im_i \cdot L_im_i \tag{4.12c}$$

$$c_im_i = b_re_i \cdot L_im_i + b_im_i \cdot L_re_i \tag{4.12d}$$

Substituting these relations into (4.9) and (4.10), we may have

$$\left|\boldsymbol{P}_{m_i}\right| = \left|\frac{\beta}{2\omega\varepsilon_o\varepsilon_m}|D_i|^2\left\{|R_i|^2 e^{2k_re_m(z-z_{Li})} + e^{-2k_re_m(z-z_{Li})} + 2Cos[2k_im_m(z-z_{Li})]R_re_i + 2Sin[2k_im_m(z-z_{Li})]R_im_i\right\}\right| \tag{4.13}$$

$$\left|\boldsymbol{P}_{d_{i,i+1}}\right| = \left|\frac{\beta}{2\omega\varepsilon_o\varepsilon_d}|B_i|^2\left\{e^{2k_re_d(z-z_{Ri})} + |L_i|^2 e^{-2k_re_d(z-z_{Ri})} + 2Cos[2k_im_d(z-z_{Ri})]L_re_i + 2Sin[2k_im_d(z-z_{Ri})]L_im_i\right\}\right| \tag{4.14}$$

Thus, the power ratio of adjacent layers of the i[th] metal layer and its RHS dielectric layer $AR_{i,i+1}$ can be expressed as:

$$AR_{i,i+1} = \frac{P_{trans_m}(x=0)}{P_{trans_d}(x=0)} = \frac{\int_{z_{L_i}}^{z_{R_i}} Re(\boldsymbol{P_{m_i}}\cdot\boldsymbol{i})dz}{\int_{z_{R_i}}^{z_{L_{i+1}}} Re(\boldsymbol{P_{d_{i,i+1}}}\cdot\boldsymbol{i})dz} \tag{4.15}$$

In which the amplitude ratio can be obtained from (3.11) as:

$$\frac{|D_i|}{|B_i|} = \left|\frac{1+L_i}{e^{-k_m w_m} + e^{k_m w_m} R_i}\right| \tag{4.16}$$

In addition, a special case should be treated differently. As the initial layer (RHS dielectric boundary layer) of the iterative algorithm, it does not have a RHS boundary. The component along the propagation direction of its Poynting vector can be easily derived as:

$$\left|\boldsymbol{P}_{d_{n-1,n}}\right| = \left|\frac{\beta}{2\omega\varepsilon_o\varepsilon_d}|C_n|^2 e^{-2k_re_d(z-z_{Rn})}\right| \tag{4.14'}$$

Therefore, an iterative algorithm of determining the time-averaged power ratio in an identical D/M waveguide array (4.1b) is proposed as (4.13), (4.14), (4.15) and (4.16). In the IMIMI waveguide, the confinement ratio *CR* can be further expressed as:

$$CR = \frac{P_{core}}{P_s} = \frac{1+2\cdot AR_{1,2}}{1+2\cdot AR_{1,2}(1+AR_{2,3}^{-1})}\cdot 100\% \tag{4.17}$$

4.2.3 Simulation Results & Discussion

In this section, the previous formulas of the time-averaged transmission power would be applied into an IMIMI waveguide. The confinement ratio parameter, *CR*, is obtained by comparing the power in the core three layers with that of the total array. Furthermore, by varying the thicknesses of the different layers in the IMIMI waveguide, the threshold values which ensure at least 99% of the transmission power is included in the core layers can be determined for both *s*-mode and *a*-mode.

4.2.3.1 Variation of Metal Layer Thickness

The variation of the two symmetric metal layers in an IMIMI waveguide is first considered as the parametric variable. At the same time, the core layer thickness is set as 100nm, the material is selected as silicon and silver, and the wavelength remains at 1.55μm.

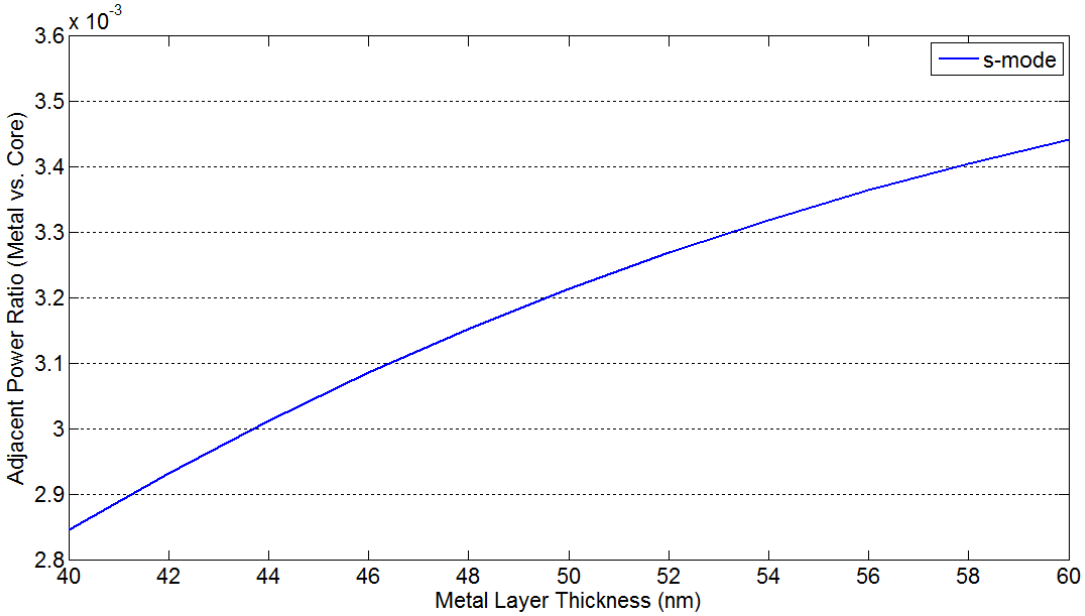


Fig 4-2: The Adjacent Power Ratio of the Two Metal Layers and the Core Layer

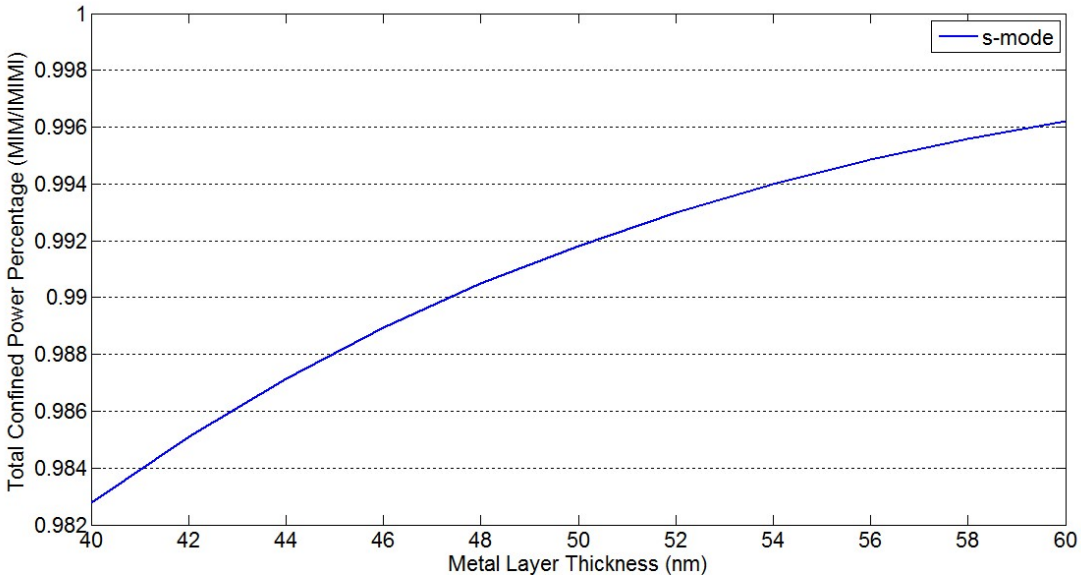


Fig 4-3: The Confined Energy (in the core layers) Percentage Against Different Metal Layer Thickness (nm)

As seen from figure 4-2, for the *s*-mode the time-averaged power in the two metal layers is only about 0.3% of the power in the core layer, even though the total thickness of two metal layers (80nm~120nm) is about the same as that of the core one. It indicates that most of the energy is confined in the core layer of an IMIMI waveguide.

In figure 4-3, the total confined energy percentage in the core and metal layers of the *s*-mode is plotted. In the given simulation conditions, when the metal layer thickness reaches about 48nm, over 99% of the total transmission power is confined in the core three layers. Compared with the result in section 3.3.2.1, once the effective index can be numerically approximated by the characteristic equations of the MIM waveguide, the percentage of the energy confined within the core three layers has reached 99% for *s*-mode.

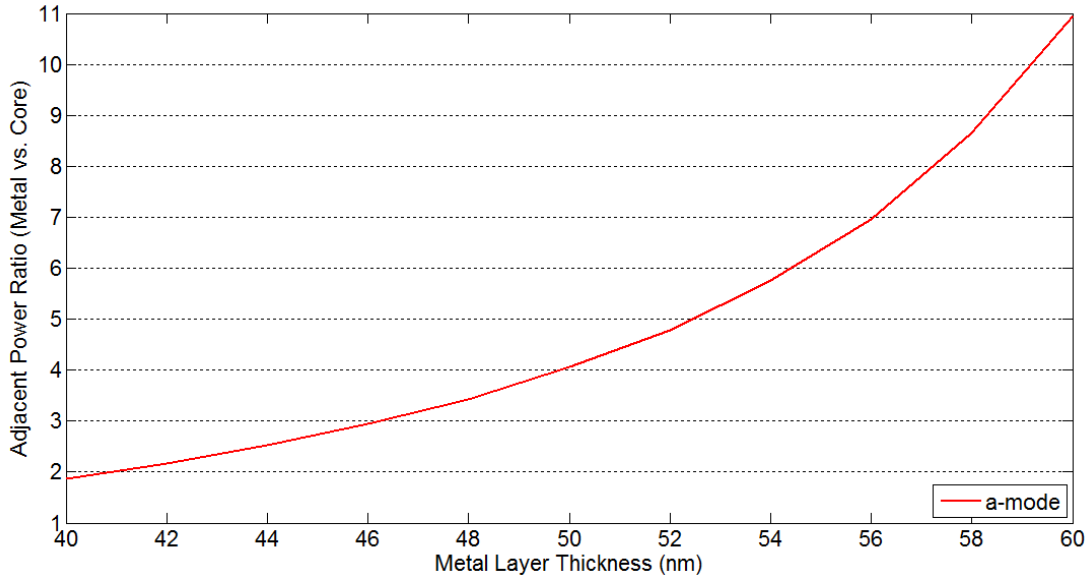


Fig 4-4: The Adjacent Power Ratio of the Two Metal Layers and the Core Layer

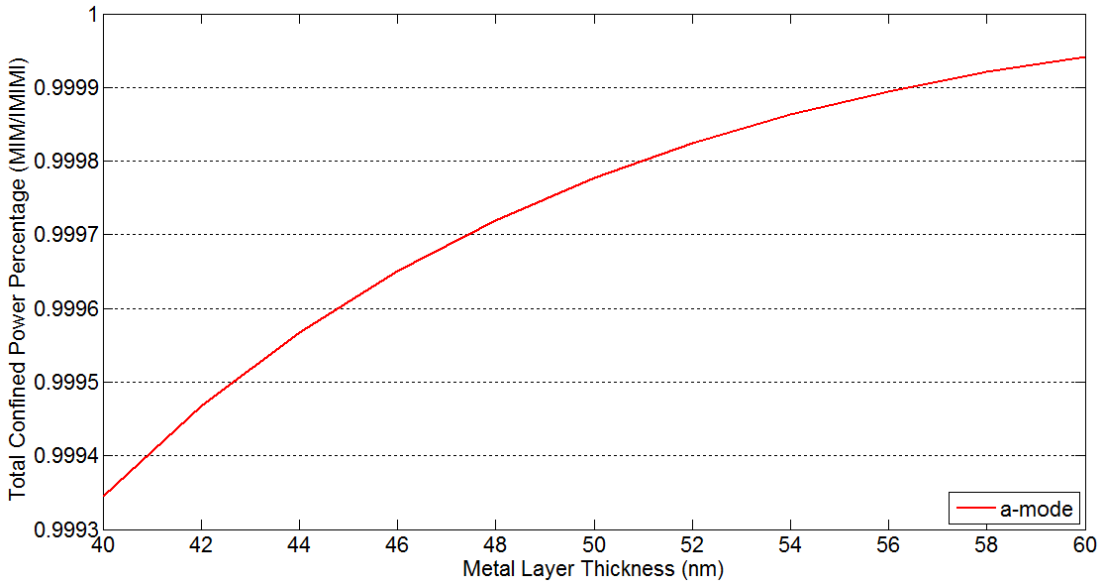


Fig 4-5: The Confined Energy (in the core layers) Percentage Against Different Metal Layer Thickness (nm)

As for the *a*-mode, the time-averaged power ratio of the two metal layers and the core layer is to the contrary with that of the *s*-mode. The power in the metal layers raise from 1.8 times (w_m=40nm) of that in the core layer to 11 times (w_m=60nm). It

shows that the majority of the confined energy exists in both metal layers, instead of the core.

Similarly, the total confined power percentage in the core and metal layers of the *s*-mode is plotted in figure 4-5. When the metal layer thickness ranges from 40nm to 60nm, the total percentage is remained above 99.9%. Compared with the percentage of the *s*-mode, the *a*-mode has a better performance in terms of transversal energy confinement.

4.2.3.2 Variation of Core Layer (Dielectric) Thickness

The variation of the core layer in an IMIMI waveguide is considered as the parametric variable in this section. Meanwhile, the metal layer thickness's variation range remains the same as in section 4.2.4.1, the material is selected as silicon and silver, and the wavelength remains at 1.55μm.

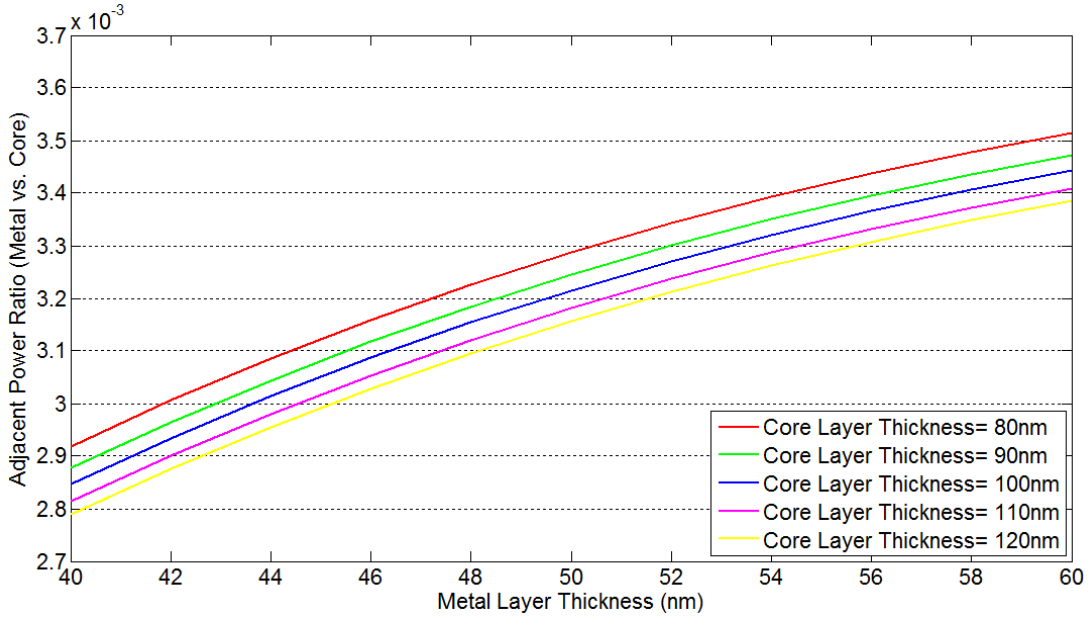


Fig 4-6: The Adjacent Power ratio of the Two Metal Layers and the Core Layer

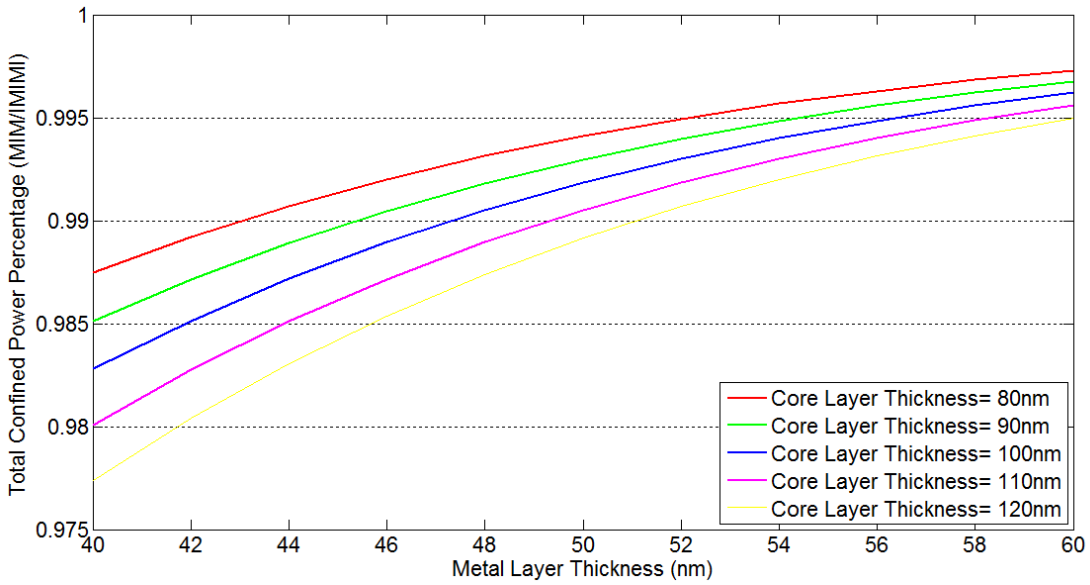


Fig 4-7: The Confined Energy (in the core layers) Percentage with Different Core Layer Thickness (nm)

As seen from the above two figures, the energy distribution (or confinement) trends of the *s*-mode with different core layer thicknesses (ranges from 80nm to 120nm) are the same. The time-averaged power percentage in the two metal layers is still about 0.3% of the power in the core layer. The additional characteristic that can be observed is that, when the core layer is enlarged, a higher ratio of transmission power is confined in itself.

Furthermore, from figure 4-7, the threshold metal layer thickness of each core layer condition varies. Similar to the last section, the threshold is set so that 99% of the transmission power is confined within the core three layers of the waveguide. Numerically, when the core layer is increased from 80nm to 120nm, the threshold value is also enlarged, from around 43nm (~50.25% of the core layer thickness) to

around 51nm (~40.25% of the core layer thickness). The absolute value is increasing while the relative percentage is lowered.

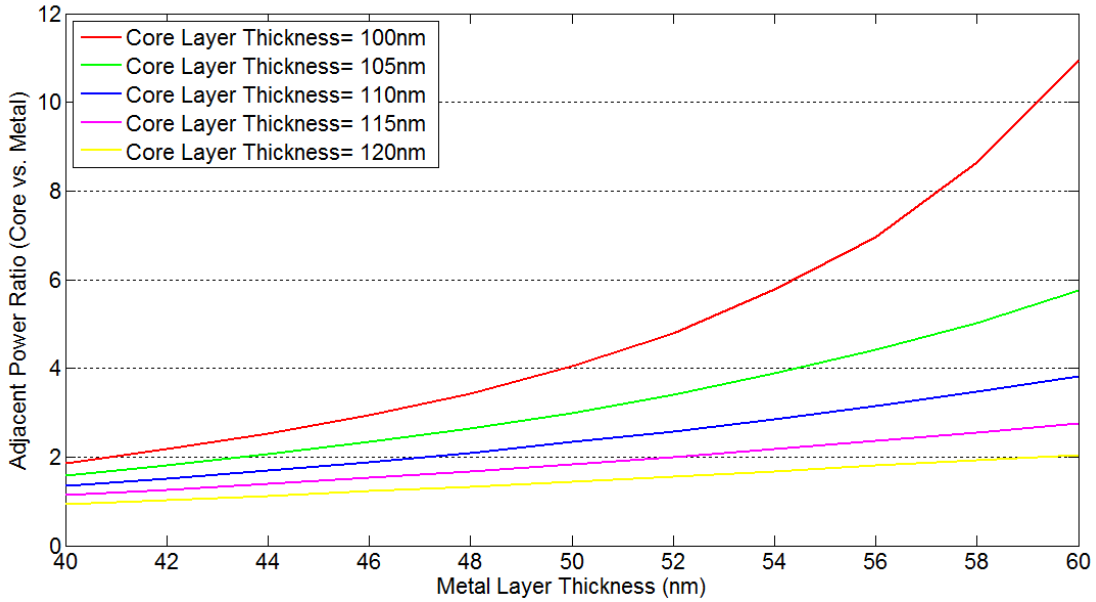


Fig 4-8: The Adjacent Power Ratio of the Two Metal Layers and the Core Layer

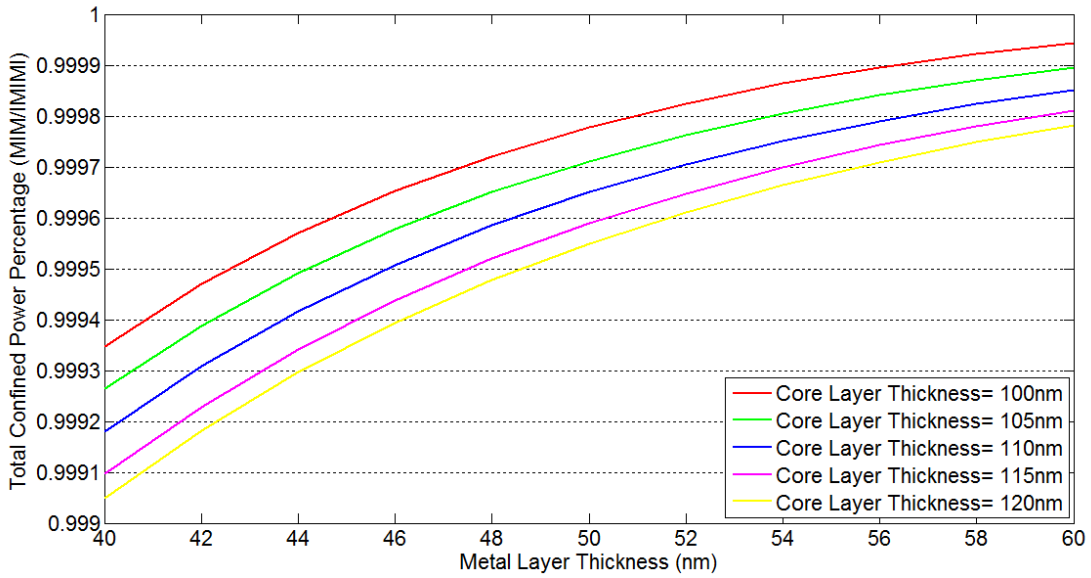


Fig 4-9: The Confined Energy (in the core layers) Percentage against Different Metal Layer Thickness (nm)

Similarly, the variation trends of the *a*-mode are the same with that discussed above. As the core layer thickness increases, the time-averaged power ratio of the two metal layers and the core layer is decreasing. It implies that, the narrower the core layer is, the more energy is confined in the metal layer for the *a*-mode.

4.3 Propagation Loss

As discussed in section 4.2.1, two directions of power fluxes exist when a plasmonic signal is propagated in an array. The one along the cross-section direction would finally dissipate in the form of heat or radiation. The other one along the channel direction is the focus of most researches [20]. The lossy nature of the D/M waveguide array would affect the signal energy level at the receivers' end. In this section, the propagation loss, which measures the power loss along the signal transmission direction, is mainly studied and discussed.

4.3.1 Time-Averaged Power Loss

In section 4.2, the energy confinement ranges of all propagating SPP modes on the input side transversal surface (x=0) are fully discussed. Since the positive x-axis has been defined as the signal transmission direction of such waveguides, the term $exp(i\beta x)$ of the waveform expression should be taken into account in determining the power loss along propagation, where $\beta = n_{eff} \cdot k_o$ and can be further expanded as:

$$s-mode: \beta_s = \beta_{sr} + i \cdot \beta_{si} \tag{4.17a}$$

$$a-mode: \beta_a = \beta_{ar} + i \cdot \beta_{ai} \tag{4.17b}$$

Expanded from the equations (4.4) derived in 4.2.1 and 4.2.2, the x-axis term is introduced as follow so that a simulation model for propagation loss is determined.

$$P_{transmission}(x) = \oiint \boldsymbol{P}_{ave}(x,z) \cdot \boldsymbol{i} \cdot dy \cdot dz \tag{4.4}$$

$$where\ \boldsymbol{P}_{ave}(x,z) = \frac{1}{2} Re\left(-\frac{\beta}{\omega \varepsilon_o \varepsilon_i} H_y(z) \cdot e^{-i\beta x} \cdot {H_y}^*(z) \cdot \left(e^{-i\beta x}\right)^*\right) \cdot \boldsymbol{i} \tag{4.5}$$

$$e^{-i\beta_{s,a}x} = \mathrm{e}^{-(\beta_{s,a_i}x)} \cdot \left[\cos\left(\beta_{s,a_r}x\right) + i \cdot \sin(\beta_{s,a_r}x)\right] \tag{4.18a}$$

$$\left(e^{-i\beta_{s,a}x}\right)^{*} = \mathrm{e}^{-(\beta_{s,a_i}x)} \cdot \left[\cos\left(\beta_{s,a_r}x\right) - i \cdot \sin(\beta_{s,a_r}x)\right] \tag{4.18b}$$

By substituting (4.18a), (4.18b) and (4.5) into (4.4), the time-averaged power at a certain propagation distance *x* can be expressed as:

$$P_{transmission}(x) = \oiint \boldsymbol{P}_{ave}(z) \cdot \mathrm{e}^{-2(\beta_{s,a_i}x)} \cdot \boldsymbol{i} \cdot dy \cdot dz \tag{4.19}$$

By dividing the time-averaged power at a certain propagation distance with that of the input side, the propagation loss is simply:

$$L_{dB} = 10\, log_{10} \frac{P_{transmission}(x)}{P_{transmission}(0)} = 10\, log_{10}\, e^{-2(\beta_{s,a_i}x)} \tag{4.20}$$

Or, it is equivalent to measure the loss with the physical term propagation length L_p:

$$L_p = \frac{1}{2k_0 \cdot Im(n_{eff})}\ (m^{-1}) \tag{4.21}$$

4.3.2 Simulation Results & Discussion

In order to have a more intuitive understanding of the propagation loss for both *s*-mode and *a*-mode, the relative transmission power is plotted as a function of the propagation length as follows. Note that the transmission power at the initial position (input) of the channel is normalized.

For consistency, the structure of the waveguide is simulated with 100nm core layer, two 50nm metal layers, and two 100m (infinite) dielectric layers. The wavelength and the materials remain the same.

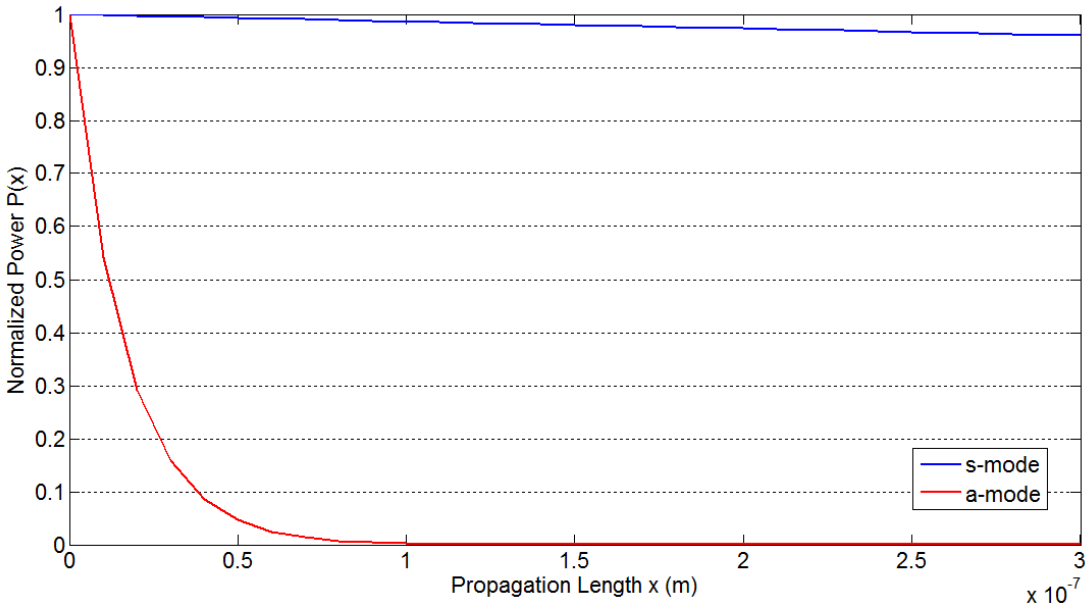


Fig 4-10: Normalized Transmission Power of s-mode and a-mode in IMIMI Waveguide

As seen from figure 4-10, the transmission power of the *s*-mode is well conserved during the initial 300nm propagation; while the *a*-mode suffers a significant loss. This matches with the numerical simulations of chapter 3, which presents that the imaginary part of the *a*-mode is much larger than that of the *s*-mode. Combining the numerical results from section 4.2, the higher loss rate comes from the fact that a much larger percentage of the *a*-mode energy is confined in the metallic layer, instead of the core (dielectric) layer.

In addition, this figure indicates that, with the given waveguide structure, the *a*-mode energy decays swiftly to zero within a propagation range of 100nm.

By looking into the wave propagation of each mode in detail, the waveguide structure parameters also play an important role. For the both modes, with significantly different propagation loss rates, the propagation length L_p can be obtained as follows.

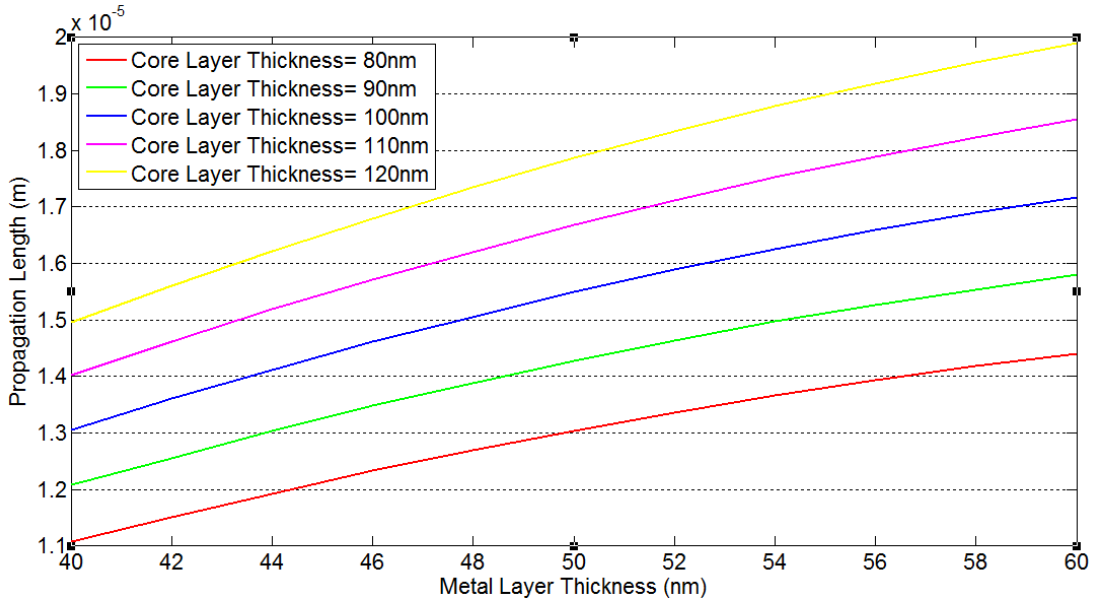


Fig 4-11: Propagation Length of s-mode with Different IMIMI Waveguide Structures

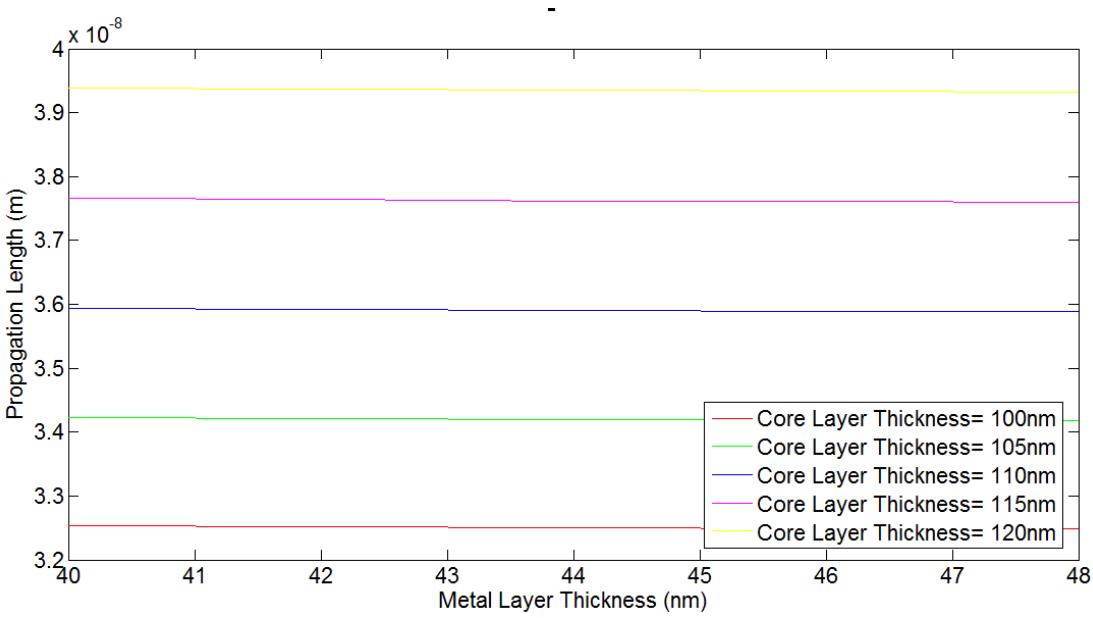


Fig 4-12: Propagation Length of a-mode with Different IMIMI Waveguide Structures

It can be observed from the two figures that, the *s*-mode, with a lower propagation loss rate, has a much longer propagation length than that of an *a*-mode, when the same IMIMI waveguide is considered. For s-modes, the propagation length raises either

when the metal layer thickness is enlarged, or when the core layer thickness is enlarged. Besides, the slopes of the curves in figure 4-11 are rather uniform.

For the *a*-modes, the propagation length is insensitive to the variation of the metal layer thickness. However, when the core layer thickness is increased by 20% (from 100nm to 120nm), the numerical result is increased by about 25%. Such phenomenon indicates that most of the energy is confined and consumed on the inner side of both metal layers, so that the variation of the metal layer thickness does not affect the performance a lot. Once the thickness of the core layer is increased, more transmission power would exist in the core (dielectric) layer with a lower loss rate. Thus, the propagation length would be increased.

4.4 Conclusion

In this chapter, the crucial parameters in applying the D/M waveguides, mainly the IMIMI waveuguide, into plasmonic communication devices have been listed and studied based on the iterative-type analytical solution of such structures derived in chapter 3.

As one of the most important parameters in integrated optics, the capability of energy confinement in such a waveguide has been defined as the ratio of the energy within the core layer to that of the total energy. By deriving the analytical expression of the time-averaged power ratio in adjacent layers of a general D/M waveguide array, the energy confinement ratio has been provided with an accurate expression. Later in section 4.2, the numerical simulation of such an expression was discussed under different structural conditions. When the metal layer thickness satisfied the threshold value condition in chapter 3, over 99.9% of the transmission energy in both s-mode and a-mode would be confined within the core layers.

In section 4.3, the propagation loss properties of different modes in the IMIMI waveguide have been simulated. By using the conventional parameter, the propagation length, the lossy nature of the anti-symmetric mode has been shown quantitatively. Also, the variation of the propagation loss along different structural parameters of the waveguide has also been presented.

Chapter 5 Coupling Effect between Different Plasmonic Modes

5.1 Introduction

In this chapter, the coupling effect between the different modes in a D/M waveguide array, which has been studied in previous chapters, is mainly analyzed. By selecting the IMIMI waveguide as an example, the coupling effect of its two major modes, namely the *s*-mode and the *a*-mode, could be applied to achieve a sub-wavelength range coupling length. Compared with the conventional plasmonic couplers [5], the reduction in the coupling length will provide the possibility of manufacturing a coupler with smaller size and lead to more potential applications in the area of integrated optics.

From the power loss analysis in chapter 4, it can be concluded that, given the same array structure, the *a*-mode has a much shorter propagation length than that of the *s*-mode. Therefore, the a-mode is named as Short-Range-Surface-Plasmon-Polaritons (SRSPPs) [60], and the s-mode is named as Long-Range-Surface-Plasmon-Polaritons (LRSPPs) [61]. It is also the significant difference in the complex propagation constants of the two modes that provides the possibility of coupling the transmission power into the target output area within a sub-wavelength range.

This chapter begins with the normal-mode analysis, which has been widely used in plasmonic coupler designs [13]. By considering the specific waveguide structure, the specific conditions, under which the coupling length could be significantly shortened, are analyzed first. Then the numerical simulation is presented for further verification. Finally, the performance of the coupler is discussed with its crucial parameters.

5.1.1 Structural Description

Before expanding the detailed analysis, a brief illustration of the proposed coupler based on a regular IMIMI waveguide array would be helpful. The following figures show the structure layout from the longitudinal and the transversal directions.

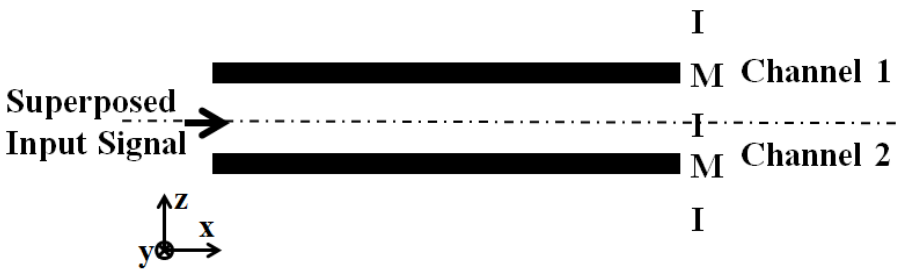


Fig 5-1: Longitudinal Profile of A Duo-Channel SPP Coupler

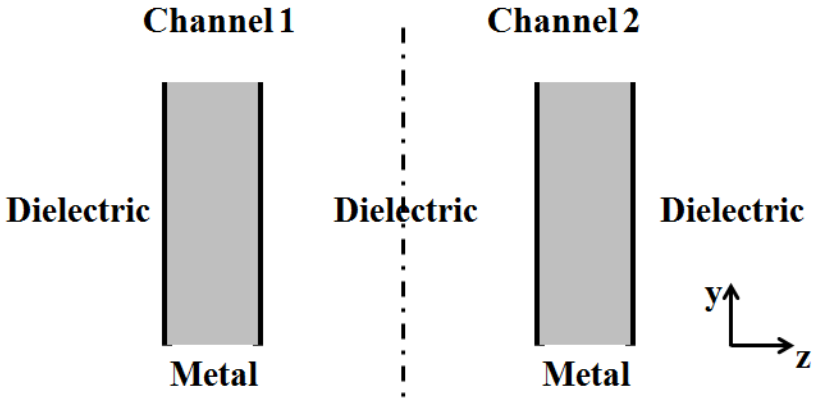


Fig 5-2: Transverse Profile of A Duo-Channel SPP Coupler

Figure 5-1 shows the longitudinal profile of such a waveguide. With two identical metal layers placed at two sides of the core dielectric layer, the waveguide is divided into two identical channels. The capital letters *M* and *I* represent the material (metal and insular) of each layer, respectively. The x-axis is defined as the direction of signal propagation and the y-z plane is defined as the transversal surface, with a profile diagram shown as figure 5-2.

According to the division of the two channels in figure 5-1, channel 1 consists of layer I, II, and the left-hand half of layer III from figure 5-2, and the rest of the transversal surface is defined as channel 2. The following table shows the specific parameters of the coupler when the SPP wavelength remains at 1.55μm.

Coupler Channel	Channel 1		Channel 2		
	Layer I	Layer II	Layer III	Layer IV	Layer V
Width	*infinite*	w_d	w_m	w_d	*infinite*
z-axis range	$-\infty \sim -(w_m/2+w_d)$	$-(w_m/2+w_d) \sim -w_m/2$	$-w_m/2 \sim w_m/2$	$w_m/2 \sim (w_m/2+w_d)$	$(w_m/2+w_d) \sim \infty$
Permittivity	1.4	-95.431+i*9.515	1.4	-95.431+i*9.515	1.4

Table 5-1: Dimensions and Material Properties of the Coupler

5.1.2 Mechanism

In the normal-mode analysis, if the plasmonic signal is guided into the coupler from one of the two channels, it can be regarded as the superposition of the LRSPP and SRSPP modes. Due to the different propagation constants of the two modes, the transmitting signal power will be transferred between the two channels. However, the SRSPP is so lossy that its power usually vanishes swiftly in the channel. Thus, it is difficult to directly couple such two modes. In order to overcome the difficulty, adding additional SRSPP signal power would be a potential solution proposed in this chapter. With a relatively larger input power, the SRSPP would be capable of propagating over a distance comparable with that of the LRSPP.

5.2 Approximated Analytical Model

5.2.1 Transversal Superposition

The superposition of the two modes in the coupler is expressed in the first place, so that the approximation condition can be later derived. By re-writing the *H*-field waveform equations of the two modes as follow:

$$H_y^{LRSPP}(x,z) = A^{LRSPP}(x)\varphi_{trans}^{LRSPP}(z)e^{i\beta_{LRSPP}x} \tag{5.1a}$$

$$H_y^{SRSPP}(x,z) = A^{SRSPP}(x)\varphi_{trans}^{SRSPP}(z)e^{i\beta_{SRSPP}x} \tag{5.1b}$$

where A^{LRSPP} and A^{SRSPP} are the complex amplitudes of the *H*-fields, φ functions are the transversal waveforms, and the $e^{i\beta x}$ terms are the phasors along the propagation direction. We may define the initial condition of the system by setting x=0.

According to the superposition, the *H*-field waveform equations of the plasmonic signal at the input end (initial condition) can be directly expressed as:

$$H_y^{LRSPP}(0,z) = A^{LRSPP}\varphi_{trans}^{LRSPP}(z) \tag{5.2a}$$

$$H_y^{SRSPP}(0,z) = A^{SRSPP}\varphi_{trans}^{SRSPP}(z) \tag{5.2b}$$

Before discussing the peak amplitude variables of each mode, A^{LRSPP} and A^{SRSPP}, the transversal waveform equations should be carefully compared. From the study of chapter 3, the fundamental modes both exponentially decay in each layer of the waveguide. It is the differences of the transversal decay rates in each layer, denoted as k_m and k_d in equation (3.7), that determine the accuracy of the superposition. If the absolute transversal waveforms $|\varphi_{trans}^{LRSPP}(z)|$ and $|\varphi_{trans}^{LRSPP}(z)|$ are identical in a

certain layer, we may directly use the peak amplitude values in the superposition calculation. Considering the waveguide structure as in Table 5-1, the complex transversal decay rates (TDRs) can be calculated by using the iterative approach equations (3.22) ~ (3.24).

TDRs	Dielectric Layer TDR k_d	Metal Layer TDR k_m
LRSPP	$2.51*10^6+8.03*10^4$	$4.0016*10^7-i*1.95*10^6$
SRSPP	$7.66*10^7+3.17*10^6$	$4.0012*10^7-i*1.93*10^6$

Table 5-2: Transversal Decay Rates of Each Layer in the IMIMI Coupler

As shown in Table 5-2, the decay rates in the metal layers (layer II and IV) are numerically close for both modes. Thus, we might achieve an approximated cancellation of the two waveforms in these layers when their amplitudes are the same. The following figures illustrate the description above intuitively.

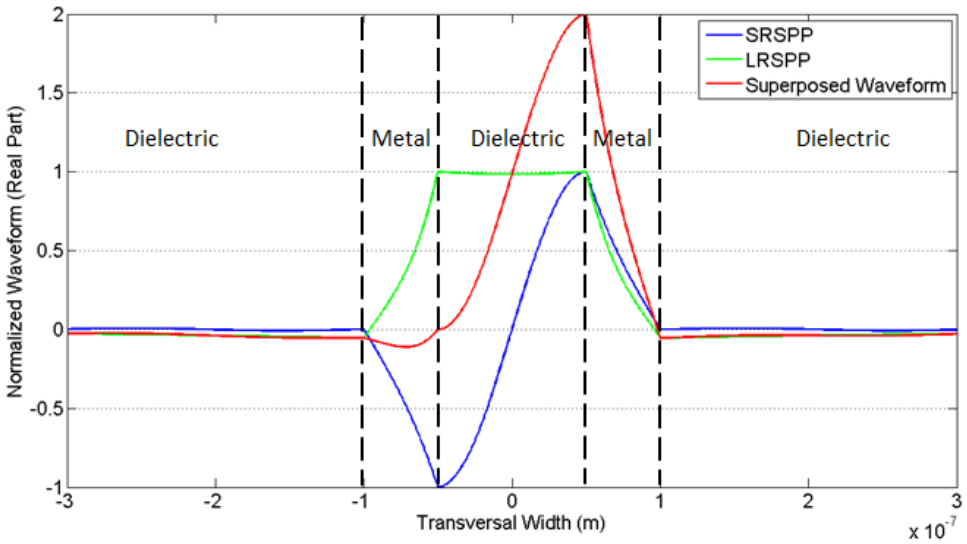


Fig 5-3a: Numerical Plotting of the Real Part of the Transversal Superposition between Amplitude-Normalized LRSPP and SRSPP

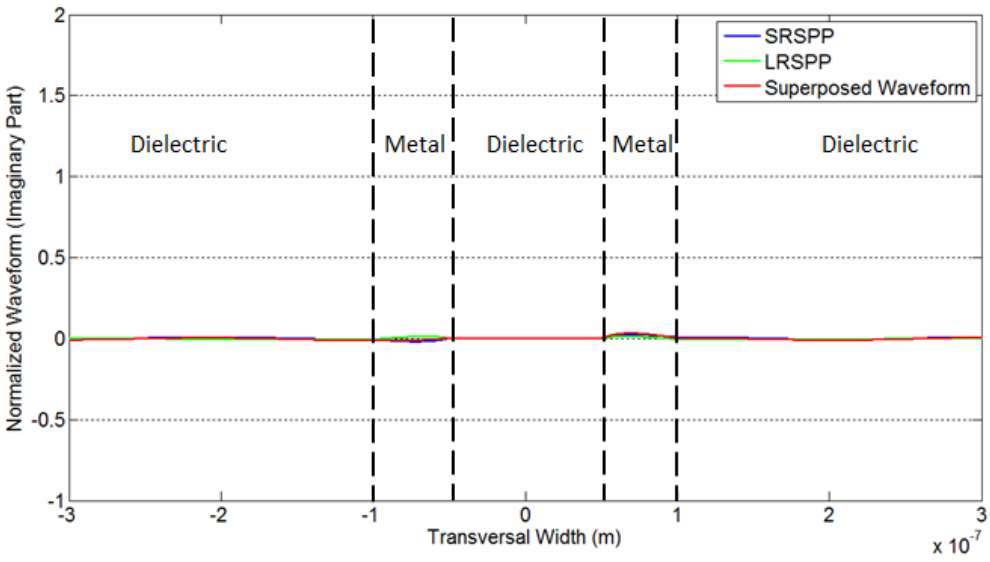


Fig 5-3b: Numerical Plotting of the Imaginary Part of the Transversal Superposition between Amplitude-Normalized LRSPP and SRSPP

It can be first observed from figure 5-3 that, comparing with the real parts of the waveforms, the imaginary parts are negligible. In figure 5-3a, it shows that the real parts of the waveforms are nearly zero in one of the metal layers (layer II). Physically, it indicates that the total cancellation of the waveform in one channel can be approximately described by the total cancellation of the peak amplitude values in the metal layer of that channel. Mathematically, we may have the following equations to express the physical condition of the expected output from the coupler.

$$H_y^{LRSPP}(x,z) + H_y^{SRSPP}(x,z) = 0, \text{ when } z < -50\text{nm} \qquad (5.3a)$$

Or equivalently, it can be approximated by:

$$A^{SRSPP} e^{i\beta_{SRSPP}x} + A^{LRSPP} e^{i\beta_{LRSPP}x} = 0 \qquad (5.3b)$$

Due to the symmetry of the transversal geometric layout of the waveguide, if the input SRSPP is shifted by π (or mathematically multiply the waveform equations by -1), the superposed waveform is also shifted by π.

$$H_y^{LRSPP}(x,z) + H_y^{SRSPP}(x,z)e^{i\pi} = 0, \text{ when z > 50nm} \tag{5.4a}$$

$$A^{SRSPP}e^{i\beta_{SRSPP}x} - A^{LRSPP}e^{i(\beta_{LRSPP}x+\pi)} = 0 \tag{5.4b}$$

5.2.2 Longitudinal Analysis

In this section, the longitudinal analysis provides an approach of determining the coupling length, at which the output condition of the coupler can be described by equation (5.3a) and (5.3b). In order to deal with the complex values of the propagation constants, we may utilize the following expressions for both modes.

$$LRSPP: \beta_{LRSPP} = n_{eff_s} \cdot k_0 = \beta_{sr} + i\beta_{si} \tag{5.5a}$$

$$SRSPP: \beta_{SRSPP} = n_{eff_a} \cdot k_0 = \beta_{ar} + i\beta_{ai} \tag{5.5b}$$

Note that the thickness of the metal layer is thick enough (larger than the threshold value derived from chapter 3) that the effective indexes n_{eff_s} and n_{eff_a} in the IMIMI waveguide can be numerically solved by the analytical expression of the MIM waveguide as follow:

$$tanh\left(\frac{k_d \cdot w_d}{2}\right) = -\left(\frac{k_m \varepsilon_d}{k_d \varepsilon_m}\right)^{\pm 1} \tag{3.27}$$

For convenience, +1 represents LRSPP and -1 represents SRSPP.

Based on the discussion of the normalized transversal waveform superposition, the coupling length can be determined by the peak amplitudes of each mode as in the description of equation (5.3b). Regardless of the specific input conditions, the waveform amplitudes at the surfaces between the core dielectric layer and two metal layers, as shown in figure 5-3, are the key parameters to be calculated. When the initial phases of both modes are considered as zero here, the two surface amplitudes can be expressed as follow:

$$A_{II,III}(x) = A^{LRSPP} \cdot e^{i\beta_{LRSPP}x} - A^{SRSPP} \cdot e^{i\beta_{SRSPP}x} \tag{5.6a}$$

$$A_{III,IV}(x) = A^{LRSPP} \cdot e^{i\beta_{LRSPP}x} + A^{SRSPP} \cdot e^{i\beta_{SRSPP}x} \tag{5.6b}$$

$A_{II,III}$ is the amplitude value at the surface of layer II and III regarding to a certain x-axis position, and $A_{III,IV}$ is the amplitude value at the surface of layer III and IV regarding to a certain x-axis position.

By equalizing any of the two values to zero, we are assuming that the output signal of the coupler is mainly guided from the other channel. Thus, the solution of the following equations determine the coupling lengths ($L_{1,2}$) which, if exist, satisfy the coupling condition stated as equation (5.3b).

Let L_1 represents the coupling length of channel 1, and L_2 is for channel 2. With the relative input ratio $A_{ratio} = A^{SRSPP}/A^{LRSPP}$ the lengths can be obtained from the following equations independently.

$$A_{ratio} = e^{[-(\beta_{si}-\beta_{ai})+i(\beta_{sr}-\beta_{ar})]x} \tag{5.7a}$$

$$A_{ratio} = -e^{[-(\beta_{si}-\beta_{ai})+i(\beta_{sr}-\beta_{ar})]x} \tag{5.7b}$$

Recalling the numerical solutions of the effective indexes of the two modes, listed as Table 5-3 below:

IMIMI Waveguide	*Real(n_{eff})*	*Imag(n_{eff})*
LRSPP (*s*-mode)	1.4762	0.0156
SRSPP (*a*-mode)	0.0016	7.5899

Table 5-3: Real and Imag Part of the Effective Indexes for Both Modes

Table 5-3 shows that β_{si} can be regarded as zero when compared with β_{ai} (0.0016<< 7.5899). Also, β_{sr} can be regarded as a rather large value when compared with β_{ar} (1.4762>>0.0156). Plus, when the propagation length is much smaller than the wavelength (~0.1λ), we may have the following approximations.

$$e^{-(\beta_{si}-\beta_{ai})x} \cong e^{\beta_{ai}x}$$

$$e^{i(\beta_{sr}-\beta_{ar})x} \cong 1$$

And the approximated coupling length (L_C) can be simplified as:

$$|A_{ratio}| \cdot e^{-\beta_{ai}L_C} = 1$$

Equivalently, it can be reformed as:

$$L_C = \frac{1}{\beta_{ai}} \ln|A_{ratio}| \tag{5.5}$$

The approximated equation mainly states that the coupling length is proportional to the absolute peak amplitude ratio value $|A_{ratio}|$, and is inversely proportional to the imaginary part of the SRSPP's propagation constant β_{ai}.

Also, it can be concluded from the equation (5.5) that, when $|A_{ratio}|$ is smaller than 1, the coupling length calculated is negative. It shows that when the peak amplitude value of the SRSPP is smaller than that of the LRSPP, the coupling effect between the two modes is not capable of confining the transmission power into a specific channel in such a coupler.

When $|A_{ratio}|$ equals 1, the analytical coupling length is exactly 0. Physically, it describes that if the LRSPP and SRSPP modes are equally normalized, the power is well-confined within one of the channels at the input end of the coupler. In other words, it can be used to represent the plasmonic signal guided into the coupler from one of the channels.

When $|A_{ratio}|$ is larger than 1, we are able to obtain a sub-wavelength coupling length along the signal propagation direction. Compared with the condition above, we may treat the SRSPP signal as a composition of two parts: one is from the signal input guided from one channel, and the rest can be regarded as a control signal to alter the coupling length.

The signs of the variable A_{ratio} determine the output channel, from which the coupled signal would be guided out. It will be discussed in section 5.4.

5.2.3. Numerical Comparisons

From the longitudinal analysis, the calculation of the coupling length between a LRSPP and a SRSPP in the IMIMI waveguide can by carried out from an accurate analytical equation, equation (5.3a), or its approximated version, equation (5.3b). Since both the equations listed above are transcendental equations, which can hardly be compared directly. Therefore, the numerical simulations between the two equations are presented to make a comprehensive comparison.

First of all, after setting the wavelength and the waveguide materials with the same values as the previous section, the thicknesses of both metal and core layers are slightly varied, so that a general idea of the coupling length range in such a structure can be obtained. In order to set up reasonable controls, the amplitude ratio value A_{ratio} between the two modes is selected as 4 here (larger than 1).

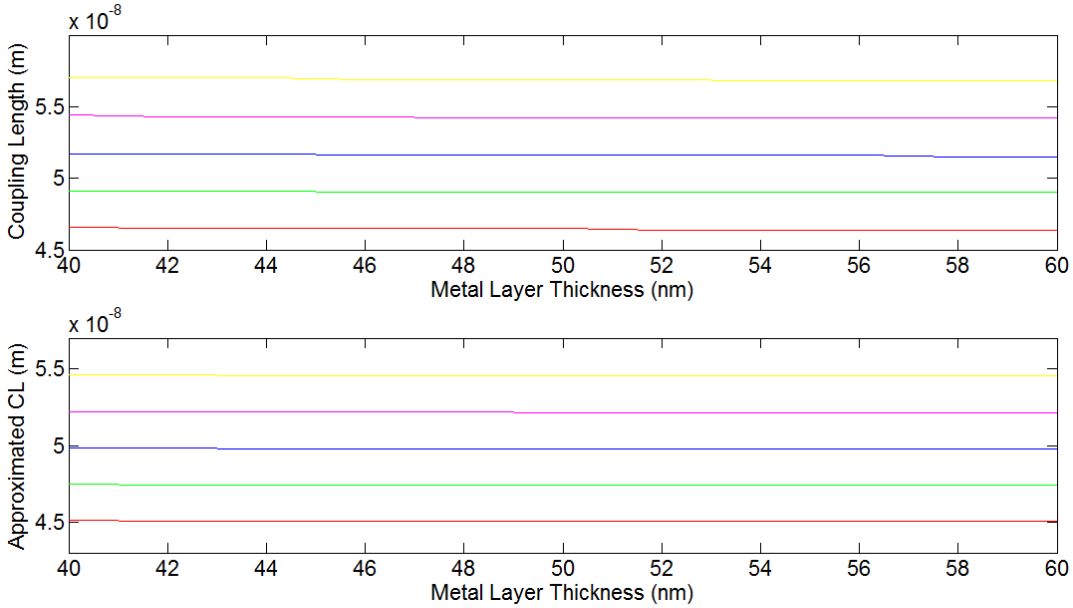


Fig 5-4: The Coupling Length (L_C) of an IMIMI Waveguide under Different Dimensions

As seen from figure 5-4, if the transversal dimension of the IMIMI waveguide is designed within the range discussed in the previous chapters, the coupling lengths of the two modes are rather short (45nm~55nm). And by simplifying the equation (5.3a) into (5.3b), the approximated coupling length results are reduced by 2.26nm on average. Considering the more clearly physical meaning brought into the mathematical expressions, the extra error of the approximation equation (5.5) is tolerable.

It can be observed that the metal layer thickness merely has influence upon the coupling between the two modes. However, when the core layer thickness is enlarged (from 100nm to 120nm), the coupling length is increased by 21%. The linear increment of the coupling length is mainly due to the decrease of the power loss rate of the SRSPP.

Except for the power loss rate along propagation, the input amplitude ratio, A_{ratio}, also plays an important role. Thus, another set of results is presented as below.

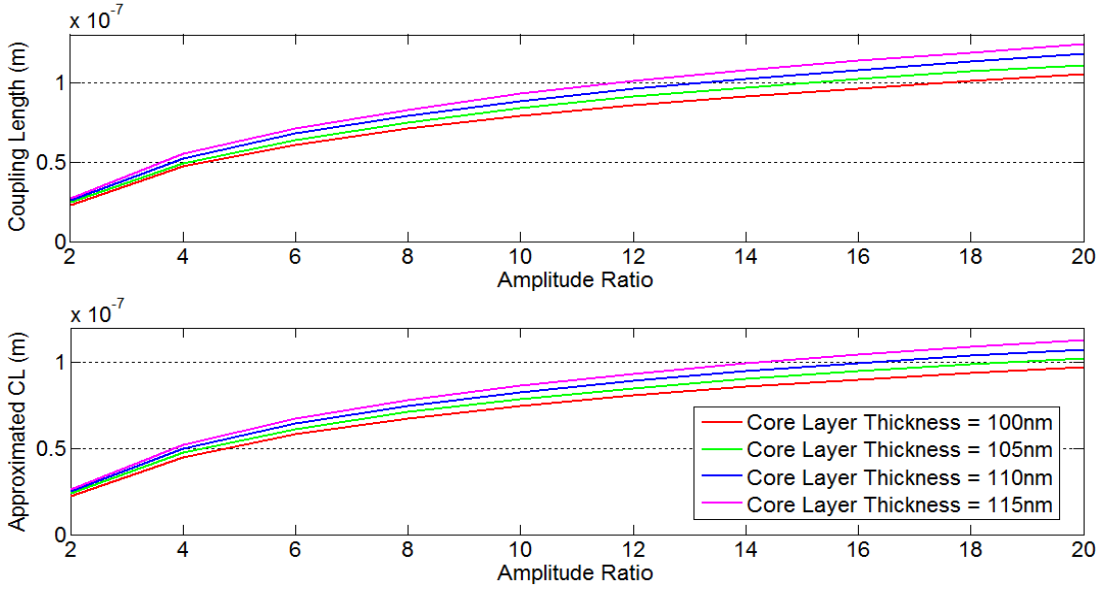


Fig 5-5: The Coupling Length (L_C) vs. Different Amplitude Ratios of the Two Modes

By setting the metal layer thickness as a constant value (50nm), the amplitude ratio A_{ratio} is regarded as the variable here. From figure 5-5, the relationship of the amplitude ratio and the coupling length is proportional when $|A_{ratio}|$ is larger than 1. A straight-forward explanation based on the fundamental properties of these two modes can be presented as follow. As far as the sub-wavelength propagation range (50nm~1550nm) is considered, the transmission power of the LRSPP is relatively well-conserved due to the extreme low loss rate. Therefore, if more lossy SRSPP power is coupled into the waveguide, it would take a longer distance to be reduced into the comparable range that would cause the total-cancellation of time-averaged power in a certain transversal area of the waveguide, such as a specific channel.

Overall, the numerical results of the comparison show that, given the physical conditions described as above, the approximation model, presented by equation (5.5), is able to provide an accurate performance in determining the coupling length of the LRSPP and SRSPP modes with identical wavelength and same initial phase. The validity of equation (5.5) is well testified through the simulation results.

5.3 Exact Numerical Model

5.3.1 Motivation

Despite the fact that the analytical study in section 5.2 is capable of providing a promising coupling length between the LRSPP and SRSPP within the sub-wavelength range, the model is actually built under the assumption that the absolute transversal waveform equations in the metal layers are identical for equally normalized LRSPP and SRSPP modes. Therefore, once the peak amplitude values are cancelled out with each other, the superposed fields can be approximately treated as zero in that channel.

In dealing with the influence caused by such approximation, a straight-forward methodology is presented in this section by numerically simulating the exact superposition of the two modes, and to compare the exact coupling length results with the approximated results of section 5.2. By finding out the differences of results, the analytical equation (5.5) would be adjusted with numerical factors, so that the discrepancy caused by assumptions and approximations can be reduced; meanwhile the simplicity of the expression can be conserved. It would provide a more accurate result for further fabrications.

5.3.2 Model Description

In order to calculate the coupling length of such a coupler accurately, the exact time-averaged power of each channel at the output end should be carefully analyzed. When it vanishes in one channel, the coupling length of the other channel is obtained.

$$P(x) = \frac{1}{2}\oint \boldsymbol{P}_{ave} d\boldsymbol{s} = \frac{1}{2}\oint Re(\boldsymbol{E} \times \boldsymbol{H}^*) d\boldsymbol{s} \tag{4.4}$$

Equation (4.4) can be applied here to calculate the time-averaged power of each channel at any propagation distance. Applying the notations in section 5.2, the LRSPP *H*-field and SRSPP *H*-field are firstly obtained as follow:

$$H_y^{LRSPP}(x,z) = A^{LRSPP}\varphi_{trans}^{LRSPP}(z)e^{i\beta_{LRSPP}x} \tag{5.6a}$$

$$H_y^{SRSPP}(x,z) = A^{SRSPP}\varphi_{trans}^{SRSPP}(z)e^{i\beta_{SRSPP}x} \tag{5.6b}$$

And according to the derived relationships from Maxwell's equations, the *z*-axis component of the *E*-field expressions can be obtained as:

$$E_z^{LRSPP}(x,z) = -\frac{\beta}{\omega\varepsilon_o\varepsilon_i}H_y^{LRSPP}(x,z) \tag{5.6a}$$

$$E_z^{SRSPP}(x,z) = -\frac{\beta}{\omega\varepsilon_o\varepsilon_i}H_y^{SRSPP}(x,z) \tag{5.6b}$$

As shown in section 4.3, these two components of the TM-polarized SPPs determine the time-averaged power along the transmission (*x*-axis) direction. By setting the coordinate of the waveguide as below, the *y*-*z* surface is equally divided as two channels by the line *z*=0.

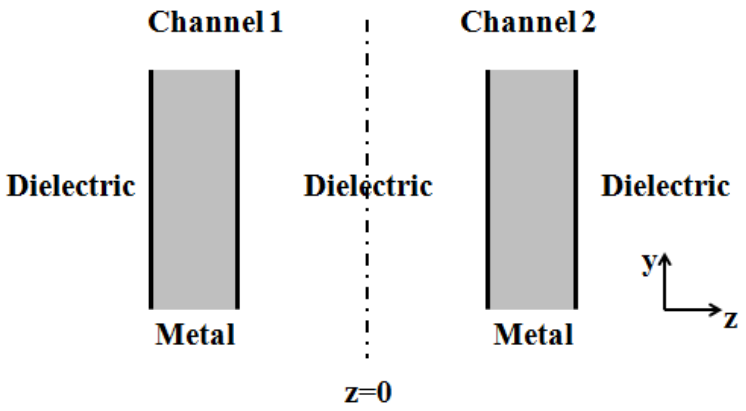


Fig 5-6: y-z Plane Boundries of the Two Channels

Therefore, the time-averaged power in each channel can be expressed as:

$$P_{Channel\ 1} = \frac{1}{2}\int_{z=-\infty}^{z=0}\int Re\left(-E_z(x,z)\cdot {H_y}^*(x,z)\right)dydz \tag{5.7a}$$

$$P_{Channel\ 2} = \frac{1}{2}\int_{z=0}^{z=+\infty}\int Re\left(-E_z(x,z)\cdot {H_y}^*(x,z)\right)dydz \tag{5.7b}$$

Where the *E*-field and the conjugate of *H*-field are both superposed as follow:

$$E_z(x,z) = E_z^{LRSPP}(x,z) + E_z^{SRSPP}(x,z)$$

$$H_y(x,z)^* = [H_y^{LRSPP}(x,z) + H_y^{SRSPP}(x,z)]^*$$

Since the waveform component in the *y*-axis direction is constant, the integration with respect to the variable y can be equivalent to extending the thickness of the waveguide along the *y*-axis. By solving the 2-D waveguide structure with a limited transversal area, it is more meaningful to pay attention to the power density with respect to the different geometric definitions along the *z*-axis. Here, the power density can be defined as below.

$$P_{density}(x) = P_{trans}(x)/t_y \tag{5.8}$$

Where t_y is the waveguide thickness along the *y*-axis direction.

Since the power density function (5.8) is proportional to the time-averaged power, its numerical value will decrease to zero when no power is transmitted within the defined transversal area. The following figure shows the results of calculating the power density of each channel at different propagation length. The coupling length (L_C)

could be determined when the power of one channel is reduced to zero. The coupler structure parameters are as Table 5-1.

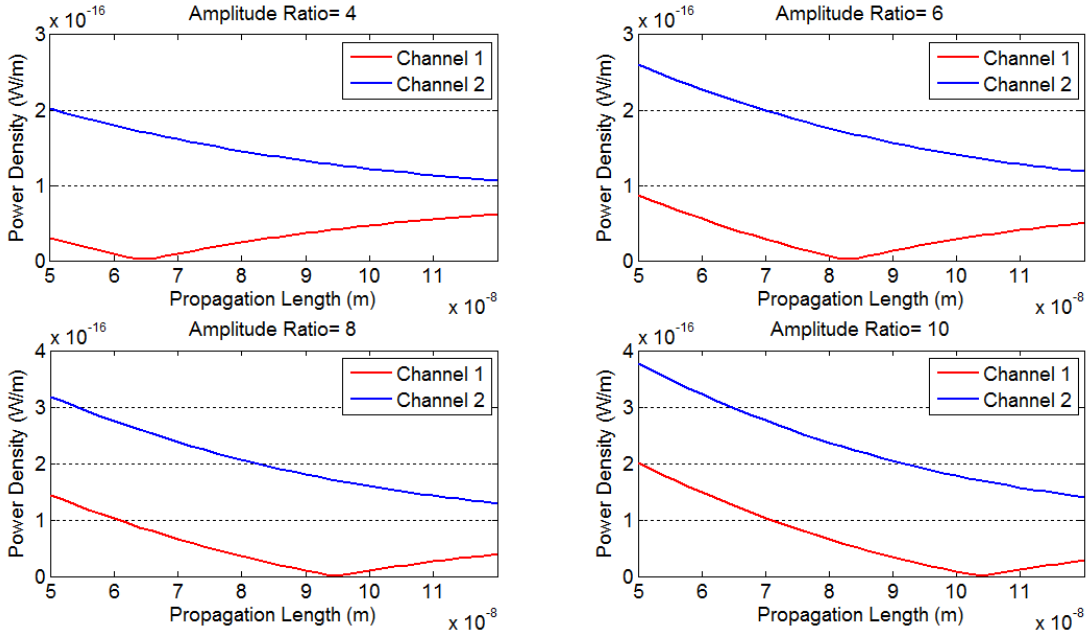


Fig 5-7: Power Density Function of Each Channel with Different Amplitude Ratios

Figure 5-7 consists of four sub-graphs, of which the horizontal axis is the propagation distance and the vertical axis is the power density function of both channels. It can be seen from each of the sub-graphs in figure 5-7 that, after being transmitted for a certain distance, the power density of channel 1 is reduced to zero. This is the exact coupling length determined by this method.

By comparing the four sub-graphs, it can be found that a larger amplitude ratio value would lead to a longer propagation length. This trend agrees with the curve trend in figure 5-5. In all sub-graphs, especially when the amplitude ratio A_{ratio}=4, the power density in both channels start to approach to each other after the coupling length. This phenomenon is caused by the high power loss rate of the SRSPPs. After dissipating all

of its transmission power first, the LRSPP is the only mode in the IMIMI waveguide, and the time-averaged power would be evenly distributed into the two channels due to the symmetry of the mode.

5.3.3 Simulation Results & Discussion

In this section, a numerical simulation about the power transmission of the superposed modes is presented based on the IMIMI waveguide. From the previous study, the metal layer thickness of the array has very limited impact once beyond the threshold values (followed by chapter 3).

Similar to section 5.2.3, the core layer thickness is first considered as the variable when the amplitude ratio A_{ratio} range is the same as that in the figure 5-5.

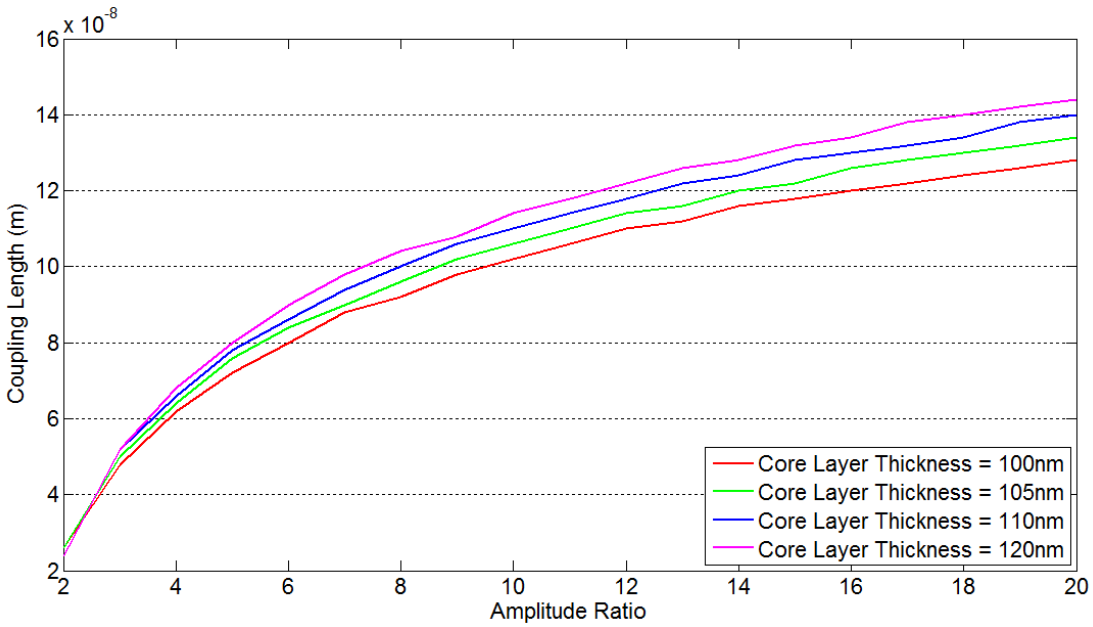


Fig 5-8: The Coupling Length (L_C) of an IMIMI Waveguide under Different Amplitude Ratios of the Two Modes by Exact Numerical Simulation

Figure 5-8 shows the coupling length of such a coupler by using the exact numerical model. Compare with the result of figure 5-5, we may find that the trend of each curve is the same, but the coupling length C_L values determined in figure 5-8 are slightly larger than that of figure 5-5. The difference is mainly caused by the approximation condition described in section 5.2.

In order to determine the precise relation between the results of the two methods, the coupling lengths obtained from figure 5.5 and figure 5.8 are compared directly as follows (dividing the corresponding curve in figure 5.5 by that of figure 5.8).

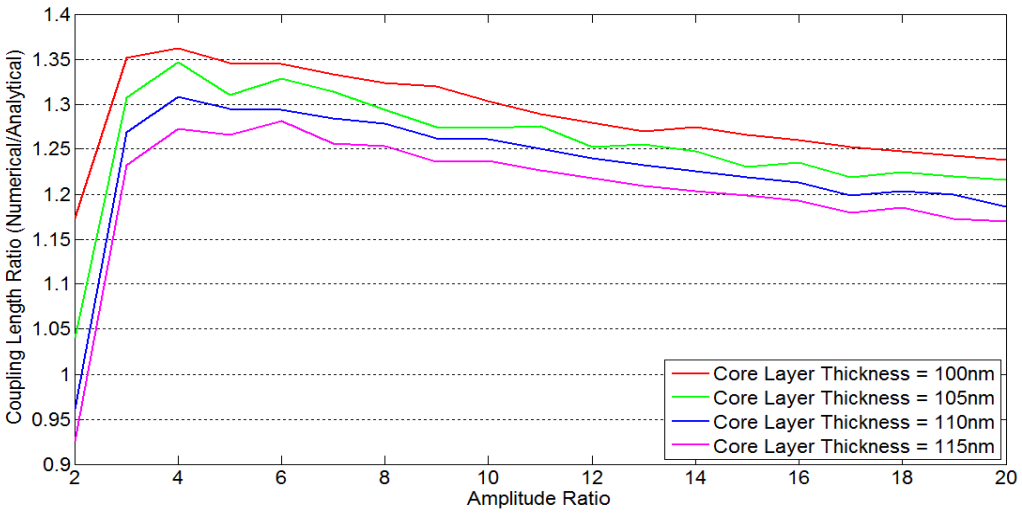


Fig 5-9: The Coupling Length (L_C) Ratio between the Exact Numerical Method and Approximated Analytical Method

When the two methods are applied in the identical coupler to determine the coupling length of different combinations of LRSPP and SRSPP modes, the relations of the two sets of results can be shown as above. When $|A_{ratio}|$ is larger than 4, the results from the exact simulation are larger than those of the analytical ones. As we may see from the four curves, the smaller the core layer thickness is, the larger the

discrepancy is. This is due to the physical fact that a smaller core layer in an IMIMI waveguide would cause a greater transversal coupling within each mode. Thus, even when the peak amplitudes $A_{II,III}$ or $A_{III,IV}$ are reduced to zero in equation (5.6), the exact superposed waveform in this channel cannot be approximated as zero.

Therefore, even with an intuitive physical meaning and a clear mathematical expression, the analytical model developed in section 5.2 would cause an error above 15% when the given coupler and input signal are considered.

However, when the amplitude ratio is larger than 4, the coupling length ratio curves are close to a straight line. This implies a linear relationship can be discovered in between of the two methods, and can be used as a compensation factor to increase the accuracy of the approximation model, equation (5.5).

Given the condition that the metal layer thickness is 50nm, the core layer thickness (w_d) ranges from 100nm to 115nm, and the amplitude ratio (A_{ratio}) ranges from 4 to 20, the average value of the four curves in figure 5-9 can be calculated and is shown in figure 5-10.

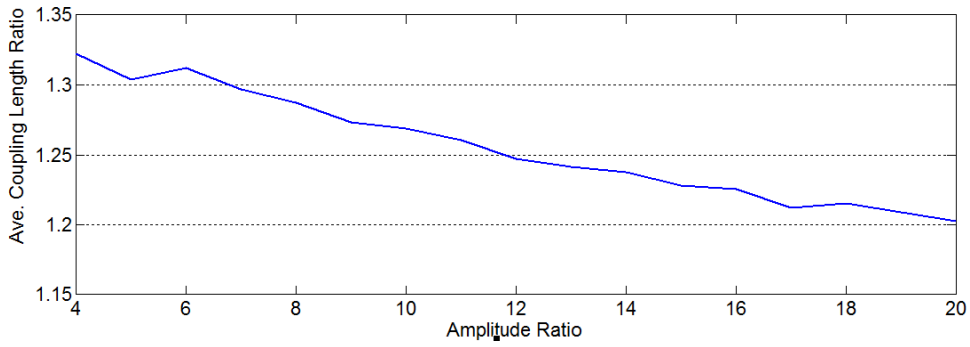


Fig 5-10: The Average Coupling Length (L_C) Ratio between the Exact Numerical Method and Approximated Analytical Method of Figure 5-9

The curve in figure 5-10 can be approximated by the expression:

$$Ave.CL_{ratio} = 1.35 - 0.0075 * A_{ratio} \tag{5.9}$$

Thus, by shifting the straight line slightly according to the average variance of each core layer thickness, the expression of the coupling length can be written as:

$$L_{c_accurate} \cong CL_{ratio} \cdot \frac{1}{\beta_{ai}} ln\, A_{ratio} \tag{5.10}$$

Where $CL_{ratio} = 1.38 - 0.004 \cdot (w_d - 100) - 0.0075 \cdot A_{ratio}$ (5.11)

From section 5.2 and 5.3, we know that equations (5.10) and (5.11) can only be applied with a limited geometry range of such a coupler. However, equation (5.10) would be able to fit a new set of geometry dimensions once equation (5.11) is numerically adjusted. And the methodology of adjusting equation (5.11) is the same as the process introduced above.

5.4 Phase Control of the Coupler

5.4.1 Introduction

In the previous sections, the coupling effect between the LRSPP and SRSPP mode in a coupler design based on the IMIMI waveguide has been studied. From the analytical derivation, equation (5.5), we found that the initial phase of the SRSPP would affect the output signal of the coupler. Consider the extreme condition, if the initial phase of the SRSPP mode is shifted by π, the output signal would be guided from the other channel, equation (5.4b).

However, in real cases, once the input signal is regarded as the superposition of the equally normalized LRSPP and SRSPP from a certain channel of the coupler, that part of the SRSPP mode is always in-phase with the LRSPP mode. The purpose of this section is to discover the possibility of controlling the output channel of the coupler by changing the initial phase of the remaining SRSPP at the input end. Therefore, we may further categorize the plasmonic signal into two parts in this section, namely the information signal and the control signal.

$$H_y(x,z) = H_i(x,z) + H_c(x,z)e^{i\varphi_c} \tag{5.2c}$$

where H_i is the information signal, H_c is the control signal and φ_c is the control phase. In this section, when φ_c=0, the superposition (or sum) of H_i and H_c are the same as the H-field discussed in the previous sections, so that we can simulate the desired control phase values accordingly. When different information (or data) is discussed in the following sections, the amplitude of H_i will be varied. However, as long as the H_c is purely SRSPP, the results of this section will still be valid.

With the coupler structure remained identical to the previous description, the following figure illustrates the definition of the newly-defined signal.

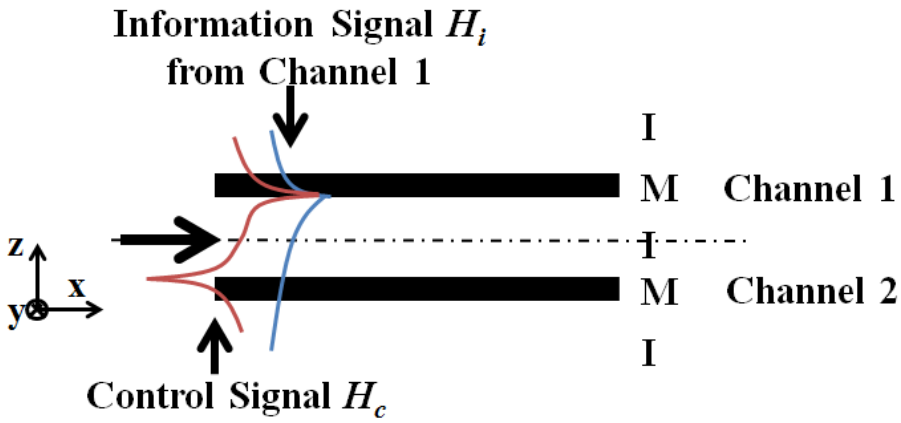


Fig 5-11: Longitudinal Profile of a Duo-Channel SPP Coupler

For consistency, the material of the coupler remains the same as Table 5-1, and the dimensions are defined as $w_d = 100nm, w_m = 50nm$.

Therefore, given an information signal input from one of the channels, by varying the phase of the control signal, the input signal would be guided to different output channels of the coupler. The selection of the output channel is the main function of the phase control, and will be explained in the following sections.

5.4.1.1 Motivation

From the study of the duo-channel SPP coupler, we have known that a short range coupling length can be achieved through a mixed input signal of LRSPP and SRSPP. The critical condition of such a coupling effect is that the peak amplitude of the SRSPP is larger than that of the LRSPP.

However, by simply looking at the random combination of the two modes, the coupling does not have much merit for application. By defining the mixed input as the

superposition of the transmission signal and the control signal, the coupling effect could be interpreted as the active control of the output channel. Such sub-wavelength channel selection would provide huge potential in developing active elements of plasmonic communication.

5.4.1.2 Initial Condition Description

When the information signal is defined to be the input from one of the channels (for example channel 1), the time-averaged power is actually confined within the LHS of the transversal surface of figure 5-2. From section 5.2.1, such input signals could be described as a superposition of the LRSPP and SRSPP as follows (the *H*-field equation is mainly discussed): $A^{LRSPP}\varphi_{trans}^{LRSPP}(z)e^{i\beta_{LRSPP}x}$

$$H_y(x,z) = A^{LRSPP}\varphi_{trans}^{LRSPP}(z)e^{i\beta_{LRSPP}x} + A^{SRSPP'}\varphi_{trans}^{SRSPP}(z)e^{i\beta_{SRSPP}x} \quad (5.12)$$

With the initial condition that:

$$A^{LRSPP} = A^{SRSPP'}\ (x = 0)$$

Compared with equation (5.6a) and (5.6b), it is easy to find that the remaining part of the SRSPP, which is regarded as the control signal, can be expressed as:

$$H_y^{SRSPP}(x,z) = \left(A^{SRSPP} - A^{SRSPP'}\right)(x)\varphi_{trans}^{SRSPP}(z)e^{i\beta_{SRSPP}x} \quad (5.13)$$

By normalizing the waveforms and following the notations, the *H*-fields of the control signal H_c and the information signal H_i can be expressed as:

$$H_i(x,z) = \varphi_{trans}^{LRSPP}(z)e^{i\beta_{LRSPP}x} + \varphi_{trans}^{SRSPP}(z)e^{i\beta_{SRSPP}x} \quad (5.14a)$$

$$H_c(x,z) = (A_{ratio} - 1)\varphi_{trans}^{SRSPP}(z)e^{i\beta_{SRSPP}x} \quad (5.14b)$$

where $A_{ratio} = A^{SRSPP}/A^{LRSPP}$ is the amplitude ratio.

5.4.2 Numerical Analysis of the Phase Control

Intuitively, there are two possible output conditions for the information signal guided into such a coupler. One is to be guided from the same channel as the input, and the other is to be guided from a different one.

In order to study the process of achieving the selection function introduced above, the two possible conditions are studied separately first. Later, by comparing the results of each selection, the feasibility of such phase control will be discussed.

5.4.2.1 Output from the Different Channel

Similar to section 5.2, the input signal (say from channel 1) is output from the other channel (channel 2). Physically, it is equivalent to the phenomenon that all the transmission power is confined in channel 2 at the end of the coupler.

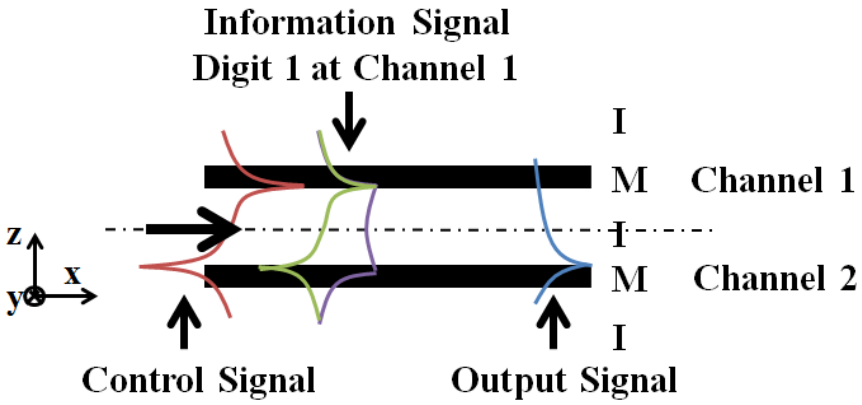


Fig 5-12: Output Signal from the Different Channel of Input

Since the waveguide structure and the output channel selection case is identical to that of section 5.2, the approximation equation (5.10) stating the relationship between the coupling length and the amplitude ratio can be directly applied.

$$L_C \cong [1.38 - 0.004 * (w_d(nm) - 100) - 0.0075 * A_{ratio}] \cdot \frac{1}{\beta_{ai}} ln\, A_{ratio} \qquad (5.10)$$

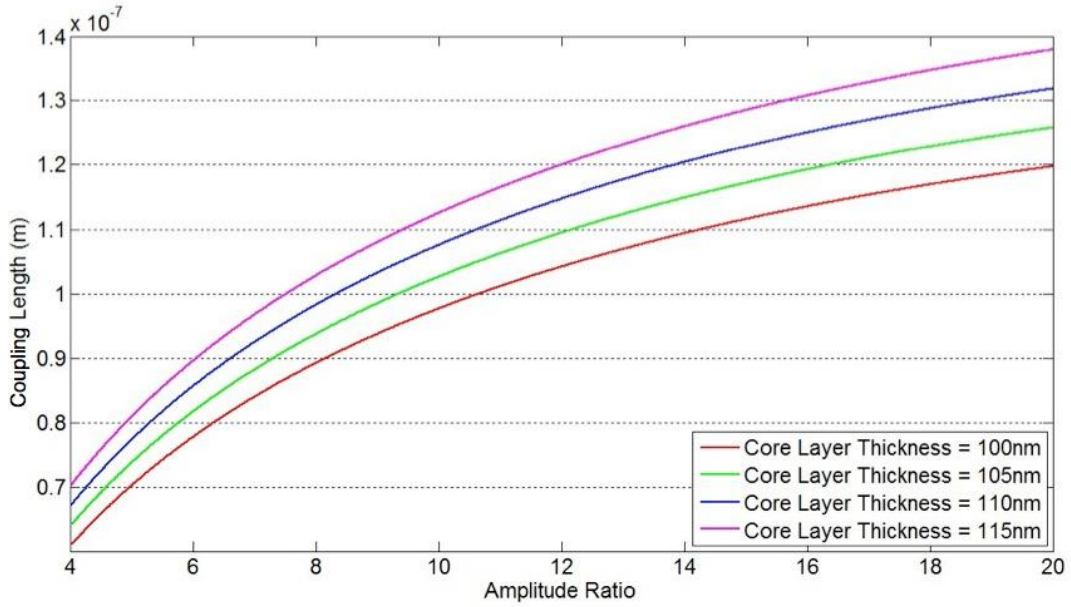


Fig 5-13: The Coupling Length against Different A_{ratio} When the Information Signal is Guided from the Different Channel

By plotting the equation in MATLAB, figure 5-13 provides us with a numerical reference for selecting the A_{ratio} values. Note that the effective amplitude ratio of the control signal is actually ($A_{eff} = A_{ratio} - 1$).

If the coupler length is set as 100nm (in the *x*-axis), the A_{ratio} values can be determined from figure 5-13 as follows:

Core Layer Thickness (w_d)	100nm	105nm	110nm	115nm
Amplitude Ratio (A_{ratio})	10.69	9.37	8.35	7.53

Table 5-4: Numerical Selections of A_{ratio} with Respect to Different w_d Values

If the amplitude of the control signal is not modulated, these parameters can be regarded as the standard values for experimental researches. Also, by following the same structure, the amplitude ratios would also be selected for control signal determination.

5.4.2.2 Output from the Original Channel

According to section 5.2.2, it would be impossible for the information signal to be transferred back to the original channel at the output within the sub-wavelength range, if the input signals remain as given. However, by varying the initial phase of the control signal, the coupling effect of the coupler would be totally different.

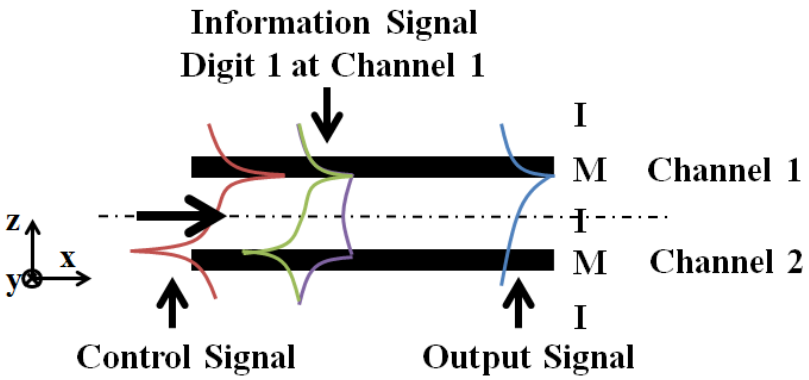


Fig 5-14: Output Signal from the Same Channel of Input

As shown in figure 6-5, with a certain fixed structure of the coupler, and a fixed control signal power to be added at the input end, the phase difference **φ** to be added to the control signal could be determined numerically.

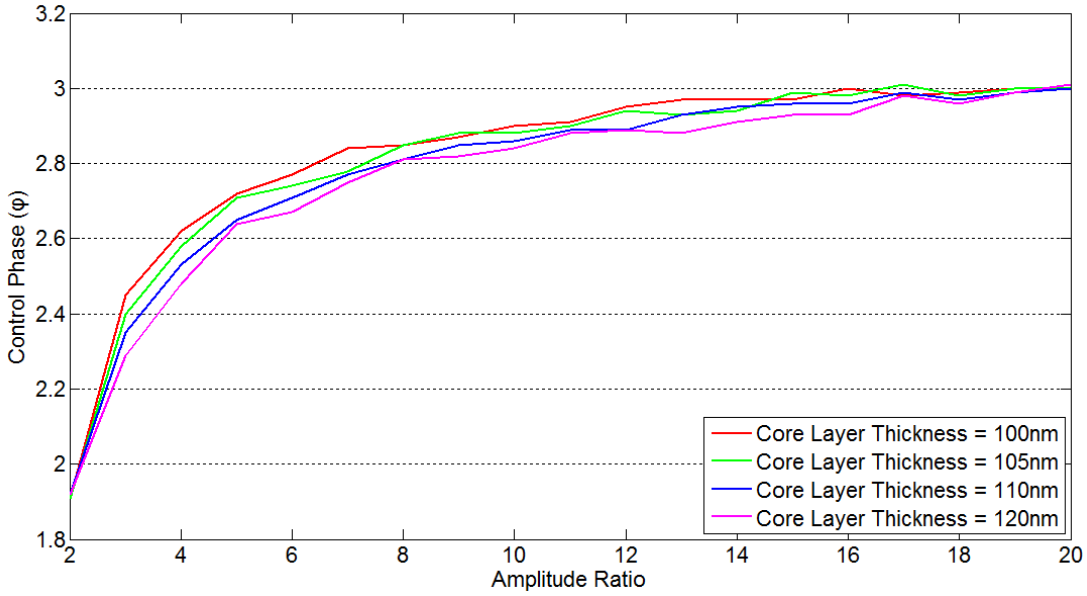


Fig 5-15: The Phase Shift of the Control Signal against Different A_{ratio}

In figure 5-15, each curve stands for the corresponding phase shift of the control signal when the amplitude ratio is varied. If the length of the coupler remains as 100nm, following table 5-4, we may obtain the results:

Core Layer Thickness (w_d)	100nm	105nm	110nm	115nm
Amplitude Ratio (A_{ratio})	10.69	9.37	8.35	7.53
Corresponding Phase ($\boldsymbol{\varphi}$)	2.91	2.88	2.85	2.81

Table 5-5: Numerical Selections of $\boldsymbol{\varphi}$ with Respect to Different w_d Values When the Length of the Coupler is Fixed as 100nm

As shown from the table 5-5, the corresponding control phase is increasing when the core layer thickness is reducing. It is mainly due to the increment of the amplitude ratio value, which indicates a larger control signal power. Ideally, if the control signal power of both cases are infinite ($A_{ratio}\rightarrow\infty$), the corresponding phase shift for the power transfer should be approaching π, at which the phasor is $e^{i\pi}$ =-1.

5.4.2.3 Relative Input-Output Power Ratio

In order to obtain an even output power for both switch selections of the coupler, the relative power ratio between the output signal and the input transmission signal should be calculated and discussed.

For consistency, the coupler structure remains the same as above (100nm in propagation direction). And the expression of the power ratio can be written as:

$$P_{ratio_1,2} = \frac{P_{channel\ 1,2}}{P_{transmission}} \tag{5.15}$$

By applying the phase and the amplitude ratio, A_{ratio}, values from table 5-5, the relative power ratio with different core layer thicknesses can be determined as:

Relative Power Ratio (P_{ratio})	100nm	105nm	110nm	115nm
Output at Original Channel	102.45%	98.57%	97.39%	97.41%
Output at Different Channel	107.63%	105.15%	103.26%	101.71%

Table 5-6: Relative Power Ratio of Both Outputs Regarding to Different w_d Values

From table 5-6, it can be concluded that, even though the SRSPP mode in the input transmission signal is quite lossy, when the control signal required is over five times larger than that of the information signal ($A_{eff} > 5$, or $A_{ratio} > 6$), the final output power of the coupler at each channel is almost the same as the input power ($P_{ratio} \approx 1$). It shows that, no additional amplifier should be added after the coupler in future designs.

Besides, the relative power ratios between two output channels with an identical coupler structure are quite close. The relatively lower output power when the signal is switched to the original channel is caused by the partial cancellation of the control signal and the SRSPP mode in the transmission signal. The discrepancy ranges from 4.3% to 6.5% according to the four specific examples presented.

Since an evenly distributed output power with low loss for each switch selection is the crucial parameter in evaluating the performance of the coupler, the variations of the results with respect to the slightly varied control signal parameters should be carefully studied.

5.4.3 Important Parameters of the Phase Control

In this section, the propagation length of the coupler is set as 100nm. With different transversal layer thickness, the important input control parameters are varied slightly around the numerical standard values from 5.4.2. By comparing the new outputs with the desired ones, the sensitivities of the coupler are evaluated.

5.4.3.1 Relative Phase of the Control Signal

The desired phase values of switching the input power back to the original channel after 100nm can be obtained from table 5-5. By varying each standard with 0.1 rad, the new output power ratio can be plotted as below.

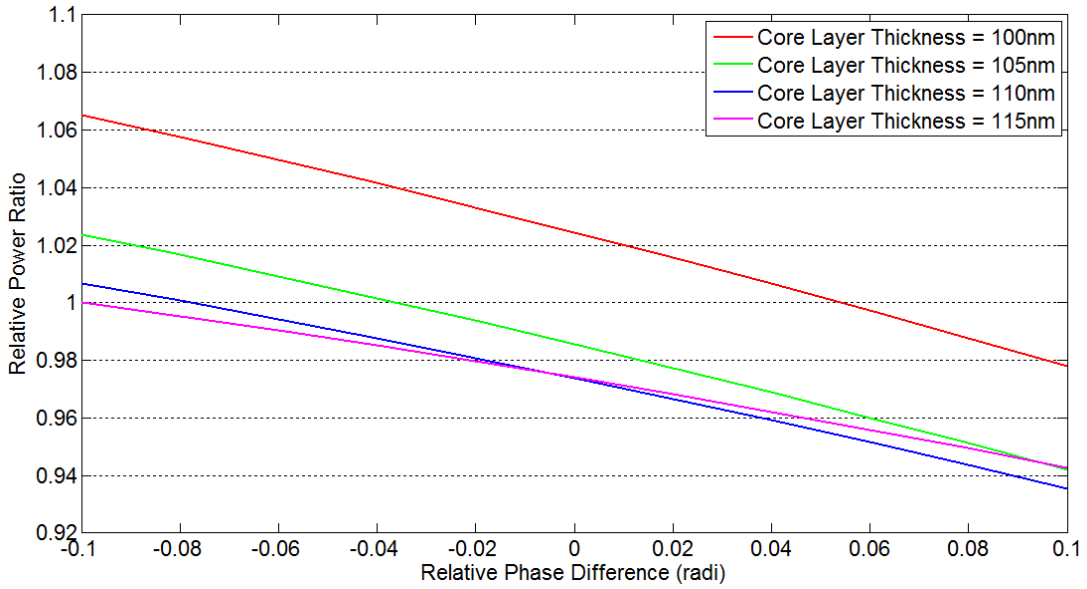


Fig 5-16: The Relative Power Ratio of Two Output Conditions Against Varied Control Phase Values

When the power is to be switched back to a different channel, no phasor is required. Thus, only the case when the signal is switched back is considered. By replacing the accurate phase with an error of at most 0.1 rad, the output power is

linearly varied by 2.8%~4%. The smaller the core layer is, the more sensitive the coupler is with respect to the control phase.

5.4.3.2 Relative Amplitude of the Control Signal

The desired A_{ratio} values of both situations can be found from table 5-4. By varying each A_{ratio} with 0.5, the new output power ratio can be plotted as below.

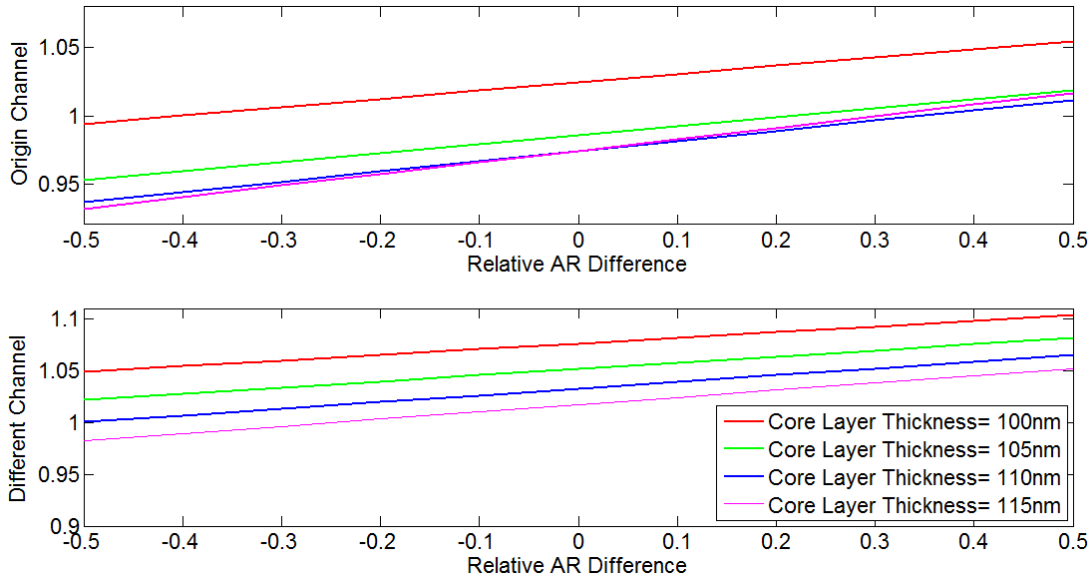


Fig 5-17: The Relative Power Ratio of Two Output Conditions Against Varied Amplitude Ratio Values

In this section, the amplitude ratio of the control signal would affect both situations of the coupler. By replacing the accurate A_{ratio} value with an error of at most 0.5 the output power is linearly varied by 2.5% in both two sub-graphs. Based on the design, the two sets of variances indicate the fact that the coupler is more sensitive to the phase of the control signal, rather than the amplitude ratio value. Therefore, a more sensitive phasor would be the next important step in realizing the design proposed in this thesis.

5.5 Data Transmission

5.5.1 Objective

In the previous sections, the sub-wavelength coupler applied in guiding a plasmonic signal has been carefully proposed and examined. However, in order to apply such a device into real integrated circuit designs, the capability of guiding data sequences with low error rate is the key issue that requires further consideration. In the following sections, different outcomes at the receiver's end will be simulated. In order to achieve a feasible model for data transmission, the differences between the received powers of each data should be significant.

In this section, the most fundamental bit transmission model, namely the on-off model, is applied onto the proposed device. In such a model, the digit '1' is transmitted when the information signal, as described in equation (5.14), is fully 'on'; while the digit '0' is transmitted when the information signal equals zero. The actual information signal is input from one of the channels. Based on the coupling effect on the input surface (the cross-sectional surface), two modes (*s* and *a* modes) with same peak amplitude values (as discussed in section 5.2) will be excited and propagated along the device. However, since the *a*-mode suffers a greater loss, if no additional a-mode power is injected, the signal will be finally evenly distributed in two channels (only *s*-mode survives).

Thus, we need a control signal, which is purely the *a*-mode, to compensate the power loss and to control the output channel. The physical theory is based on the interference phenomena between superposed modes. And the actual realization is

quite similar to a coupler (or an active coupler), in which the information signal is guided through the device with no significant loss, and is output from an arbitrary channel by changing the initial phase of the control signal. By plotting equation (5.14), we may have the following diagrams at the input end of the coupler.

$$H_{i_on}(x,z) = \varphi_{trans}^{LRSPP}(z)e^{i\beta_{LRSPP}x} + \varphi_{trans}^{SRSPP}(z)e^{i\beta_{SRSPP}x}$$

$$H_{i_off}(x,z) = 0 \tag{5.14a}$$

$$H_c(x,z) = (A_{ratio} - 1)\varphi_{trans}^{SRSPP}(z)e^{i\beta_{SRSPP}x} \tag{5.14b}$$

The following figures display the superposition of data and control signals for both digit '1' and digit '0' cases, in which the waveforms of each equations are roughly sketched for the ease of understanding.

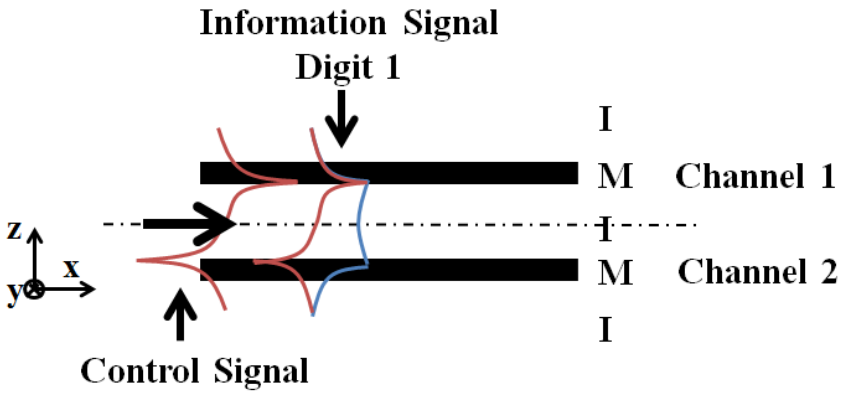


Figure 5-18 a: Sketches for Digit 1's Transversal Waveforms at the Input

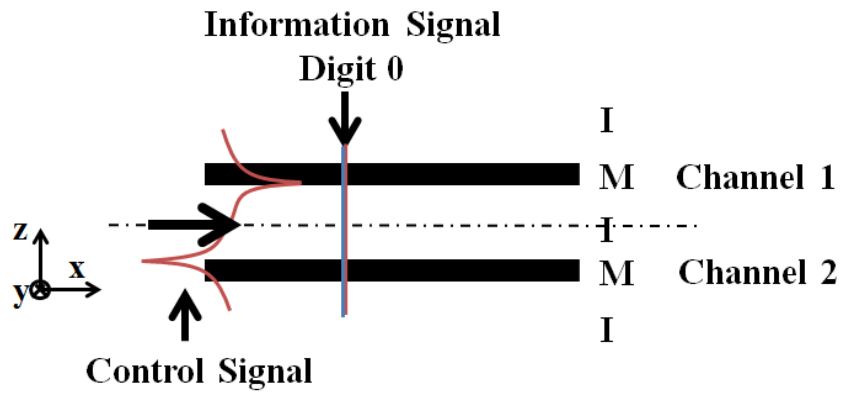


Figure 5-18 b: Sketches for Digit 0's Transversal Waveforms at the Input

After substituting different input situations (digit '1' or '0') into the simulation, we may have different output waveforms at both channels. By comparing the output power ratio, or the On/Off power ratio ('on' refers to transmitting digit '1' and 'off' refers to digit '0'), with different amplitude ratio (A_R) values, a desired A_R with higher power difference at the output end can be determined. Remember that the amplitude of the control signal is adjusted (via A_R) to maintain the amplitude of the information signal at the output of channel 1.

5.5.2 Output Modal Description

Previously, in figure 5-3, we have displayed the output profile when one of the channels is receiving the signal with both H_i and H_c being transmitted. However, when a digit '0' is being transmitted, the absence of the information signal will reduce the LRSPP signal to zero, and will decrease the *a*-mode amplitude by $(A_{ratio}\text{-}1)/A_{ratio}$ (the control signal is remained on for the ease of application). The residue control signal may cause disturbance in data transmission. The following figures show the output of both transmission cases (digit '1' and '0'), when A_{ratio}= 5.

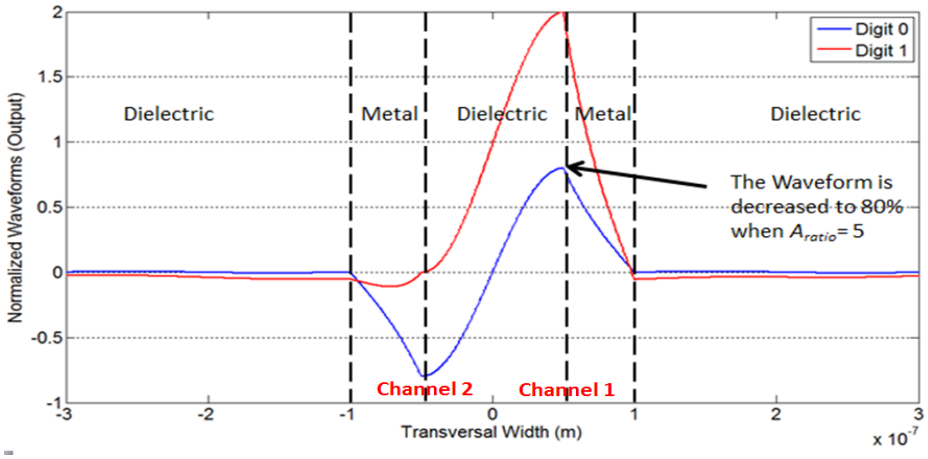


Fig 5-19a: Numerical Plotting of the Real Part of the Digit '0' H-Field

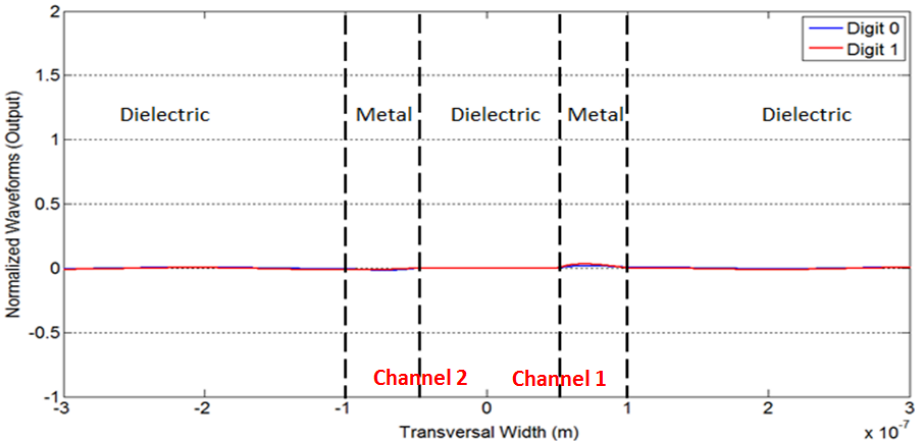


Fig 5-19b: Numerical Plotting of the Imaginary Part of the Digit '0' H-Field

It can be observed from the above figures that it will not achieve the real "power-off" situation (zero output power at both channels) when a digit '0' is being transmitted. Therefore, the energy difference at the output between the different transmission states (i.e. data '1' or '0') must be carefully calculated. The aim of the following section is to demonstrate that the proposed device, when transmitting data and control signals, can be used to propagate distinguishable logic states at the output of channel 1.

5.5.3 Important Quantities

The discussion of this section is based on the single-input-single-output (SISO) transmission mode. In the SISO mode, the information signal will be input from one of the channels, and the output power of both channels will be simulated. Between the two output channels, the one used for information determination is named the 'target channel', while the other one is named the 'idle channel'.

5.5.3.1 Output On/Off Power Ratio

The On/Off power ratio is mainly used to determine the output power difference at each transmission states, namely transmitting digit '1' and digit '0'. A larger power ratio value will lead to a larger bit energy difference. Thus, a better transmission performance can be achieved with lower bit error rate (BER) [62].

Mathematically, the expression of the On/Off power ratio can be expressed as follows when the information is output from channel 2 (the positive half of *z*-axis).

$$R_t = \frac{\int_{z=0}^{z=+\infty} \int Re\left(-H_{y_on}(x,z) \cdot {H_{y_on}}^*(x,z)\right) dydz}{\int_{z=0}^{z=+\infty} \int Re\left(-H_{y_off}(x,z) \cdot {H_{y_off}}^*(x,z)\right) dydz} \tag{5.16a}$$

$$R_i = \frac{\int_{z=-\infty}^{z=0} \int Re\left(-H_{y_on}(x,z) \cdot {H_{y_on}}^*(x,z)\right) dydz}{\int_{z=-\infty}^{z=0} \int Re\left(-H_{y_off}(x,z) \cdot {H_{y_off}}^*(x,z)\right) dydz} \tag{5.16b}$$

where R_t and R_i represent the target channel and the idle channel, respectively.

$$H_{y_on}(x,z) = H_y^{LRSPP}(x,z) + H_y^{SRSPP}(x,z) \tag{5.17a}$$

$$H_{y_on}(x,z) = \frac{A_{ratio} - 1}{A_{ratio}} \cdot H_y^{SRSPP}(x,z) \tag{5.17b}$$

By substituting equation (5.17) into (5.16), we may obtain the relation between R_t, R_i and A_{ratio} as follow.

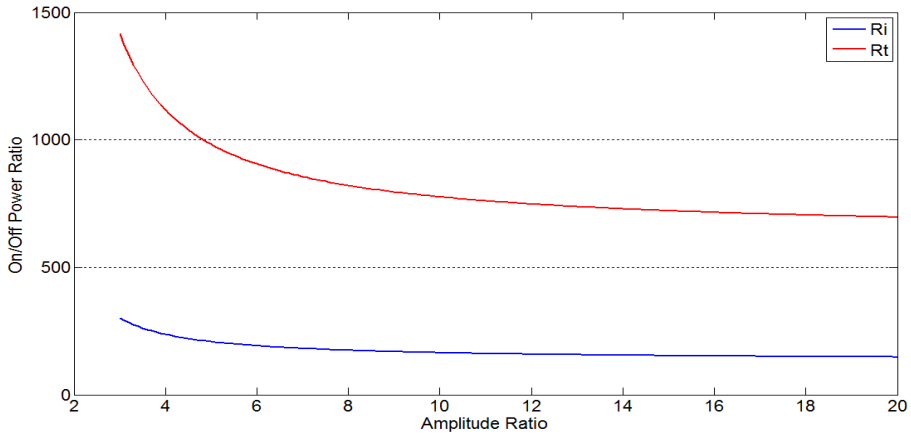


Fig 5-20: On/Off Power Ratio with regarding to A_{ratio} values

The two curves in the figure above show that the output power ratio between the 'on' mode (digit 1) and the 'off' mode (digit 0) is significant when the A_{ratio} values are selected within the range 2 to 200. Therefore, the threshold values can be easily set between the two output power values, and distinguishing between the two data states appears to be feasible.

5.5.3.2 Input/ Output Ratio

The input/ output ratio, *Q*, is the quantity that measures the ratio between the input power difference and the output power difference. An ideal on/off transmission will lead to the target channel ratio Q_t=1, and the idle channel ratio Q_i=1.

$$Q_t = \frac{P_{target_on} - P_{target_off}}{P_{input_on} - P_{input_off}} \tag{5.18a}$$

$$Q_i = \frac{P_{idle_on} - P_{idle_off}}{P_{input_on} - P_{input_off}} \tag{5.18a}$$

where Q_t and Q_i are the quantities that measure the ratio between the input power difference and the output power difference; P_{input_on} is the information signal power of a digit '1', and P_{input_off} is the information signal power of a digit '0' (equals zero in this case); $P_{target_on/off}$ is the output power of the target channel, and $P_{idle\ _on/off}$ is the output power of the idle channel. Similarly, we may find the relations between Q_t, Q_i and A_{ratio} as follow.

The figure below shows that both Q_i and Q_t are close to the ideal value 1. When the A_{ratio} value is increasing, the *Q* values are slightly decreasing. Generally, the values remain above 0.99 within the range of previous discussion (from 2 to 20). This is mainly because the power supplied from the control signal.

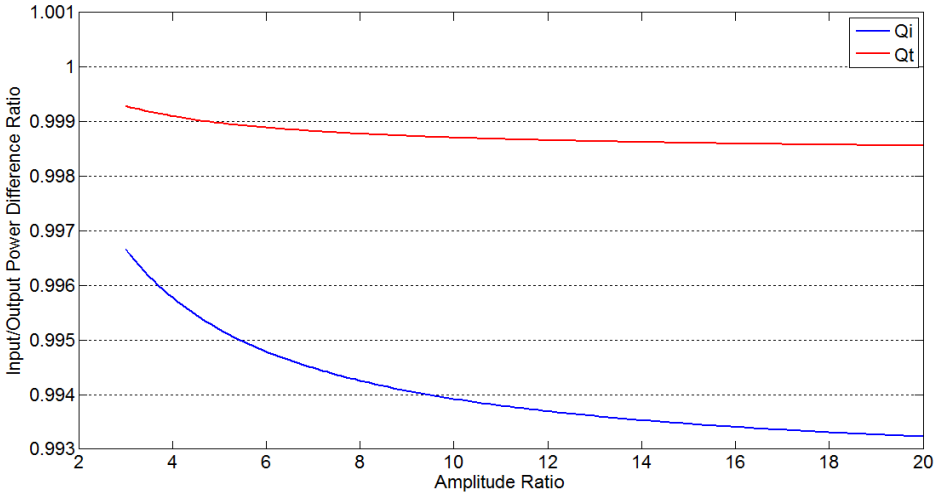


Fig 5-21: Input/ Output Power Difference Ratio with regarding to A_{ratio} values

5.5.3.3 Discussion

As we may see from the above calculation, the energy level between the digit 1 and digit 0 are large enough for data transmission when a SISO mode is applied in such a device. The high *Q* values from figure 5-20 reveal that the power ratio is well maintained within the sub-wavelength propagation distance.

However, the current proposal is based on an ideal input condition, which includes a pure SRSPP control signal with precise amplitude values. If the proposal is to be applied into experimental or industrial applications, this will become a quite important condition. And also, more complicated data transmission modes, such as the double-input-single-output (DISO) mode, should also be studied in the future. Nonetheless, the proposed device appears to have some merits as a simple router and practicalities associated with its implementation might be worth considering.

5.6 Conclusion

By looking into the LRSPP and SRSPP modes of the IMIMI waveguide, the coupling effect of these two modes were studied in detail in this chapter. The principle of normal-mode analysis was applied throughout the chapter.

By showing the similarity of the transversal decay rates of both LRSPP and SRSPP in the metal layers of the coupler, the mathematical description of the two modes' superposition in such an element has been further simplified. The approximated analytical equation calculating the coupling length was determined. By using the numerical solutions of the two modes' propagation constants from chapter 3, the equation was further simplified as equation (5.5). Both of the analytical expressions of the coupling length were intuitive to be applied and indicated a super short coupling length within the sub-wavelength range.

In section 5.3, the exact numerical model of such a coupling effect was proposed by calculating the time-averaged transmission power (along the transversal surface of the coupler) of the superposed modes as a function of the propagation distance. By comparing the difference of the results with the analytical solution of section 5.2, a revised expression of the analytical equation was obtained as equation (5.10) when the coupler's geometry parameter and the plasmonic signal remained the same as the conditions discussed in this chapter.

In section 5.4, the function of selecting the output channel of the coupler by adding phase control into part of the input signal was proposed. By applying the revised coupling length equation (5.10) into the coupling case introduced in section 5.3,

the relationship of the amplitude ratio, A_{ratio}, and the coupling length was first obtained. After setting the A_{ratio} and coupling length as fixed values, the corresponding phase shift of the control signal was calculated in section 5.4.2.2. Later in the example case discussed in this thesis, when the coupling length was set as 100nm and the transversal geometry of the coupler was set as Table 5-1, the phase shifting value was calculated to be 2.91. From the results of section 5.4.2.3, the output powers of the each case were 102.45% and 107.63% of the initial input signal power, respectively. It indicated that no additional power amplifier would be needed if the coupler was applied in a plasmonic communication system. Furthermore, by scrutinizing two of the crucial parameters, the phase and the amplitude of the control signal, which would directly determine the feasibility of the design, the potential application range of such a coupler was presented.

In section 5.5, the completed data transmission of the single-in-single-out (SISO) model is simulated by launching both two digit states (digit '1' and '0') into the proposed device. In order to achieve a promising transmission performance, two crucial quantities were calculated and plotted. The one that measures the output powers ratios between different digital states, namely the On/Off power ratio, was found large enough to be distinguished by the receiver. This could be directly linked with a low bit error rate in future applications. The other one that measures the ratio between the input power difference and the output power difference was found close to 1 in both channels. This proved that the information power was well conserved by compensating the control signal as the power supply.

The analytical and numerical work of this chapter was based on the wave theory study proposed in chapter 3 and chapter 4. The sub-wavelength coupling length of the IMIMI waveguide has shown the potential of developing the current plasmonic devices into a more compact dimension.

Chapter 6 Conclusion

6.1 Summary of Findings

During the two years' study and research, a systematic study of the dielectric/metallic (D/M) waveguide array based on the surface plasmon polariton theory has been successfully accomplished, and the major findings have been summarized in this thesis.

In chapter 3, the general D/M waveguide array was studied by using the normal mode analysis. An iterative analytical solution of a general D/M array structure was proposed for the first time, which could be regarded as the analytical solutions for the complex waveguide array that could only be solved numerically now. Then, by further defining the structure as an identical D/M waveguide array, the analytical expressions are further simplified. In comparison with the existing analytical solutions of several simple arrays, such as the IMIMI waveguide and the MIM waveguide, the validity of the new approach was further enhanced. Meanwhile, the analytical equations were applied in MATLAB simulations. And the numerical performances of such approach, mainly the effective indexes of different plasmonic modes, are solved. The impact of the metal layer was further quantized with a threshold thickness value.

Based on the analytical approach, the expressions, together with the numerical simulation results, of the energy confinement property and the propagation loss were further derived in chapter 4. The analytical expression of the time-averaged power ratio in adjacent layers of a general D/M waveguide array was obtained on the basis of the iterative analytical solution directly. Considering the widely-applied IMIMI

waveguide case, it led to the accurate determination of the condition that at least 99.9% of the transmission power would be confined within the core layers. Similarly, the same waveguide was selected to intuitively display the results of the propagation loss of different guided modes. The attenuation rate of the anti-symmetric mode (*a*-mode) was proved to be much swifter than that of the symmetric mode (*s*-mode).

By using the special physical characteristics displayed in the wave theory study of the waveguide arrays and the different modes to be carried, the coupling between the LRSPP (*s*-mode) mode and the SRSPP (*a*-mode) mode was studied in a new way. In comparison with the coupling length results from the exact numerical model, the analytical expression was further modified with an additional numerical parameter when a specific waveguide dimension range was considered. Both of the approaches indicated a sub-wavelength coupling length between the two modes.

Furthermore, by splitting the input signal into the information signal and the control signal, the phase control method of selecting the output channel was proposed. By double-checking the output power of each condition, the proposed coupling effect would be able to provide a coupling length within the sub-wavelength range with no significant power loss. In order to enhance the application potential of such a device, the data transmission was finally tested by using the On/Off model. After confirming the significant power difference of the two digit states, as well as the power ratio information signal between the output and input, the performance of such a device under the traditional communication conditions was presented. The listed results showed potential for developing such a device into more complicated usage.

In summary, this thesis first introduced an innovative analytical approach of solving the D/M waveguide array for surface plasmonic communication. By applying numerical simulation into the results, it showed a number of new findings in the key parameters, which also further led to the discovery of the special coupling effect, as well as the sub-wavelength coupling length.

6.2 Future Work

In the future, there are two different research topics that can be developed from the work introduced in this thesis. Both of them are mainly about transferring the analytical and numerical results into real applications. The difference of them is that, one is more focused on the systematic communication, while the other is mainly the plamsonic device fabrication.

The systematic communication study could be closely related to the theoretical study of the general D/M waveguide array. The general D/M waveguide array structure can be further applied as a multiple channel connection between different integrated circuits. A systematic data transmission model can be developed on the basis of its physical nature that has been looked into in detail. Especially when the plasmonic devices are to be matched with the electronic integrated circuits, the dimensions of the circuit elements would be further reduced. A more complicated waveguide array, rather than the IMIMI waveguide, would be designed based on my findings in this thesis.

The implementation of the plasmonic device designs, for example a sub-wavelength coupler, would be realized through experimental approaches. The theoretical proposal and numerical tests shown in chapter 5 were merely the initial stage work. The real coupler should be first designed and fabricated in the laboratory. The major difficulties of achieving the desired performance would be the excitation of the pure SRSPP signal at the same wavelength with the input transmission signal, the control of its phase, as well as the determination of the control signal's power.

REFERENCES

[1] Roney Thomas, Zoran Ikonic, and R.W. Kelsall (2012), “Silicon based plasmonic coupler”, Opt. Express, Vol. 20, No. 19, pp. 21520-21531

[2] J. C. Weeber, A. Dereux, C. Girard, J. R. Krenn, and J. P. Goudonnet (1999), “Plasmon polaritons of metallic nanowires for controlling submicron propagation of light”, Phys. Rev. B 60, 9061-9068

[3] E. P. Fitrakis, C. Kachris, A. Scandurra, A. Melikyan, M. Sommer, M. Kohl, J. Leuthold, V. Dolores-Calzadilla, M. K. Smit, D. Van Thourhout, Z. Hens, I. Suarez, J. Martinez-Pastor, I. Tomkos (2012), “Plasmonic technology innovation: The chip-to-chip interconnect”, NAVOLCHI

[4] H. J. Lezec, A. Degiron, E. Devaux, R. A. Linke, L. Martin-Moreno, F. J. Garcia-Vidal, and T. W. Ebbesen (2002), “Beaming light from a sub-wavelength aperture”, Science 297, 820

[5] Georgios Veronis and Shanhui Fan (2008), “Crosstalk between three-dimensional plasmonic slot waveguides”, Opt. Express, Vol. 16, No. 3, 2129-2140

[6] W. Steinhogl, G. Schindler, G. Steinlesberger, and M. Engelhardt (2000), “Size-dependent resistivity of metallic wires in the mesoscopic range”, Phys. Rev. b 66, 075414

[7] Jing Chen, Gennady A. Smolyakov, Steven R. J. Brueck and Kevin J. Malloy (2008), “Surface plasmon modes of finite, planar, metal-insulator-metal plasmonic waveguides”, Opt. Express, Vol. 16, No. 19, pp. 14902-14909

[8] R. Charbonneau, N. Lahoud, G. Mattiussi, and P. Berini (2005), “Demonstration of integrated optics elements based on long-ranging surface plasmon polaritons”, Opt. Express, vol. 13, no. 3, pp. 977-984

[9] T. Nikolajsen, K. Leosson, and S. I. Bozhevolnyi (2004), “Surface plasmon polariton based modulators and switches operating at telecom wavelengths”, Appl. Phys. Lett., vol. 85, no. 24, pp. 5833-5836

[10] A. Boltasseva, S. I. Bozhevolnyi, T. Sondergaard, T. Nicolajsen, and K. Leosson (2005), “Compact Z-add-drop wavelength filters for long-range surface plasmon polaritons”, Opt. Express, vol. 13, no. 11, pp. 4237-4243

[11] J. A. Conway, S. Sahni, and T. Szkopek (2007), “Plasmonic interconnects versus conventional interconnects: a comparison of latency, crosstalk and energy costs”, Opt. Express, vol. 15, no. 7

[12] Y. -F. Li and J. W. Y. Lit (1987), “General formulas for the guiding properties of a multilayer slab waveguide”, J. Opt. Soc. Amer. A, vol. 4, pp. 671-677

[13] H. A. Haus and L. Molter-Orr (1983), “Coupled multiple waveguide systems”, IEEE J. Quantum Electron., vol. QE-19, pp. 840-844

[14] E. Kapon, J. Katz and A. Yariv (1984), “Supermode analysis of phase-locked arrays of semiconductor”, Opt. Lett., vol. 10, pp. 125-127

[15] T. W. Ebbesen, H. J. Lezec, H. F. Ghaemi, T. Thio, P. A. Wolff (1998), “Extraordinary optical transmission through sub-wavelength hole arrays”, Nature (London) 667, 391

[16] Stefan A. Maier (2006), “Plasmonics: Fundamentals and Applications, Springer”, 25-29

[17] F. J. Garcia-Vidal, Esteban Moreno, J. A. Porto, and L. Martin-Moreno (2005), “Transmission of light through a single rectangular hole”, Phys. Rev. Lett., 95, 103901

[18] Evgeny Popov, Michel Neviere, Philippe Boyer, and Nicolas, Bonod (2005), “Light transmission through a sub-wavelength hole”, Opt. Commun. 255, 338

[19] Francisco Garcia de Abajo (2002), “Light transmission through a single cylindrical hole in a metallic film”, Opt Express 10, 1475

[20] A. Kumar and T. Srivastava (2008), “Modeling of a nanoscale rectangular hole in a real metal”, OPTICS LETTERS, Vol. 33, No.4, pp1-3

[21] JENS Buus (1982), “The Effective Index Method and Its Application to Semiconductor Lasers”, IEEE JOURNAL OF QUANTUM ELECTRONICS, VOL. QE-18, NO. 7

[22] R. Gordon, and A. G. Brolo (2005), “Increased cut-off wavelength for a sub-wavelength hole in a real metal”, Opt. Express 13, 1933

[23] S. Collin, F. Pardo and Jean-Luc Pelouard (2007), “Waveguide in nanoscale metallic apertures”, Opt. Express, vol. 15, no. 7

[24] X. Fan, G. Wang, J. C. W. Lee, and C. T. Chan (2006), “All-Angle Broadband Negative Refraction of Metal Waveguide Arrays in the Visible Range: Theoretical Analysis and Numerical Demonstration”, Phys. Rev. Lett., 97, 073901

[25] L. Martin-Moreno, F. J. Garcia-Vidal, H. J. Lezec, K. M. Pellerin, T. Thio, J. B. Pendry and T. W. Ebbesen (2001), “Theory of extraordinary optical transmission through sub-wavelength hole arrays”, Phys. Rev. Lett. 86, 1114

[26] Kane Yee (1966), "Numerical solution of initial boundary value problems involving Maxwell's equations in isotropic media", IEEE Transactions on Antennas and Propagation14 (3): 302–307

[27] A. Christ and H. L. Hartnagel (1987), "Three-Dimensional Finite-Difference Method for the Analysis of Microwave-Device Embedding", IEEE Transactions on Microwave Theory and Techniques 35 (8): 688–696

[28] M. A. Swillam and Amr S. Helmy (2010), “Analysis and application of 3D rectangular metallic waveguide”, Opt Express, vol. 18, no. 19

[29] Electromagnetics Module User's Guide (Comsol, 2007), Sweden. http://www.comsol.com.

[30] R. Zia, M. D. Selker, and M. L. Brongersma (2005), "Leaky and bound modes of surface plasmon waveguide", Phys. Rev. B 71, 165431

[31] P. Lusse, P. Stuwe, J. Schule, and H. G. Unger (1994), "Analysis of vectorial mode fields in optical waveguides by a new finite difference method", J. Lightwave Technol. 12, 487

[32] T. Yang and K. B. Crozier (2008), "Surface plasmon coupling in periodic metallic nanoparticle structures: a semi-analytical model", Opt Express, vol. 16, no. 17

[33] M. L. Brongersma, J. W. Hartman, and H. A. Atwater (2000), "Electromagnetic energy transfer and switching in nanoparticle chain arrays below the diffraction limit", Phys. Rev. b 62, R16356-16359

[34] W. H. Weber and G. W. Ford (2004), "Propagation of optical excitations by dipolar interactions in metal nanoparticle chains", Phys. Rev. B 70, 125429

[35] A. F. Koenderink, and A. Polman (2006), "Complex response and polariton-like dispersion splitting in periodic metal nanoparticle chain", Phys. Rev. b 74, 033402

[36] T. Yang and K. B. Crozier (2008), "Dispersion and extinction of surface plasmons in gold nanoparticle chains: influence of the air/glass interface", Opt. Express 16, 8570-8580

[37] Z. Ruan and M. Qiu (2006), "Enhanced transmission through periodic arrays of sub-wavelength holes: the role of localized waveguide resonanaces", Phys. Rev. Lett 96, 233901

[38] V. G. Veselago (1968), "The electrodynamics of substances with simultaneously negative values of ε and μ", Sov. Phys. Usp. 10, 509

[39] J. B. Pendry (2000), “Negative refraction makes a perfect lens”, Phys. Rev. Lett. 85, 3966

[40] A. Boltasseva, T. Nikolajsen, K. Leosson, K. Kjaer, M. S. Larsen and S. I. Bozhevolnyi (2005), “Integrated optical components utilizing long-range surface plasmon polaritons”, J. Lightwave Techno, vol. 23, no. 1

[41] R. Charbonneau, C. Scales, I. Breukelaar, S. Fafard, N. Lahoud, G. Mattiussi and P. Berini (2006), “Passive integrated optics elements based on long-range surface plasmon polaritons”, J. Lightwave. Techno, vol. 24, no. 1

[42] R. Charbonneau, P. Berini, E. Berolo, and E. Lisicka-Shrzek (2000), “Long-range plasmon-polariton wave propagation in thin metal films of finite width excited using an end-fire technique”, Proc. SPIE, Quebec City, Canada, vol. 4087, pp. 534-540

[43] R. Charbonneau (2001), “Demonstration of a passive integrated optics technology based on plasmons”, M. S. thesis, Faculty Eng., Univ. Ottawa, Ottawa, ON, Canada

[44] S. J. Al-Bader (2004), “Optical transmission on metallic wires: fundamental modes”, IEEE J. Quantum Electron., vol. 40, no. 3, pp. 325-329

[45] A. Boltasseva and S. I. Bozhevolnyi (2006), “Directional couplers using long-range surface plasmon polariton waveguides”, IEEE J. Quantum Electronics, vol. 12, no. 6

[46] J. A. Conway, S. Sahni, and T. Szkopek (2007), “Plasmonic interconnects versus conventional interconnects: a comparison of latency, crosstalk and energy costs”, Opt. Express, vol. 15, no. 7

[47] Drude, Paul (1900). "Zur Elektronentheorie der metalle" ,306 (3): 566.

[48] G. Veronis, S. E. Kocabas, D. A. B. Miller, and S. Fan (2009), “Modeling of plasmonic waveguide components and networks”, J. Comput. THeor. Nanosci, vol. 6, no. 6

[49] L. Martin-Moreno, F. J. Garcia-Vidal, H. J. Lezec, K. M. Pellerin, T. Thio, J. B. Pendry and T. W. Ebbesen (2001), “Theory of extraordinary optical transmission through sub-wavelength hole arrays”, Phys. Rev. Lett. 86, 1114

[50] Harrington, Roger F. (1961), Time-Harmonic Electromagnetic Fields, McGraw-Hill

[51] W. Steinhogl, G. Schindler, G. Steinlesberger, and M. Engelhardt (2000), “Size-dependent resistivity of metallic wires in the mesoscopic range”, Phys. Rev. b 66, 075414

[52] James Clerk Maxwell (1865), "A Dynamical Theory of the Electromagnetic Field", Philosophical Transactions of the Royal Society of London 155, 459–512

[53] M. Abramowitz and I. Stegun eds (1964), *Handbook of Mathematical functions with Formulas, Graphs and Mathematical Tables,* National Bureau of Standards. Washington, D. C

[54] Stefan A. Maier (2006), Plasmonics: Fundamentals and Applications, Springer, pp 25

[55] Ramo, Simon, John R. Whinnery, and Theodore van Duzer (1984), Fields and Waves in Communications Electronics, 2 ed., John Wiley and Sons, New York

[56] Pierre Berini (2000), “Plasmon-polariton Wave Guided by Thin Lossy Metal Films of Finite Width: Bound modes of Symmetric Structure”, Physical Review B, Vol. 61, No. 15

[57] Stefan A. Maier (2006), Plasmonics: Fundamentals and Applications, Springer, 25-29

[58] A. D. Polyanin and V. F. Zaitsev, Handbook of Exact Solutions for Ordinary Differential Equations (2nd edition), Chapman & Hall/CRC Press, Boca Raton, 2003

[59] Stefan A. Maier (2006), Plasmonics: Fundamentals and Applications, Springer, pp 23

[60] Ruiyuan Wan, Fang Liu, Xuan Tang, Yidong Huang, and Jiangde Peng (2009), "Vertical coupling between short range surface plasmon polariton mode and dielectric waveguide mode", Appl. Phys. Lett. 94, 141104

[61] Fang Liu, Yi Rao, Yidong Huang, Wei Zhang, and Jiangde Peng (2007), "Coupling between long range surface plasmon polariton mode and dielectric waveguide mode", Appl. Phys. Lett. **90**, 141101